Università degli Studi di Firenze

Dipartimento di Fisica

DOTTORATO DI RICERCA IN FISICA

Study of the deuterium spectrum in cosmic rays with the CAPRICE98 experiment

Tesi di Dottorato di Ricerca in Fisica di

Elena Vannuccini

Relatori	Dott.	Paolo Papini
	Dott.	Mirko Boezio
Relatore esterno	Prof.	Federico Palmonari

XIV Ciclo di Dottorato

Coordinatore	Prof.	Anna Maria Cartacci

Anno Accademico 2000/2001

Abstract

The initial chapters 1 and 2 introduce the physical background necessary to understand the scientific interest of this work. Chapter 1 discusses how the elemental and isotopic abundances of the stable cosmic-ray proton-nuclear component provides information on the mean amount of matter traversed by cosmic rays from their sources to the Earth. Chapter 2 will deal in detail with discussing the role of the light stable secondary isotopes deuterium and ^{3}He. The peculiar feature of these secondary components is that their interaction mean free path is considerably larger than the escape mean free path from the Galaxy, so that they are ideal probe to study the cosmic-ray propagation.

Most data concerning the composition and the energy spectra of cosmic rays are collected below few g/cm^2 of residual atmosphere, by means of balloon-borne experiments. As a consequence, the instruments detect also particles produced by the interactions of cosmic rays with the air nuclei, which include also deuterons. The deuterium atmospheric production is particularly significant below about 1 GeV/n, where the fragmentation of air nuclei dominates. Therefore, accurate corrections are essential in order to obtain reliable results from balloon-borne experiments measuring the low energy deuterium abundance. Chapter 3 presents a calculation carried out in order to evaluate the secondary deuterium energy and angular distributions, as a function of the atmospheric depth.

The remaining chapters 4-7 are dedicated to the central argument of this work, consisting in the measurement of the deuterium abundance in cosmic rays with the CAPRICE98 experiment. In chapter 4 the different parts of the CAPRICE98 apparatus are described: the time-of-flight system, the magnetic spectrometer, the Ring Imaging CHerenkov (RICH) detector and the electromagnetic calorimeter. Chapter 5 presents the applied basic selection criteria, as well as their efficiencies. The deuterium is identified among charge one particles by requiring no Cherenkov signal detected, for rigidity values above the proton threshold for Cherenkov light emission. The resulting sample of events contains a non-negligible component of protons. Since the deuterium identification is possible only using the RICH detector information, the proton background contamination and the deuterium selection efficiency have been evaluated by means of a simulation. In chapter 6 the analysis procedure developed to parameterize the instrument response is described and the simulation results are discussed. At the end of the chapter, the estimated number of protons and deuterons in the spectrometer is presented. In chapter 7 these numbers are corrected for the basic selection efficiency and for the attenuation and secondary particle production in the material above the tracking system, including the atmosphere. Finally, the deuterium flux and the deuterium-to-helium ratio in the kinetic energy range from 13 GeV/n to 22 GeV/n are presented. These results are compared with data from other experiments and theoretical predictions, with reference to the arguments discussed in chapter 2.

Contents

List of Figures

List of Tables

Chapter 1

Propagation of the proton-nuclear component of cosmic rays in the Galaxy

Cosmic rays are charged particles that hit the Earth's atmosphere at a rate of about 1000 $m^{-2}s^{-1}$. *About* 98% *of them are protons and nuclei and about* 2% *are electrons. The study of chemical abundances of the cosmic rays provides important clues to their origin and to the process of their propagation from the sources to Earth. The physical background necessary to understand the scientific interest of this work concerns the stable proton-nuclear component, within the kinetic energy range of some tens MeV/n to about some hundreds GeV/n. The elemental and isotopic abundances of stable nuclei give important information on the mean amount of matter traversed by the cosmic rays from their sources to Earth, where they are observed.*

In section 1.1 some basic observational data are reported. Section 1.2 introduces the theory of cosmic-ray propagation, and the last section, 1.3, shows how the observed secondary-to-primary ratios can be used to set constraints on propagation models.

1.1 The cosmic-ray proton-nuclear component as observed on Earth

The cosmic-ray spectra span a very wide range of energy. The units usually used to indicate the energy of cosmic rays refer to their kinetic energy per nucleon, which is essentially a measure of the Lorentz factor γ of the particles. Fig. 1.1 shows the differential fluxes of protons, helium, and carbon nuclei from some tens of MeV/n up to hundreds GeV/n. In this energy range the cosmic-ray flux is found to be isotropic.

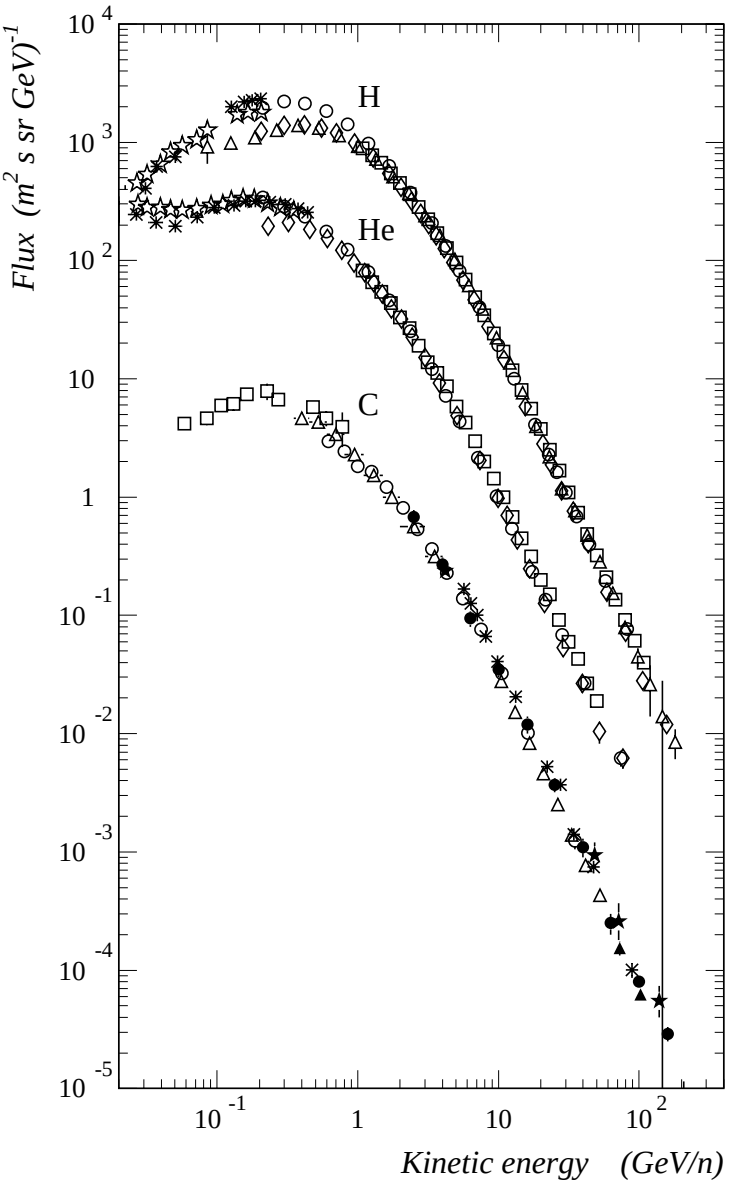

Figure 1.1: *The differential energy spectra of cosmic-ray proton, helium and carbon as measured on Earth at minimum solar modulation level.*

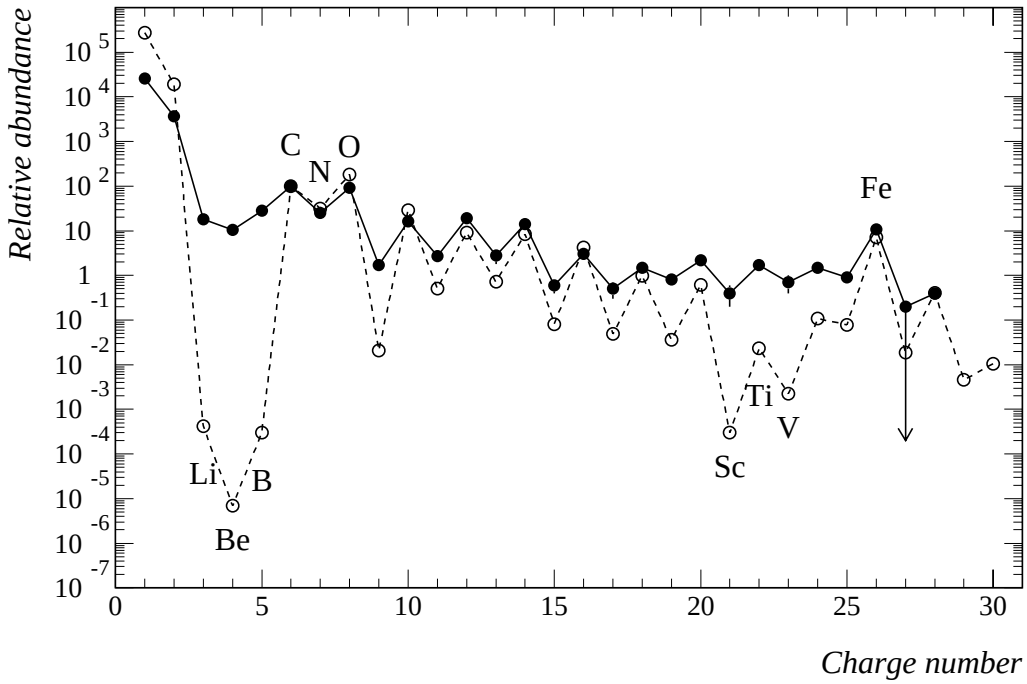

Figure 1.2: *Comparison between the cosmic rays and the Solar System element composition, both given relative to carbon. Filled circles: cosmic rays. Open circles: Solar System elements.*

Above ~ 1 GeV/n the differential energy spectra of the various cosmic-ray components is well represented by a power-law distribution whose spectral index lies in the range $2.5 - 2.7$. At energies less than ~ 1 GeV/n the energy spectra of all the cosmic-ray components show a pronounced attenuation, relative to the power-law observed at high energy. The position of the peak and the intensity at low energy are strongly correlated to the solar activity. In fact, the low energy flux attenuation is an effect of the diffusion of cosmic rays from the interstellar space towards the Earth, through the out-flowing Solar Wind [3]. This phenomenon is known as *solar modulation* of the flux of cosmic rays: the higher the solar activity, the lower the cosmic-ray flux at low energy. The data presented in fig. 1.1 refer to minimum solar modulation level. For a more complete collection of data including also maximum solar modulation periods, see section 3.4.

An interesting feature of the proton-nuclear component of cosmic rays emerges from the comparison of their composition with that of ordinary matter in the Galaxy. As an example, fig. 1.2 shows the comparison between the cosmic-ray elemental composition

(filled circles) with that of the Solar System [1] (open circles), up to $Z = 30$. It is evident that the overall distribution of elemental abundances in the cosmic rays is not so different from that in typical Solar System matter; in both cases the abundances show a peak at the elements C,N,O, and Fe, and the odd-even effect in the relative stabilities of the nuclei. The most evident difference between the two compositions is the overabundance in cosmic rays of Li,Be,B, and sub-Fe elements (Sc,Ti,V).

Such elements are usually thought to be formed by the nuclear interaction of cosmic rays and interstellar medium nuclei, during the propagation of cosmic rays from their sources to Earth. Within the energy range taken into consideration here, cosmic rays are essentially of a Galactic origin, and are produced and accelerated during supernovae explosions [3]. The spectroscopic data, the study of the composition of Solar System's and meteorites' matter, and the calculated nuclear reactions in stars suggest a Galaxy's homogeneous elemental composition which thus represents the average cosmic-ray composition at their sources. The resulting effect of the fragmentation processes is that the cosmic-ray abundances distribution as observed on Earth is smoother than at the sources. That is an overall feature that emerges from fig. 1.2. Therefore an important distinction is the one between the *primaries* cosmic-ray components which are accelerated in sources of high energy particles, and the *secondaries* cosmic-ray components which are produced by nuclear fragmentation. The relative abundances of secondary nuclei, with respect to their progenitors, give important information concerning the origin and the propagation of cosmic rays. In particular, as will be discussed in detail in section 1.3, the secondary-to-primary ratios suggest that, on average, cosmic rays in the GeV/n range traverse ~ 6 g/cm^2 [5] of equivalent hydrogen between injection and observation. When this value is compared with the amount of matter along a line of sight through the disk of the Galaxy, which is $\sim 10^{-3}$ g/cm^2 [5], it is easy to deduce that cosmic rays remain for a long time confined within a limited volume. The confinement volume include part or all of the Galactic disk and possibly the Galactic halo.

A second important experimental result, with implication for the cosmic-ray origin and propagation, is the energy dependence of the relative abundances of secondaries and primaries. Fig. 1.3 shows the ratio boron to carbon and the ratio sub-iron elements to iron as functions of the kinetic energy, measured by the HEAO-3 experiment [67]. In section 1.3 this feature will be related to the cosmic-ray propagation mechanism.

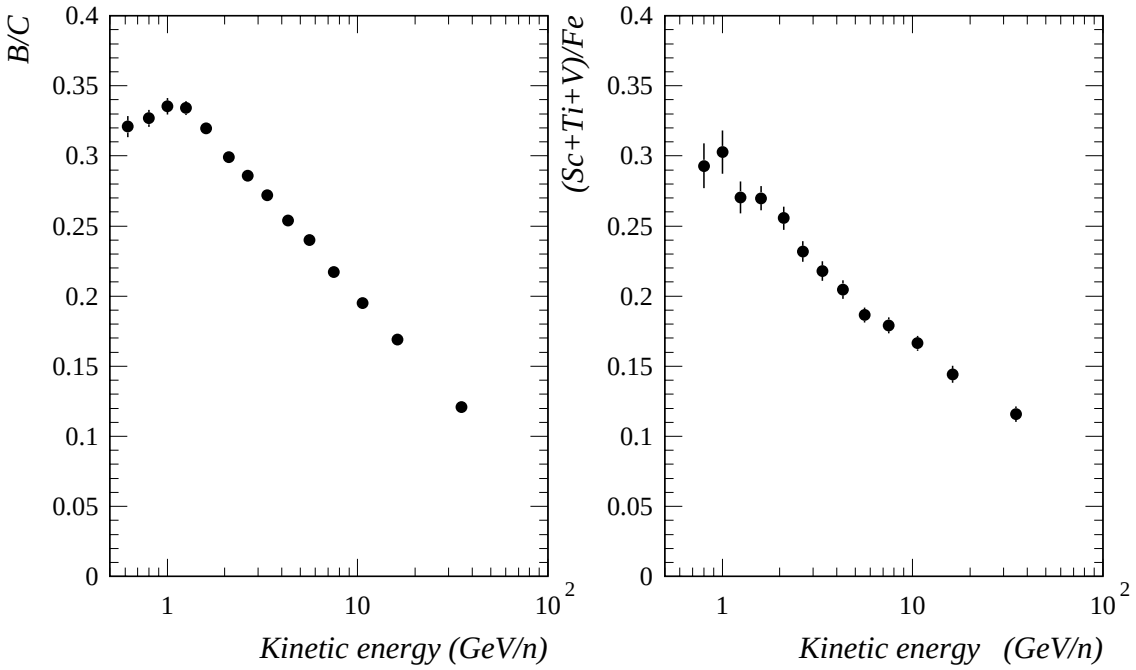

Figure 1.3: *Energy dependence of the secondary-to-primary ratio. Left plot: B/C ratio. Right plot: sub-Fe/Fe ratio.*

In addition to the overall chemical abundances, of particular interest is the isotopic composition of cosmic rays. The light stable elements, ^{1}H, ^{2}H, ^{3}He, and ^{4}He form a special group of isotopes. The discussion on this subject is deferred to chapter 2, since it is directly involved in the interpretation of the deuterium measurement performed by the CAPRICE98 experiment, which is the central part of this work. A further important aspect of the isotopic composition of cosmic rays is that some of the secondaries produced during the fragmentation processes are radioactive, so that they give information about the time that cosmic rays spent to reach the Earth from their source regions.

In the following will be discussed how the observational evidences concerning the stable proton-nuclear component of cosmic rays can be accounted for by the propagation mechanism.

1.2 General transport equations

A theory that explains the nature of the propagation of cosmic rays should take into account the interaction mechanism of the charged particle with the interstellar medium, where a decisive role is played by the galactic magnetic field. The details of the specific physical mechanism that regulates the motion of cosmic rays is however still unclear, mainly because of the lack of detailed information concerning the interstellar medium and the magnetic field structures. To interpret the observations one generally uses approximate semi empirical models, which anyway make it possible to correlate the basic features of experimental data.

A sufficiently general set of transport equations to describe the proton-nuclei cosmic-ray propagation through the Galaxy is the one presented by Ginzburg and Syrovatskii [2]:

$$\frac{\partial N_i}{\partial t} = \nabla \cdot (\hat{\mathcal{D}} \nabla N_i) - \nabla \cdot \mathbf{u}\, N_i - \frac{\partial}{\partial E}\left[b_i N_i\right] + \mathcal{Q}_i - p_i N_i + \sum_{k \geq i} N_k p_{k \to i} \qquad (1.1)$$

Eq. 1.1 describes the variation with time of the density $N_i = N_i(E, \mathbf{r}, t)$ of cosmic rays nuclei of type i at position $\mathbf{r}$ and with kinetic energy per nucleon between E and $E + dE$.

The first and second terms on the right hand side represent the diffusion, where $\hat{\mathcal{D}}$ is the diffusion tensor assumed to be independent on the kind of particle, and convection with velocity $\mathbf{u}$. The third term takes into account the continuous energy variations, and can represent either energy loss by ionization or acceleration, depending on the application. The function $b_i = dE/dt$ expresses the change in energy per unit of time of a single nucleus of type i. For the following discussion it will be assumed that the particles are not accelerated in the interstellar medium, but that they originate in point-like sources whose intensity, spectrum, and space time distribution are described by the functions $\mathcal{Q}_i = \mathcal{Q}_i(E, \mathbf{r}, t)$, where i denotes the nucleus type. The quantity $\mathcal{Q}_i$ expresses the number of particles injected in the interstellar medium, per time unit and volume, in the energy range between E and $E + dE$.

The fifth term represents the loss of nuclei of type i by collision and decay, whose probability per time unit is:

$$p_i = n\beta c\sigma_i + \frac{1}{\gamma \tau_i}\,, \qquad (1.2)$$

where $n = n(\mathbf{r})$ is the density of the interstellar gas, σ_i is the inelastic cross-section, and τ_i is the nucleus lifetime with respect to the radioactive decay. The following discussion

will take into consideration an interstellar medium composed of hydrogen only, since this simplifying assumption does not affect the conclusions. The last term describes the production of nuclei of type i from the interactions of nuclei of different type and the summation is carried out over heavier nuclei. For the production probability $p_{k\to i}$ holds the same notation of eq. 1.2; in this case $\sigma_{k\to i}$ is the inclusive cross-section for the production of the nucleus i from the breakup of a nucleus of type k, and $\tau_{k\to i}$ is the lifetime of the nucleus k with respect to the nuclear decay channel that leads to the production of the nucleus of type i. The production term can be written in the simple form used in eq. 1.1 because in fragmentation reactions of relativistic nuclei the kinetic energy per nucleon is nearly conserved. This process is known as *spallation*.

A complete solution of the problem requires the knowledge of shape and size of the propagation regions of cosmic rays in the Galaxy, and the distribution of interstellar gas and sources. Besides that, it will be assumed that all the fragmentation cross-sections and the lifetimes for nuclear decay are known.

Once all this quantities are specified, the general approach is to get the parameters of the theory from the observed secondary abundances. In fact, in this case the source term is $\mathcal{Q}_i = 0$, so that the secondary cosmic-ray density is only related to the propagation parameters. Once the parameters are known, one can infer the composition at the sources from the observed primary abundances.

1.2.1 Solution of the equations for stable nuclei

The aim of this chapter is to discuss the role of the stable secondary cosmic rays as tools to study the propagation mechanism within the Galaxy, in order to understand, in particular, the scientific interest of the measurements of light isotopes abundances. The discussion is therefore limited to stable nuclei, setting the decay term in eq. 1.2 to zero.

A stationary picture of the cosmic-ray propagation will be taken into consideration, since several experimental data [3] suggest that cosmic-ray intensity did not change significantly over the past hundred million years. As a consequence, the dependence on time t in eq. 1.1 can be ignored, and the left hand side of the equation can be set equal to zero.

At a kinetic energy below ~ 1 GeV/n the cosmic-ray flux is affected by solar activity, so that the interpretation of data at such energy values must take into account the solar

modulation effect. Since this is beyond the subject of this chapter, the discussion will be restricted to an energy above several GeV/n. This simplifies the transport equations, since ionization losses can be neglected.

With the above mentioned conditions eq. 1.1 simplifies as follows:

$$-\nabla \cdot (\hat{\mathcal{D}} \nabla N_i) + n\beta c \sigma_i N_i = \mathcal{Q}_i + \sum_{k \geq i} n\beta c \sigma_{k \to i} N_k \tag{1.3}$$

Let the spatial distribution of sources be independent of the kind of nuclei, that is $\mathcal{Q}_i(\mathbf{r}) = q_i \chi(\mathbf{r})$ where q_i are constants that determine the abundances of the various nuclei at the sources. It can be demonstrated [4] that eq. 1.3 has a solution of the form:

$$N_i(\mathbf{r}) = \int_0^\infty N_i^{(\sigma)}(x)\, \mathcal{G}(\mathbf{r}, x)\, dx\,, \tag{1.4}$$

where $N_i^{(\sigma)}$ and $\mathcal{G}$, which are both function of the parameter x (expressed in g/cm^2), satisfy the following equations:

$$mn\beta c \frac{\partial \mathcal{G}}{\partial x} - \nabla \cdot (\hat{\mathcal{D}} \nabla \mathcal{G}) = 0 \quad \text{with} \quad mn\beta c\, \mathcal{G}(\mathbf{r}, 0) = \chi(\mathbf{r})\,, \tag{1.5}$$

$$\frac{dN_i^{(\sigma)}}{dx} + \frac{\sigma_i}{m} N_i^{(\sigma)} - \sum_{k \geq i} \frac{\sigma_{k \to i}}{m} N_k^{(\sigma)} = 0 \quad \text{with} \quad N_i^{(\sigma)}(0) = q_i\,, \tag{1.6}$$

where m is the hydrogen mass. The function $\mathcal{G}$ should also satisfy the boundary conditions for $N_i(\mathbf{r})$ related to the geometry of the containment volume.

By expressing the transport equation in this form, it is possible to separate the strictly astrophysical aspects of the cosmic-ray propagation, related to the function $\mathcal{G}$, from the aspects concerning the fragmentation by nuclear interactions with the interstellar medium, related to the function $N_i^{(\sigma)}$. In fact, given a specific composition q_i at the sources, the quantities $N_i^{(\sigma)}(x)$ represent the variation of the cosmic-ray composition due only to fragmentation processes after traversing an amount x of matter, and they are related only to the nuclear cross-sections (σ_i, $\sigma_{k \to i}$). The quantity $\mathcal{G}(\mathbf{r}, x)$ is instead related only to the parameters of the considered propagation model: the diffusion tensor ($\hat{\mathcal{D}}$), the geometry of the containment volume, the source and interstellar medium distributions ($n(\mathbf{r})$, $\chi(\mathbf{r})$).

The function $\mathcal{G}$ is usually called *path-length distribution*. The interpretation of $\mathcal{G}(\mathbf{r}, x)$ as path-length distribution is clear from eq. 1.4, which states that the cosmic-ray density at the position $\mathbf{r}$ is obtained by averaging the composition expressed by

$N_i^{(\sigma)}(x)$ over the distribution of path lengths $\mathcal{G}(\mathbf{r}, x)$ traveled by cosmic rays, from their sources to the point $\mathbf{r}$.

For any propagation model that satisfies the requirement $\mathcal{Q}_i(\mathbf{r}) = q_i\chi(\mathbf{r})$ and can be expressed by a set of transport equations of the kind 1.3, all the information concerning the propagation processes is included in the function $\mathcal{G}(\mathbf{r}, x)$. The following chapter will show that the cosmic-ray secondary-to-primary ratio provides in principle direct information on the path-length distribution and, as a consequence, on the cosmic-ray propagation mechanism.

1.3 The secondary-to-primary ratio

In order to discuss the physical interest in the study of stable secondary cosmic rays it is useful to introduce first the *Leaky-Box Model (LBM)*. This is a very simple and widely used model, which in spite of its simplicity gives a satisfactory interpretation of observational data and includes the basic features of the cosmic-ray propagation in the Galaxy. A specific description of some models, formulated within the framework of the LBM, may be found in the next chapter, that deals with the discussion on the light isotope cosmic-ray component.

1.3.1 The Leaky Box Model (LBM)

Within the framework of the LBM it is assumed that the density of the cosmic rays, and the distribution of the interstellar medium and of the sources in the whole system (the Galaxy), are constant and uniform. The diffusion term in eq. 1.3 is thus replaced by assuming a finite escape probability τ_{esc} from the confinement volume:

$$\nabla \cdot (\hat{\mathcal{D}} \nabla N_i) \longrightarrow -\frac{N_i}{\tau_{esc}} \,. \tag{1.7}$$

In the picture generally associated to the LBM the Galaxy is described as a box with a small leakage of particles; cosmic rays propagate freely inside the containment volume undergoing many reflections at the boundaries before escaping. The LBM set of transport equations which describes the propagation of stable nuclei is obtained substituting the escape term in eq. 1.3 and dividing for $mn\beta c$:

$$\frac{\mathcal{Q}_i}{mn\beta c} - \frac{N_i}{\lambda_i} - \frac{N_i}{\lambda_{esc}} + \sum_{k>i} \frac{N_k}{\lambda_{k\to i}} = 0 \,. \tag{1.8}$$

In eq. 1.8 we have introduced the interaction lengths $\lambda = m/\sigma$, where σ is the cross-section for the considered process. With these approximations the cosmic-ray propagation is described, for the various kinds of nuclei i, by a set of algebric equations which can be solved analytically. In eq. 1.8 the only parameter of the model is expressed as

$$\lambda_{esc} = mn\beta c\,\tau_{esc}\ , \tag{1.9}$$

which represents the mean amount of matter, in g/cm^2, traversed by cosmic rays before their escape from the confinement volume. This interpretation of λ_{esc} is evident from the LBM path-length distribution function. The solution of eq. 1.5, after replacement of the diffusion term with the escape term, gives as a result:

$$\mathcal{G}_{LBM}(x) \propto e^{-x/\lambda_{esc}}\ . \tag{1.10}$$

One of the main constraints on the LBM parameter λ_{esc} comes from the ratio of stable secondary to primary abundances. For simplicity's sake, let be taken into consideration a secondary nucleus of type S whose only parent nucleus is of type P. In this case the set of transport equations is reduced to a system of two equations:

$$\frac{\mathcal{Q}_P}{mn\beta c} - \frac{N_P}{\lambda_P} - \frac{N_P}{\lambda_{esc}} = 0 \tag{1.11}$$

$$-\frac{N_S}{\lambda_S} - \frac{N_S}{\lambda_{esc}} + \frac{N_P}{\lambda_{P\to S}} = 0 \tag{1.12}$$

The solution of the above system gives the following expression for the secondary-to-primary ratio:

$$S/P = \frac{N_S}{N_P} = \frac{\lambda_{esc}/\lambda_{P\to S}}{(1+\lambda_{esc}/\lambda_S)} \xrightarrow[\lambda_S \gg \lambda_{esc}]{} \frac{\lambda_{esc}}{\lambda_{P\to S}}\ . \tag{1.13}$$

In eq. 1.13 it is clear that, in the extreme case of a secondary nucleus with a long interaction mean free path, the secondary to primary ratio S/P is directly proportional to the escape mean free path of cosmic rays from the Galaxy.

The main results concerning the stable nuclear component of cosmic rays within the framework of the LBM are summarized in the following.

- The observed abundances at a few GeV/n of the stable secondary nuclei Li,Be,B and Sc,Ti,V,Cr, produced respectively by the spallation of the nuclei C,N,O and Fe, are both well described by assuming an escape mean free path from the confinement volume of:

$$\lambda_{esc} = 5 - 8\ \mathrm{g/cm^2} \tag{1.14}$$

of equivalent hydrogen (see reference [4] for references concerning this result). Besides Li,Be,B and sub-Fe nuclei, there are other secondary isotopes, among which are included deuterium and ^{3}He. Chapter 2 will show that the interpretation of the D and ^{3}He abundances with the same escape mean free path obtained from heavier secondary nuclei is still unclear.

- From the observed dependence of the secondary-to-primary ratio on energy, it is inferable that the mean amount of matter traversed by cosmic rays before their escape from the Galaxy is energy dependent, and in particular it decreases for increasing energy (see B/C and (Sr+Ti+V)/Fe in fig. 1.3). According to several authors the composition of $Z > 2$ cosmic-ray nuclei can be interpreted by assuming a rigidity[1] dependent escape mean free path which, at energy values above some GV, is of the type $\lambda_{esc} \propto R^{-\delta}$. Several parameterizations have been proposed for the function $\lambda_{esc} = \lambda_{esc}(R)$ obtained by fitting the observed secondary-to-primary ratio, generally B/C ratio. The results of the fit depend on the model adopted, in particular on the cross-section values used, and on the composition of the interstellar medium, so that the resulting parameterizations of λ_{esc} can differ by large amounts (see reference [11] for a collection of results). Notice that if the energy dependence of the cross-sections is neglected, being λ_{esc} the only parameter of the theory, the energy dependence of the secondary-to-primary ratio can be ascribed only to it. The rigidity dependence of λ_{esc} can be accounted for within the framework of more complex models [4].

1.3.2 Probing the path-length distribution function with different secondary nuclei

A conclusion reached in section 1.2 is that in a sufficiently general scenario of the propagation of cosmic rays in the Galaxy all information concerning the propagation mechanism, the geometry of the confinement volume, and the distribution of the sources and of the interstellar medium are contained in the path-length distribution function $\mathcal{G}(\mathbf{r}, x)$. The LBM is a very simplified version of the general model expressed by the set of transport equations 1.3. In this model the path-length distribution function is described by one parameter only, the escape mean free path from the Galaxy λ_{esc}.

[1] See section 4.1.2 for the definition of rigidity.

Within the framework of this model it is therefore sufficient to know the abundances of just one secondary nuclear component and its progenitors, in order to determine the parameter of the model. It has also been asserted that the observed abundances of heavy secondary Li,Be,B and sub-Fe nuclei are consistent with a value of escape mean free path of about 6 g/cm^2, at energies in the GeV/n range.

This section shows, in an intuitive way, that the secondary-to-primary ratios not only provide information on the mean amount of matter traversed by cosmic rays before their escape from the Galaxy, but may in principle be used to reconstruct the whole shape of the path-length distribution function, which could differ from the exponential shape assumed within the framework of the LBM (see reference [4] for a rigorous treatment of this argument).

Let be assumed that the true path-length distribution function is an unknown function $\mathcal{G}(\mathbf{r}, x)$. Let be taken into consideration a simple system of one secondary nucleus of type S and one primary nucleus of type P. By solving the equations 1.6 for this system and using the eq. 1.4, for the secondary-to-primary ratio the following general expression is obtained:

$$S/P = \frac{1}{\lambda_{P\to S}} \frac{1}{\left(\frac{1}{\lambda_S} - \frac{1}{\lambda_P}\right)} \left[1 - \frac{\int_0^\infty \mathcal{G}(\mathbf{r}, x) e^{-x/\lambda_S} dx}{\int_0^\infty \mathcal{G}(\mathbf{r}, x) e^{-x/\lambda_P} dx}\right] . \tag{1.15}$$

The important feature of the above expression is that the path-length distribution $\mathcal{G}(x)$ appears in the equation weighted by a factor $e^{-x/\lambda_{S,P}}$. This means that the abundances of secondary and primary nuclei of different kinds are sensitive to different regions of the path-length distribution. In particular heavy nuclei, which have short interaction mean free paths if compared with the escape mean free path, are sensitive to short path lengths. In the extreme case of $\lambda_{S,P} \ll \langle x \rangle$, where $\langle x \rangle$ is the mean value of the path-length distribution function $\mathcal{G}(\mathbf{r}, x)$, eq. 1.15 gives the following:

$$S/P \sim \frac{\lambda_S}{\lambda_{P\to S}} , \tag{1.16}$$

so that the observed secondary-to-primary ratio is entirely determined by the fragmentation cross-section, and any information on the propagation through the Galaxy is lost. Light nuclei have instead a long interaction mean free path, so that they are sensitive also to the remote tail of the path-length distribution function. In the extreme

case of $\lambda_{S,P} \gg \langle x \rangle$:

$$S/P \sim \frac{\langle x \rangle}{\lambda_{P \to S}} \,, \tag{1.17}$$

that is, the observed secondary-to-primary ratio depends only on the mean amount of traversed matter and is not sensitive to the specific shape of $\mathcal{G}(\mathbf{r}, x)$.

By combining the observational data of different secondary nucleus abundances it is possible, in principle, to reconstruct the whole shape of the path-length distribution function. To this purpose, it is advisable to study cosmic-ray nuclei with a wide range of cross-sections.

Actually the present experimental knowledge does not allow to determine much more than the average thickness of matter traversed by cosmic rays in the Galaxy. From the above discussion it follows that among all the secondary cosmic-ray nuclear components, of particular interest are the light ones. In fact, having an interaction mean free path considerably longer than the average thickness of matter traversed by cosmic rays before their escape from the Galaxy, such light components give a complete information on the propagation process, which is not the case for heavier nuclei.

Besides that, it is important to study different secondaries because their progenitors could have a different propagation history, so that, for example, the conclusion drawn by the study of the secondary nuclei Li,Be,B could hold for carbon, but not for helium or hydrogen.

Chapter 2

Deuterium in Cosmic Rays

Deuterium and ^{3}He isotopes are present in cosmic rays as a result of nuclear interactions mainly of primary ^{4}He with the interstellar medium. As a consequence, they are part of a class of secondary stable nuclei that, as discussed in section 1.3, provide information on the mean amount of matter traversed by cosmic rays before escaping from the Galaxy. The peculiar feature of light secondary isotopes is that their interaction mean free path is considerably larger than the escape mean free path from the Galaxy, so that they are ideal probes to study the cosmic rays propagation. In spite of their scientific relevance, few experimental data exist, due to the difficulties of such measurements.

In section 2.1 a collection of deuterium and ^{3}He data is presented and the main features discussed. In the next section 2.2 the experimental data are compared with the results of some calculations. The cosmic rays deuterium and ^{3}He physics is similar, therefore the discussion involves both. However, since the central part of this work is the measurement of the deuterium abundances, the presented collection of data and theoretical calculations is exhaustive only for the deuterium, and not for ^{3}He.

2.1 Deuterium as observed on Earth

Deuterium and ^{3}He are very fragile isotopes, and they are destroyed, rather than formed, in the stars. Their presence in cosmic rays is due to nuclear interactions with the interstellar medium. The main production channel of both deuterium and ^{3}He is from the spallation of cosmic rays ^{4}He nuclei. For the deuterium there is also a significant contribution from the resonant reaction p+p $\rightarrow$ D+π. The cross-section for this process is well measured [35] and shows a pronounced peak at an incident

Table 2.1: *List of the available deuterium and ^{3}He measurements above 100 MeV/n. Column 2 indicates the year when each experiment was carried out. The symbol * indicates the measurements performed during maximum solar modulation level (see fig. 3.4). The last column indicates the identification technique; η is the magnetic deflection and R is the magnetic rigidity (see section 4.1.2).*

Reference	Year	Isotope	Symbol	Identification technique
Apparao [6]	1973	D	❋	Cherenkov threshold counter
Webber & Yushak [101]	1977	^{3}He	□	$dE/dX \times E$
Bogomolov *et al.* [7]	1979	D	☆	Cherenkov threshold counter
Webber *et al.* [10]	1989*	D,^{3}He	▲	$dE/dX \times \eta^2$
Papini [11]	1989*	D	▼	$dE/dX \times \eta^2$
Beatty *et al.* [15]	1989*	^{3}He	●	$\beta \times R$
Hatano *et al.* [17]	1989*	^{3}He	■	Cherenkov threshold counter
Bogomolov *et al.* [8]	1990*	D	★	Cherenkov threshold counter
Reimer *et al.* [16]	1992	^{3}He	☆	$\beta \times R$
Finetti [12]	1994	D	△	$\beta \times R$
Lamanna [13]	1998	D	○	$\beta \times R$

proton kinetic energy of ~ 0.6 GeV; since this is a two-body reaction, the energy of the final state particles is fixed, so that the deuterium is produced mainly within a limited energy range, $\sim$ 80 to 250 MeV/n. This is an interesting feature of the cosmic rays deuterium, since it is the only secondary particle, besides antiprotons positrons and electrons, that is a product of the cosmic rays proton propagation in the interstellar medium.

The most recent measurements of deuterium and ^{3}He abundances at a kinetic energy above 100 MeV/n are summarized in tab. 2.1, together with the year when each experiment was carried out and the isotope identification technique employed. Fig. 2.1 shows the D/(^{3}He+^{4}He)[1] kinetic energy. If we exclude the result of Apparao [6], then all the available measurements are below 2 GeV/n.

It is important to notice that all the deuterium measurements but [13] were performed by means of balloon-borne instruments. These experiments fly under a few g/cm^2 of residual atmosphere, so that the instruments detect also particles produced by the interactions of cosmic rays with air nuclei, whose contribution must be sub-

[1] In references [7, 8, 10] data on D/^{4}He ratio are presented, we thus have scaled them in order to take into account the ^{3}He component. In reference [10] results on the ^{3}He/^{4}He ratio are also reported, from which a mean value of 0.11 has been estimated. In order to scale the results of references [7, 8], a mean value of ^{3}He/^{4}He$\sim$ 0.17 has been instead assumed, obtained by averaging the ^{3}He/^{4}He data at about 1 GeV/n.

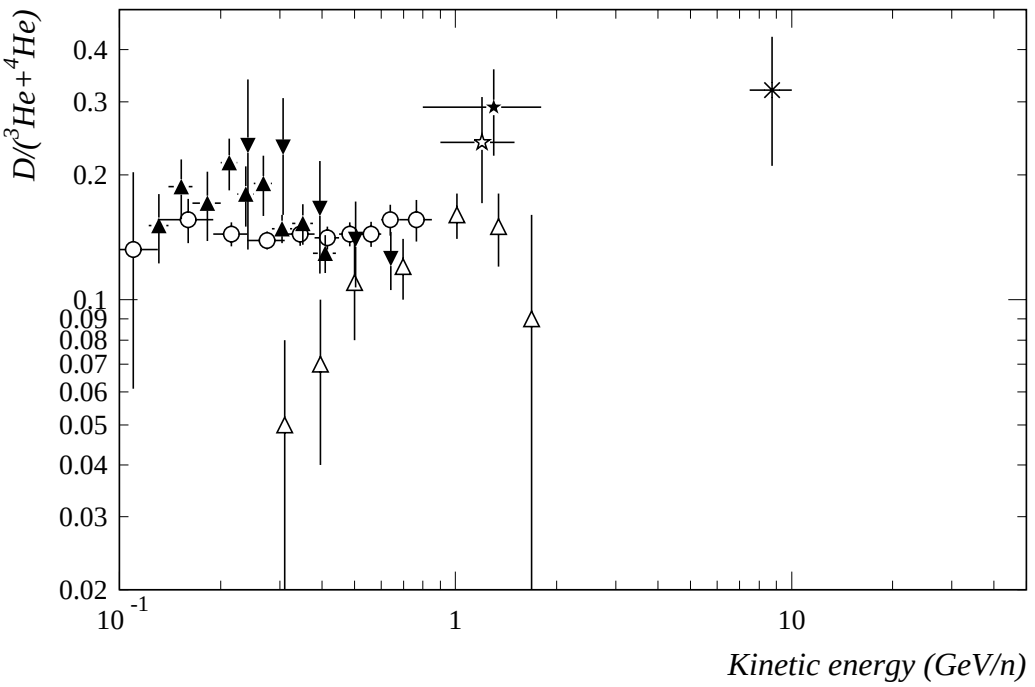

Figure 2.1: *Measured D/(^{3}He+^{4}He) ratio. (see tab. 2.1 for references and footnote[1]).*

tracted in order to estimate the galactic component. As will be discussed in chapter 3, the atmospheric production is particularly significant, below 1 GeV/n, in the case of deuterium measurements, due to the large amount of deuterons produced during the fragmentation of air target nuclei. This contribution, which increases at decreasing energy, is difficult to estimate, so that the low energy balloon data are affected by large uncertainties. This could partly explain the observed disagreement among data in fig. 2.1.

As pointed out in section 1.1, at an energy below $\sim$ 1 GeV/n the cosmic rays propagation through the Solar System is affected by the solar activity, which results in strong time variations on the cosmic rays flux observed on Earth. Even if the ratio D/(^{3}He+^{4}He) is less affected by the solar modulation than the single fluxes, a non negligible effect still exists. The general trend is that to an higher solar modulation level corresponds an higher value of the ratio D/He (compare the measurement year in tab. 2.1 to the Climax neutron monitor flux shown in fig. 3.4). This is in agreement with the predictions of Webber *et al.* [101], who calculated the low energy helium and

hydrogen isotopes abundances for different levels of solar activity.

In general, there is a lack of experimental results above 2 GeV/n, where the information concerning the cosmic rays propagation through the Galaxy is more significant. In fact at high energy the solar modulation effect becomes negligible, so that the galactic propagation models can be checked without assumptions on the modulation effect. Besides this, it is above several GeV/n that deviations may be found from the standard cosmic rays propagation scenario, which predicts a decrease at the energy of the escape mean free path from the Galaxy (see section 1.3.1).

2.2 Theoretical predictions

Due to the large uncertainties on the measured deuterium and ^{3}He abundances, it is generally not possible to determine the appropriate interstellar path length of their progenitors at the same level of accuracy as for heavier nuclei. The general approach is thus to extend to cosmic rays helium the same energy dependent escape mean free path inferred from B/C ratio, which is measured with good accuracy over a wide energy range (see fig. 1.3).

The assumption for helium to have the same propagation history of heavier nuclei is however not so straightforward. Some alternative propagation models have been proposed in the past, motivated by the observed large abundance of cosmic rays antiprotons [7, 9]. These models require a large amount of matter to be traversed by cosmic rays, so that most of the heavy nuclei are destroyed while the production of light secondary nuclei is enhanced. As a consequence, deuterium and ^{3}He abundances are ideal tools to test the reliability of these models [18, 19].

In this section the available deuterium and ^{3}He data are compared to some theoretical predictions, both within the framework of *standard* models (LBM) [19, 20, 21] and of some non-standard models [19]. The collection of theoretical calculations here includes all the results concerning the deuterium abundance up to at least 10 GeV/n. For comparison also the predictions for the ^{3}He abundance, presented by the same authors, are shown.

Table 2.2: *Parameterizations used for LBM calculations whose results are shown in fig. 2.2.*

LBM calculations			
Reference $\longrightarrow$	Stephens [19]	Mewaldt [20]	Webber [21]
Cosmic rays sources			
Spectrum $\longrightarrow$	$\propto R^{-2.75}$	$\propto (E(GeV)+0.5)^{-2.6}$	$\propto R^{-2.6}$
Composition $\longrightarrow$	p:α=100:5	p:α:($Z>6$)=100:6:1	p:α:C:O =100:6.3:0.3:0.4 (other elements with Solar System abundances)
Cross-sections	[35]	[35]	[52, 22]
Interstellar medium			
Composition $\longrightarrow$	H 100%	H 90% He 10%	H 90% He 10% ionized fraction 30%
Escape mean free path			
$\lambda_{esc}(R)$ (g/cm^2) $\longrightarrow$	if $R<5.5$ GV then $8.$ else $8[R/5.5]^{-0.6}$	if $R<5.5$ GV then $28.5\beta 5.5^{-0.65}$ else $28.5\beta R^{-0.65}$	if $R<4.7$ GV then 12.5β else $31.6\beta R^{-0.6}$

2.2.1 Standard models

Fig. 2.2 shows the predicted D/(^{3}He+^{4}He) and ^{3}He/^{4}He ratios from three different calculations carried out within the framework of the *LBM*. It is evident that the results, even if performed within the same propagation model, differ by large amounts. This is due to different assumptions concerning the source spectrum and composition, the fragmentation cross-sections, the interstellar medium and the energy dependence for the escape mean free path. The parameterizations of these quantities used by the three authors are shown for comparison in tab. 2.2. In fig. 2.3 we compare the parameterizations of the escape mean free path as a function of the rigidity R, used by the three authors.

The different shape of the secondary-to-primary ratio resulting from each calculation reflects essentially the parameterization of λ_{esc}. The normalization of λ_{esc} includes the interstellar medium composition.

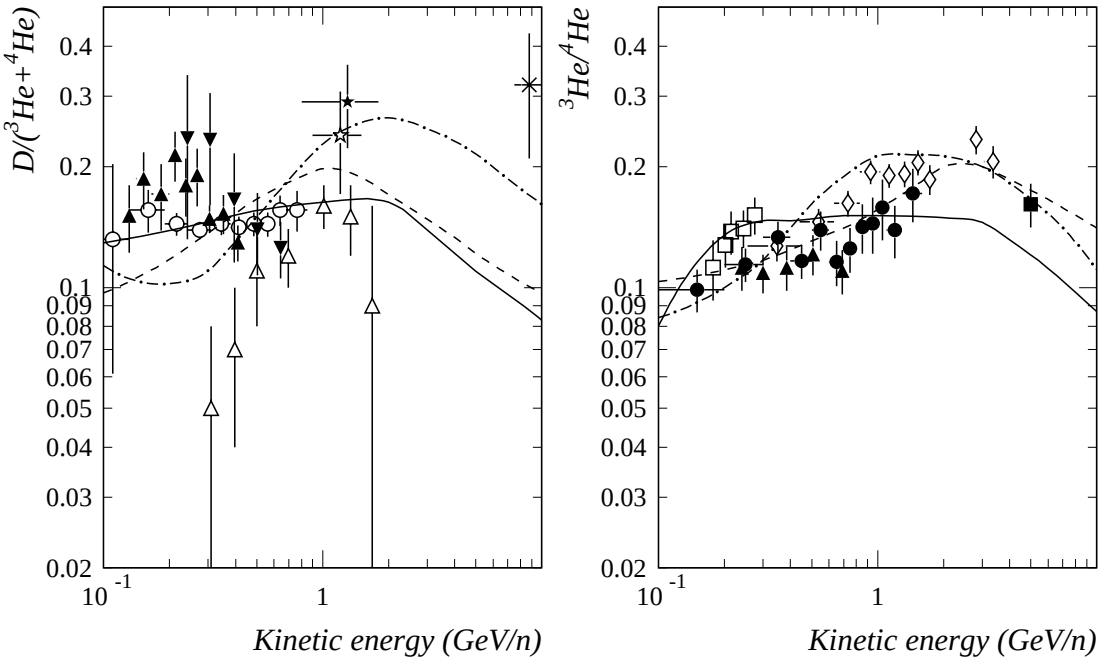

Figure 2.2: *Theoretical predictions for $D/(^3He+^4He)$ and $^3He/^4He$ ratios, resulting from three different calculations in the framework of the LBM. Symbols: experimental data (see tab. 2.1 for references). Solid curves: Stephens [19]. Dashed curves: Webber [21]. Dotted-dashed curve: Mewaldt [20]. The Webber calculation assumes a solar modulation proper for the IMAX data (◊)[16]. The other calculations assume minimum solar modulation level.*

At low energy the differences between the calculation results are also related to the solar modulation model adopted and to the solar activity level assumed . Both results from references [19, 20] refer to minimum solar activity, whereas the calculation from reference [21] has been carried out to interpret the IMAX ^{3}He data [16], so that the proper solar modulation level has been taken into account (see reference [21] for more details). Above some GeV/n the solar modulation does not affect significantly the secondary-to-primary ratio [101], so that the results of the calculation directly reflect the galactic propagation model adopted.

The common feature of the three calculations is a broad peak in the secondary-to-primary ratio around a kinetic energy value of a few GeV/n, above which the ratio decreases. This is a direct consequence of the assumed energy dependence of the escape mean free path λ_{esc}, which decreases following a power law for increasing rigidity

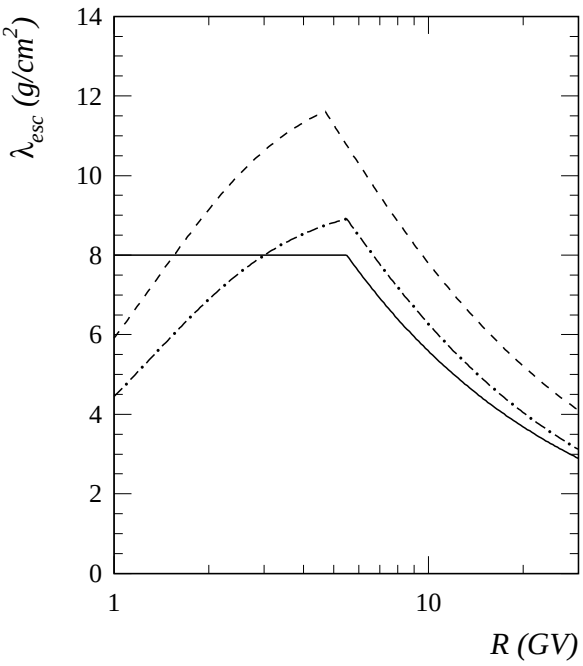

Figure 2.3: *Comparison of the parameterizations of the escape mean free path used in the LBM calculations whose results are shown in fig. 2.2. Solid curves: Stephens [19]. Dashed curves: Webber [21]. Dotted-dashed curve: Mewaldt [20].*

values above ~ 5 GV (see fig. 2.3), as resulting from the fit of B/C data. It is therefore inferable that a more significant comparison of experimental data and theoretical predictions is above ~ 1 GeV/n.

Comparison with experimental data

The few available high energy measurements (Bogomolov [7, 8] and Apparao [6]) of the D/(^{3}He+^{4}He) ratio suggest an overabundance of deuterium with respect to the standard model predictions. At a low energy, the solar minimum experimental data (Lamanna [13] and Finetti [12]) are better reproduced by the Stephens calculation [19] than the other two. Notice that the Finetti results are affected by large uncertainties due to atmospheric corrections. However no definitive conclusions can be drawn, due to the paucity of experimental results and an only partial agreement among the available ones. Besides that, as previously described, the standard scenario is not definite, since the presented calculations give different predictions.

The experimental scenario is more clear for ^{3}He data, which instead show a general agreement with standard predictions. According to reference [101], the effect of the solar modulation is lower for the ^{3}He/^{4}He ratio than for D/(^{3}He+^{4}He). If we exclud the Webber [101] results, data are in better agreement with the Mewaldt [20] and

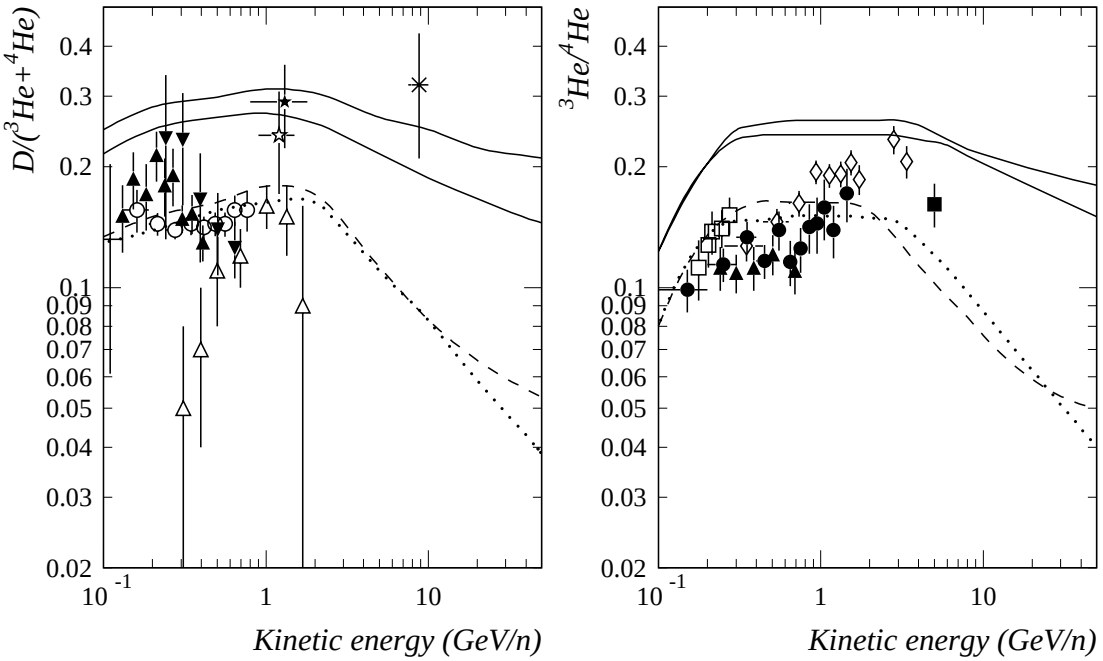

Figure 2.4: *Theoretical predictions for D/(^{3}He+^{4}He) and ^{3}He/^{4}He ratios from the calculation of Stephens [19], on the basis of some non-standard models. Symbols: experimental data (see tab. 2.1 for references). Upper solid curve: CGM calculation. Lower solid curve: TSM calculation. Dashed curve: NLBM calculation. Dotted curve: LBM calculation.*

Webber [21] calculations, which assume a similar shape for λ_{esc}. Even in this case, however, only a few data [16, 17] extend above 2 GeV/n.

In general, for a clearer understanding of the light cosmic rays nuclei propagation it is desirable to have experimental results at higher energy.

2.2.2 Non-standard models

Stephens [19] calculates the D/(^{3}He+^{4}He) and ^{3}He/^{4}He ratios also using some non-standard models. The models are described in the following and the predicted secondary-to-primary ratios are compared with experimental data in fig. 2.4.

Nested Leaky-Box Model

The *Nested Leaky-Box Model* ($NLBM$) is similar to the LBM. According to this model [23, 24] there are two confinement regions for cosmic rays. The inner confinement region surrounds the cosmic rays sources. Particles are confined inside the sources with an energy dependent escape probability. A physical realization might be a supernova inside a dense cloud. The Galaxy is treated as an outer volume inside which cosmic rays are confined, after escaping from their sources, in an energy independent manner. The energy dependence of the secondary-to-primary ratio is thus attributed to the energy dependent leakage from the source regions.

The calculation of Stephens [19] assumes an escape mean free path from the sources of $\lambda_1 = 6.4(R/5.5)^{-0.6}$ g/cm^2, for $R > 5.5$ GV, the remaining $\lambda_2 = 6.4$ g/cm^2 being traversed in the Galaxy in an energy independent manner. The predicted D/(^{3}He+^{4}He) and ^{3}He/^{4}He ratios, shown in fig. 2.4 by dashed curves, are similar to those resulting from the LBM (dotted curves). The main difference is at high energy, where the secondary-to-primary ratio expected from $NLBM$ is higher than that predicted by LBM. This happens at kinetic energy values for which the LBM escape mean free path is lower than the fixed value $\lambda_2 = 6.4$ g/cm^2 assumed in the $NLBM$.

Thick Source Model

The *Thick Source Model* (TSM) [25] hypothesizes the existence of sources shrouded by dense gas inside the Galaxy. Cosmic rays generated by these sources have to traverse a fixed amount of matter ($30 - 50$ g/cm^2) before being injected into the interstellar medium. This model was formulated to explain the observed excess of antiprotons and positrons. While the heavy nuclei are absorbed in the gas surrounding these sources, the production of light secondary is enhanced, so that also an excess of deuterium and ^{3}He is produced.

In the calculation of Stephens [19] 30% of cosmic-ray sources are assumed to be thick. Cosmic rays originating from these sources are supposed to traverse 30 g/cm^2 of pure hydrogen, and then they are propagated through the Galaxy according to the LBM. The result is shown by lower solid curves in fig. 2.4. As expected, this model gives a secondary-to-primary ratio considerably higher than the simple LBM.

Closed Galaxy Model

The *Closed Galaxy Model* (CGM) [26] can be considered a variation of the $NLBM$ in which the inner volume is the local spiral arm of the Galaxy, inside which cosmic rays are confined in an energy dependent manner. After escaping from the inner containment volume, they remain confined in an outer volume, assimilable to the galactic halo, until they are destroyed by interaction or energy loss processes. As a result, the cosmic rays observed on Earth are composed by a *young* component, just injected from the sources into the interstellar medium and still confined in the inner volume, and an *old* or *degraded* component, consisting essentially of stable particles with a large amount of secondary nuclei. This model, as the TSM, has been proposed to explain the observed overabundances of antiprotons and positrons.

In the Stephens calculation [19] the *young* component is described by using the $NLBM$. The two components are then added in the proportion of 50% and 50%. The source composition is modified in order to reproduce the observed composition on Earth. The result is shown by the upper solid curve in fig. 2.4.

Comparison with experimental data

If we exclude the measurements of Bogomolov [7, 8] and Apparao [6], that suggest an overabundance of deuterium and are consistent with the CGM and TSM predictions, all the other D/(^{3}He+^{4}He) results are in better agreement with the LBM and the $NLBM$. The ^{3}He data instead do not give any evidence supporting the CGM and TSM.

Chapter 3

Atmospheric deuterium production

Most experiments measuring the composition and the energy spectra of cosmic rays are carried out with balloon-borne instruments. Data are collected below few g/cm^2 of residual atmosphere, therefore, to determine the flux at the top of atmosphere, primary flux attenuation and secondary particle production have to be taken into account. These corrections introduce systematic uncertainties in the final results, which play an important role in the measurements of rare cosmic-ray components, such as deuterium. Therefore, accurate atmospheric corrections are essential in order to obtain reliable results and to take advantage of the improvements of the experimental techniques.

The atmospheric secondaries are produced by both the spallation of heavy cosmic-ray nuclei and as final products of air nucleus fragmentation due to nuclear interactions with the incident cosmic radiation. Protons and neutrons are the major component of the atmospheric secondary particles. Therefore, a correct estimate of the nucleon fluxes is of primary importance to evaluate the energy spectra of the other secondary particles. A detailed study of the atmospheric nucleon energy spectra was carried out by Papini et al. [29, 11]. This work has been used as a starting point to evaluate the atmospheric deuterium spectrum. Preliminary results were presented in reference [28]. In the present calculation [30] the secondary particle production by nuclei heavier than helium has been included and new fragmentation cross-sections have been used. Moreover, this calculation provides the angular distribution of the secondary deuterium.

The deuterium production processes and the transport equations are described in sections 3.1 and 3.2, respectively. The parameters defined in these sections are evaluated in section 3.3, where a compilation of nuclear cross-sections is presented. The primary cosmic-ray fluxes at the top of atmosphere used as input for this calculation

are described in section 3.4. In section 3.5 the final results are discussed.

3.1 Deuterium production in the atmosphere

By definition, the flux J is the number of particles per units of solid angle $d\Omega$ and energy dE[1] that pass per unit of time dt through a unit of surface dS perpendicular to the direction of observation. Deuterium is produced in the atmosphere from the interaction of cosmic rays with the air nuclei. Therefore, to evaluate the deuterium flux J_D in the atmosphere several production processes have to be taken into account. Each process is described by means of a production term defined as

$$P(E,l) = \frac{dN_D}{d\Omega dE dt dS dl} = \frac{dJ_D}{dl}\,, \tag{3.1}$$

which represents the increase of the deuterium flux per unit path length dl. The quantity l is the amount of atmosphere in the direction of observation and it is expressed in g/cm^2. In a polar reference system with the axis in the zenith direction, assuming a flat atmosphere, l can be expressed as $x/\cos\theta$, where x is the atmospheric depth in the vertical direction and θ is the zenith angle.

The production term defined in eq. 3.1 has the following general expression:

$$P(E,\theta,x) = \int dE' \int d\Omega^* \Phi(E';E,\theta^*) \frac{J(E',\theta'(\theta^*,\phi^*),x)}{\lambda(E')}\,, \tag{3.2}$$

where E and θ are the energy and the direction of the outgoing deuterium, E' and θ' are those of the projectile and θ^* is the emission angle of the deuterium referred to the incidence direction of the incoming particle. In eq. 3.2 the last factor indicates the number of interactions, per units of energy and time and per gram of atmosphere, for the incident particle flux $J(E',\theta',x)$ at a depth x; $\lambda(E')$ is the interaction length for each process leading to deuteron production and it is expressed in g/cm^2 ($\lambda(E') = A_{air}/N_\circ\sigma(E')$ where $\sigma(E')$ is the cross-section[2]). The quantity $\Phi(E';E,\theta^*)$, where the function Φ is defined by the relation

$$\left(\frac{d\sigma^3}{dE d\Omega^*}\right) = \sigma(E')\Phi(E';E,\theta^*)\,, \tag{3.3}$$

[1] Here and in the following E denotes the kinetic energy per nucleon.

[2] The air has been described as composed of a single nuclear component with mass number $A_{air} = 14.4$

is the distribution of deuterons, as a function of the energy E and solid angle Ω, produced per single interaction by an incident particle of energy E' with a scattering angle θ^*. The production term (eq. 3.2) is integrated over all energies E' and over the emission angles θ^*,ϕ^*.

The production processes that we have considered can be grouped in three categories:

1. fragmentation of air target nuclei;
2. nuclear interaction of incident nucleons through the reactions p(n)+p(n)$\rightarrow$ D+π;
3. spallation of incident nuclei.

In this section each production process listed above is discussed and the corresponding production term is described (eq. 3.2).

3.1.1 Deuterium production from air nuclei

During a nucleus-nucleus inelastic interaction both projectile and target might undergo fragmentation, resulting in the production of nucleons and lighter nuclei. The energy distribution of the emitted fragments, in the rest system of the fragmenting nucleus, ranges up to few hundred MeV.

A detailed discussion of nucleon production from air target nuclei is reported in Papini *et al.* [29] and the results are applied by the authors to a calculation of the secondary proton spectrum in the atmosphere. In this work the same approach for the deuterium production has been used. The deuterium energy and angular distributions have been obtained from data compiled by Powell *et al.* [27] on cosmic-ray proton interaction in nuclear emulsions.

The angular and energy distribution of the emitted deuterons have been parameterized as it follows:

$$\Phi(E';E,\theta^*) = 0.85 T(E) F(\theta^*) \omega(E')\,, \tag{3.4}$$

The function $T(E)$ represents the number of deuterons emitted per interaction and unit energy; the scale factor 0.85 makes this function proper for air targets. By fitting the experimental data [27] the following expression for $T(E)$ has been obtained:

$$T(E) = \begin{cases} 0.14\, E(GeV/n)^{-1.6} & \text{if } E < 0.5 \text{ GeV/n} \\ 2.07 \exp[-3.2\, E(GeV/n)] & \text{otherwise.} \end{cases} \tag{3.5}$$

The function $F(\theta^*)$ represents the normalized angular distribution of the emitted deuterons. The weighting function $\omega(E')$ has been introduced to reproduce the observed [27] increase of the number of emitted fragments for increasing projectile energy up to ~ 1 GeV/n. Above this value the fragment distribution is approximately energy independent. Because of the lack of data available in literature, both $F(\theta^*)$ and $\omega(E')$ have been assumed to be the same used for the recoil nucleons by Papini *et al.* [29].

Both incoming nucleons and nuclei contribute to the production of deuterium from the fragmentation of air target nuclei. As a consequence the last factor in eq. 3.2 can be expressed as it follows:

$$\frac{J(E',\theta',x)}{\lambda(E')} \equiv \frac{J_p(E',\theta',x) + J_n(E',\theta',x)}{\lambda'_p(E')} + \sum_i \langle N\rangle_i \frac{J_i(E',\theta',x)}{\lambda'_i(E')}\,, \tag{3.6}$$

where the summation is extended to all the considered nuclear components, as will be discussed afterwards in section 3.2. The factors $\langle N\rangle_i$ have been introduced when projectiles are nuclei and represent the mean number of participating nucleons during an interaction of a nucleus of type i with an air nucleus. In eq. 3.6 $\lambda'_{p(i)}(E')$ denotes the total interaction length of nucleons (nuclei) in air.

3.1.2 Deuterium production from nucleons

Nucleons contribute to the deuterium production through the reaction p(n)+p(n)$\rightarrow$ D+π, occurring between incident nucleons and nucleons inside air nuclei. The cross-section for this process is well measured and shows a pronounced peak at 0.6 GeV [35, 32]. This process should be included in the deuterium production from target fragmentation. However, the parameterization described in section 3.1.1 has been obtained from data on nuclear emulsions averaged over the projectile energy. As a consequence any structure in the deuterium spectrum due to the resonant reaction p(n)+p(n)$\rightarrow$ D+π is lost. We thus included this reaction as a separate production process.

The considered reaction has two particles in the final state, therefore, if the energy of the projectile is known, the energy of the emitted deuterium in the center-of-mass reference system (CMS) is univocally determined. The angular distribution of the emitted deuterons is approximately given by [35]:

$$F(\theta^*_{cm}) = \frac{0.22 + \cos^2\theta^*_{cm}}{6.95}\,. \tag{3.7}$$

To obtain the angular and energy distribution in the laboratory system (LS) the properties of the invariant cross-section can be used:

$$\left(\epsilon\frac{d\sigma^3}{d^3p}\right)_{LS} = \left(\epsilon\frac{d\sigma^3}{d^3p}\right)_{CMS}, \tag{3.8}$$

where ϵ is the total energy of the emitted deuterium in the corresponding system. From the above equation and eq. 3.3 we obtain:

$$\Phi(E';E,\theta^*) = \frac{2\,F(\theta^*_{cm})}{M\beta\gamma\beta_\circ\gamma_\circ}\,\delta(cos\theta^* - cos\theta^*_\circ)\,, \tag{3.9}$$

where $\beta_\circ$ and $\gamma_\circ$ are the velocity and the Lorentz factor of the deuterium in the center-of-mass reference system, β and γ are those of the center-of-mass in the laboratory system and M is the deuterium mass. The delta function takes into account that, when E', E and θ^* are given, the scattering angle in the laboratory reference system is fixed.

Both protons and neutrons contribute to the deuterium production through this reaction, therefore, the last factor on right hand side of eq. 3.2 is given by:

$$\frac{J(E',\theta',x)}{\lambda(E')} \equiv \frac{J_p(E',\theta',x) + J_n(E',\theta',x)}{\lambda_{pp\to D\pi}(E')}\,, \tag{3.10}$$

where $\lambda_{pp\to D\pi}(E')$ is the interaction length for the process p+p→D+π in air.

3.1.3 Deuterium production from incident nuclei

Incident nuclei undergo fragmentation in the atmosphere, resulting in the production of lighter particles. It will be shown afterwards that the deuterium production is dominated by these processes at energies larger than $\sim$ 1 GeV/n. Therefore, fragments are assumed to be produced with the same kinetic energy and in the same direction of the parent nucleus. As a consequence eq. 3.2 reduces to:

$$P_{i\to j} = \frac{J_i(E,\theta,x)}{\lambda_{i\to j}(E)}\,, \tag{3.11}$$

where i denotes the incident nucleus and j the produced fragment.

3.2 Transport equations

The deuterium production processes discussed in the previous section involve both nucleons and nuclei. The knowledge of their fluxes at any atmospheric depth and in any direction is thus required to determine the deuterium flux.

In this calculation distinct equations have been introduced for deuterium, protons, neutrons, ^{4}He, ^{3}He, ^{3}H and HN (heavy nuclei). The fluxes of ^{3}He and ^{3}H have been also evaluated because these isotopes are a product of ^{4}He spallation that can lead to further deuteron production. Nuclei heavier than ^{4}He have been included in the calculation in terms of an equivalent number of ^{12}C. A nucleus of atomic weight A has been considered equivalent to $n_{^{12}C}(A) = (A/12)^{2/3}$ of ^{12}C nuclei. This scaling factor expresses the ration between the geometrical cross-sections.

The deuterium transport equation and the set of equations for nucleons and nuclei have been decoupled by including the deuterium in the nucleon equations as one free proton and a neutron.

In the following the set of coupled equations for nucleons and nuclei as well as for deuterium are described. The notation for the interaction lengths is the following: λ' denotes the total interaction length; λ denotes the length for interactions with large momentum transfer only; $\lambda_{i\to j}$ denotes the interaction length for the inclusive production of particle i from particle j.

3.2.1 Nucleons and nuclei

The transport equations for nucleons are those reported by Papini *et al.* [29] modified here to include the considered nuclear components.

$$\begin{aligned}\frac{\partial J_p(E,\theta,x)}{\partial l} &= \frac{\partial}{\partial E}\left[J_p(E,\theta,x)\left(\frac{dE}{dl}\right)_p\right] - \frac{J_p(E,\theta,x)}{\lambda'_p(E)} + \\ &+ \sum_i \langle p\rangle_i \, J_i(E,\theta,x)\left(\frac{1}{\lambda'_i(E)} - \frac{1}{\lambda_i(E)}\right) + \\ &+ \int_E^\infty dE'\Phi(E')\left[\frac{J_p(E',\theta',x)}{\lambda_p(E')}\,(1-\alpha) + \frac{J_n(E',\theta',x)}{\lambda_p(E')}\,\alpha + \right. \\ &\left. + \sum_i \langle p\rangle_i \, \frac{J_i(E',\theta',x)}{\lambda_i(E')}\right] + P_{rec}(E,\theta,x) + P_{ev}(E,\theta,x)\end{aligned} \tag{3.12}$$

$$\begin{aligned}\frac{\partial J_n(E,\theta,x)}{\partial l} &= -\frac{J_n(E,\theta,x)}{\lambda'_p(E)} + \\ &+ \sum_i \langle n\rangle_i \, J_i(E,\theta,x)\left(\frac{1}{\lambda'_i(E)} - \frac{1}{\lambda_i(E)}\right) +\end{aligned} \tag{3.13}$$

$$+\int_E^\infty dE'\Phi(E')\left[\frac{J_p(E',\theta',x)}{\lambda_p(E')}\,\alpha+\frac{J_n(E',\theta',x)}{\lambda_p(E')}\,(1-\alpha)+\right.$$
$$\left.+\sum_i\langle n\rangle_i\,\frac{J_i(E',\theta',x)}{\lambda_i(E')}\right]+P_{rec}(E,\theta,x)+P_{ev}(E,\theta,x)$$

The first two terms in eq. 3.12 take into account the continuous energy losses due to ionization and loss of particles through interactions respectively. The third term describes the production of protons from the spallation of nuclei: in this process the stripped protons have the same kinetic energy per nucleon of the parent nucleus. The fourth term takes care of inelastic interactions involving large momentum transfer. These interactions lead to: discrete energy losses, loss and gain of particles due to charge exchange (with probability α) and nucleon production from incident nuclei. The integration has been carried out from the threshold energy for pion production. The last two terms represent the proton component produced through evaporation and recoil from air nuclei. The transport equation for neutrons (eq. 3.13) is analogous to that of protons with the exception of the ionization term, absent in the case of neutrons. In the equations 3.12 and 3.13, the summations have been carried out over the considered nuclear components (i=^{4}He,^{3}He,^{3}H,HN). The factors $\langle p(n)\rangle_i$ represent the mean number of free protons (neutrons) produced per interaction of a nucleus of type i. It has to be noticed that these factors also take into account the production of deuterium, which has been included in the calculation as two free nucleons. For more details on the nucleon propagation through the atmosphere see reference [29].

The transport equations for nuclei are the following:

$$\frac{\partial J_{^3H,^3He}(E,\theta,x)}{\partial l} = \frac{\partial}{\partial E}\left[J_{^3H,^3He}(E,\theta,x)\left(\frac{dE}{dl}\right)_{^3H,^3He}\right]+ \tag{3.14}$$
$$-\frac{J_{^3H,^3He}(E,\theta,x)}{\lambda'_{^3H,^3He}(E)}+\sum_{i=^4He,HN}\frac{J_i(E,\theta,x)}{\lambda_{i\to^3H,^3He}(E)}$$

$$\frac{\partial J_{^4He}(E,\theta,x)}{\partial l} = \frac{\partial}{\partial E}\left[J_{^4He}(E,\theta,x)\left(\frac{dE}{dl}\right)_{^4He}\right]+ \tag{3.15}$$
$$-f_{^4He}\,\frac{J_{^4He}(E,\theta,x)}{\lambda'_{^4He}(E)}+\frac{J_{HN}(E,\theta,x)}{\lambda_{^{12}C\to^4He}(E)}$$

$$\frac{\partial J_{HN}(E,\theta,x)}{\partial l} = \frac{1}{3}\langle\frac{Z^2}{A}\rangle\,\frac{\partial}{\partial E}\left[J_{HN}(E,\theta,x)\left(\frac{dE}{dl}\right)_{^{12}C}\right]+ \tag{3.16}$$
$$-f_{^{12}C}\,\frac{J_{HN}(E,\theta,x)}{\lambda'_{^{12}C}(E)}$$

The above set of equations takes into account energy losses due to ionization, loss of nuclei due to interactions and light nucleus production from the fragmentation of heavier nuclei. Only the spallation of heavier nuclei has been included since the production of particles from the air nucleus fragmentation decreases significantly as fragment mass increases. As a consequence, for the calculation of the atmospheric deuterium flux, the nucleon production from air nucleus fragmentation (P_{rec} and P_{ev} in equations 3.12 and 3.13) has been taken into account, while the production of nuclei heavier than deuterium has been neglected.

In equations 3.16 and 3.15 the interaction loss terms have been multiplied by the factors $f_{^4He}$ and $f_{^{12}C}$, representing the actual fragmentation probability during an inelastic collision of ^4He and ^{12}C with an air nucleus. These parameters are evaluated in section 3.3.1.

The ionization energy loss terms in equations 3.14-3.16 have been calculated on the basis of the range ($\mathcal{R}$) versus momentum (p) relation given by [31]:

$$\mathcal{R}(p) = \frac{M}{Z^2\ m}\ \mathcal{R}_p(p \cdot m/M)\ , \tag{3.17}$$

where Z and M represent the charge and mass of the nucleus (^{3}H, ^{3}He, ^{4}He or ^{12}C), m is the proton mass and $\mathcal{R}_p$ is the proton range in air. The ionization term in eq. 3.16 has been multiplied by a factor that allows to take properly into account the effective charge composition of HN. The quantity $\langle Z^2/A \rangle$ denotes the average value calculated on the basis of the composition at the top of the atmosphere and weighting each species with the factor $n_{^{12}C}$. From the measured abundances [76] a value of $\langle Z^2/A \rangle \sim 4.58$ has been estimated.

3.2.2 Deuterium

The transport equation for the deuterium has the following expression:

$$\begin{aligned} \frac{\partial J_D(E,\theta,x)}{\partial l} \;=\; & \frac{\partial}{\partial E}\left[J_D(E,\theta,x)\left(\frac{dE}{dl}\right)_D\right] - \frac{J_D(E,\theta,x)}{\lambda'_D(E)} + \\ & + \sum_i \frac{J_i(E,\theta,x)}{\lambda_{i\to D}(E)} + \\ & + P_{air}(E,\theta,x) + P_{pp\to D\pi}(E,\theta,x) \end{aligned} \tag{3.18}$$

The first two terms on the right hand side of eq. 3.19 describe the deuterium energy losses by ionization and the attenuation due to interaction with air nuclei. The third

term represents the deuterium production from the spallation of heavier nuclei and the summation is carried out over i =^{3}H,^{3}He,^{4}He,NH. The fourth term describes the production from air nuclei. The deuterium production through the resonant reaction p(n)+p(n)$\rightarrow$ D+π is described by the last term.

3.2.3 The calculation

The transport equations have been solved using a 1th-order Runge-Kutta technique with step size $\Delta x = 0.003$ g/cm^2. The calculation has been carried out, starting from the top of the atmosphere, to an atmospheric depth of 80 g/cm^2 and up to $\theta = 85°$. The deuterium flux has been evaluated in the energy range from 100 MeV/n to 100 GeV/n. The step size has been properly chosen, in order to make the energy losses for low energy carbon nuclei at large zenith angles negligible compared to their energy. The parameters of the calculation are described in the following section.

3.3 Cross-sections

In this section details are given concerning the cross-section values for the processes involving deuterium, ^{3}H, ^{3}He, ^{4}He and ^{12}C as projectile. The nucleon cross-sections are the same used by Papini *et al.* [29]. All the parameters related to the cross-sections have been obtained from a compilation of data regarding particle interactions with carbon as target. As a general rule, the cross-sections have been scaled to air target by assuming a simple relation of the form

$$\sigma \propto \left(A_P^{1/3} + A_T^{1/3}\right)^y \ , \tag{3.19}$$

where A_P and A_T are the projectile and target mass numbers, while y is a parameter that depends on the considered process. For mole details concerning the cross-section compilation see appendix A.

3.3.1 Total interaction cross-sections

The total interaction cross-section, which is related to the total interaction length λ', has been introduced to describe both the processes of fragmentation of the air target nuclei (eq. 3.6) as well as the flux attenuation in the atmosphere (equations 3.14-3.16 and 3.19). Fig. 3.1 shows all available data on total interaction cross-sections, above

100 MeV/n of projectile kinetic energy, for deuterium, ^{4}He and ^{12}C. It can be noticed that measurements from different experiments show some disagreements. This can be attributed to systematic errors and to some inconsistencies in the definition of the total interaction cross-section. The general trend [37] is that the cross-sections obtained in counter experiments (filled symbols) are greater than those obtained in track-chamber experiments (open symbols). In the first case the total interaction cross-section is obtained indirectly as the difference between the total and the elastic cross-sections; in the second case only those inelastic processes leading to projectile fragmentation are included.

The difference is not relevant for deuterium and ^{12}C projectiles. Therefore, we have assumed for the total interaction cross-sections a mean value above 1 GeV/n of 413 mb and 823 mb, respectively. To scale the deuterium total interaction cross-section from carbon to air target D+Be and D+C data [44] have been used, obtaining 481 mb. For ^{12}C projectiles data are available in literature only on carbon as target; to estimate the scaling factor from carbon to air target ^{12}C+C and ^{16}O+C data on total charge changing cross section at 1.5 GeV/n [48] have been used. The obtained value is 909 mb.

The difference between the results from counter and track-chamber experiments is significant for ^{4}He cross-section. As a consequence, the ^{4}He total interaction cross-section has been estimated from counter experiments only, obtaining a mean value above 1 GeV/n of 532 mb. To scale the cross-section to air target available data on ^{12}C+He and ^{16}O+He [48] have been used, obtaining a value of 593 mb. To describe the ^{4}He flux attenuation in the atmosphere we are however interested only in that processes leading to projectile fragmentation. Therefore, the fragmentation probability $f_{^4He}$ has been introduced in eq. 3.15 and its value has been estimated from the the comparison between counter and track-chamber measurements, obtaining $f_{^4He} \sim 0.82$.

There is only one available measurement of the ^{3}He total interaction cross-section with carbon target, at 790 MeV/n [46]. ^{3}He and ^{4}He projectiles were used in this experiment and the quoted total inelastic cross-sections are 550 ± 5 mb and 503 ± 5 mb respectively. It has to be noticed that the cross-section of ^{3}He is greater than that of ^{4}He; this is reasonable since ^{3}He is less bounded than ^{4}He and, as a consequence, it is more easily destroyed. No data are available for ^{3}H projectile. The cross-section has been assumed to be the same for ^{3}H and ^{3}He projectiles, using a high energy value of 563 mb. This value has been obtained from the measurement on carbon target

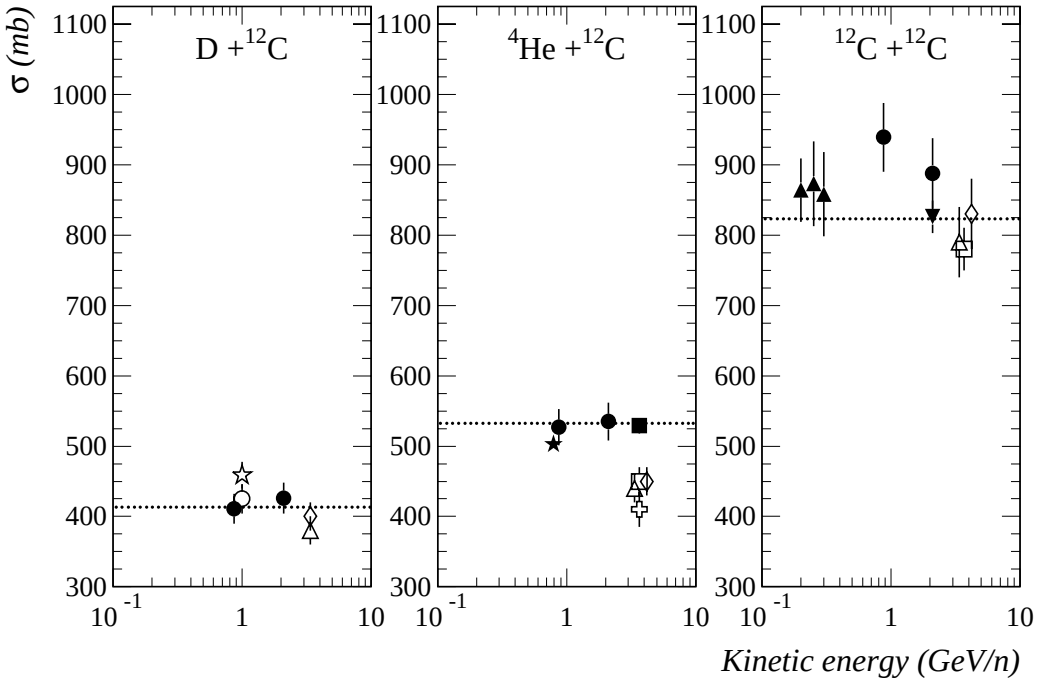

Figure 3.1: *Total interaction cross-sections for D,*^{4}*He and* ^{12}*C projectiles on carbon target (see tab. A.1 for references). Symbols: experimental data. Dotted lines: high-energy mean value.*

assuming the same scaling factor found for ^{4}He.

No evidence of a significant energy dependence is shown by available data on total interaction cross-section, therefore the average high energy value of the total interaction cross-section has been used.

From the above estimated values of the total interaction cross-sections, the mean number of nucleons $\langle N \rangle_i$ participating in the interaction (introduced in eq. 3.6) has been evaluated using the relation [36]:

$$\langle N_i \rangle = A_i \, \frac{\sigma'_{p+Air}}{\sigma'_{P_i+Air}} \, , \tag{3.20}$$

where σ'_{p+Air} and σ'_{P_i+Air} are the total interaction cross-sections for protons and for the nuclear component i, respectively. The value obtained are $\langle N \rangle_{^3H,^3He} \sim 1.5$, $\langle N \rangle_{^4He} \sim 1.9$ and $\langle N \rangle_{^{12}C} \sim 3.8$.

In eq. 3.16 the fragmentation probability $f_{^{12}C}$ for heavy nuclei has been introduced.

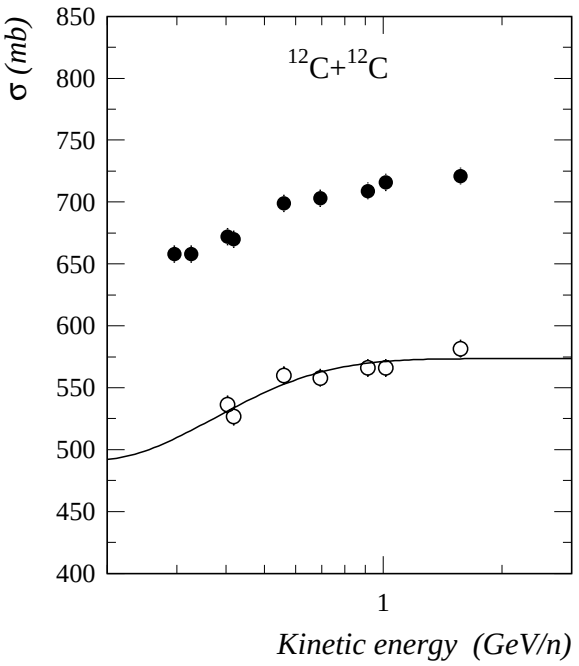

Figure 3.2: *Total charge changing cross-section (filled circles) for ^{12}C projectile on carbon target [48] and effective fragmentation cross-section of ^{12}C (open circles), defined as the difference between the total charge changing cross-section and the cross-section for the production of B and Be fragments [49].*

The reason is that the collision of a heavy nucleus with an air nucleus may result in the production of fragments heavier than helium, which are included in this calculation in the flux of heavy nuclei. As a consequence, only those processes leading to the spallation of the projectile nucleus with helium and/or lighter fragment production have been considered. Fig. 3.2 shows (filled circles) the total charge changing cross-section as a function of energy measured by Webber *et al.* [48] for ^{12}C projectile colliding with carbon target. Fig. 3.2 also shows (open circles) the fragmentation cross-section values obtained from the total charge changing cross-section after subtracting the cross-section for the production of the heavy Be and B fragments [49]. This quantity has been assumed as the effective fragmentation cross-section for ^{12}C nuclei. The scaling factor from carbon to air target has been estimated separately for the total charge changing cross-section and the cross-section for the production of B and Be at high energy. For the total charge changing cross-section, the same scaling factor for the total inelastic cross-section has been used. For the production of heavy fragments B and Be, ^{12}C+C and ^{12}C+Al partial cross-sections [51] have been considered. The obtained values are 799 mb and 155 mb, respectively, resulting in an "effective" fragmentation cross-section in air of 644 mb. By comparing this value with the total interaction cross-section, we

obtain a fragmentation probability at high energy of $f_{^{12}C} \sim 0.71$.

The solid line in fig. 3.2 represents the parameterization [50] used to reproduce the observed energy dependence of the effective fragmentation cross-section.

For the cross-sections related to collisions with large momentum transfer, introduced in eq. 3.12, the same parameterization of Papini *et al.* [29] has been used, normalized to the high energy value given by the relation:

$$\sigma(mb) = 56.7\ (A_P^{1/3} + A_T^{1/3} - 1.25)^2\ , \tag{3.21}$$

where A_P and A_T are the projectile and target mass numbers. The calculated cross-sections using eq. 3.21 are 435 mb for ^4He and 684 mb for ^{12}C. To calculate the cross-section of ^{3}He and ^{3}H eq. 3.21 has been modified to take into account that the nuclear radius of ^{3}He (and ^{3}H) is [46] $R_{^3He} \sim 1.1\ R_{^4He}$. A final value of 486 mb has been obtained.

3.3.2 Partial fragmentation cross-sections

Few data are available in literature on the partial fragmentation cross-sections with nuclear targets. Therefore, some assumptions have been made in order to determine the partial fragmentation cross-sections needed for this calculation. In the following some experimental data are presented, from which the inclusive cross-sections for the light nucleus production and the mean number of free nucleons produced in the fragmentation of the projectiles have been evaluated.

Fig. 3.3 shows the measured partial fragmentation cross-sections as a function of energy for the of ^{4}He projectiles, producing deuterium, ^{3}H and ^{3}He, on hydrogen target. It can be noticed that, in case of the production of ^{3}H and ^{3}He, there is a general agreement among different measurements and no evident energy dependence of the cross-sections is shown. In case of deuterium production, the results presented by Webber [52] appear to be not in agreement with other recent measurements [53, 54, 55, 56]. If we neglect the cross-sections measured by Webber, the deuterium data also suggest an energy independent trend, as it is observed for ^{3}H and ^{3}He data. Therefore, it has been assumed that the partial fragmentation cross-section is independent on projectile energy above 100 MeV. The shaded bands in fig. 3.3 show the range where the partial fragmentation cross-section measurement lie, over the energy range where measurements are available. It can also be seen from fig. 3.3 that the average partial

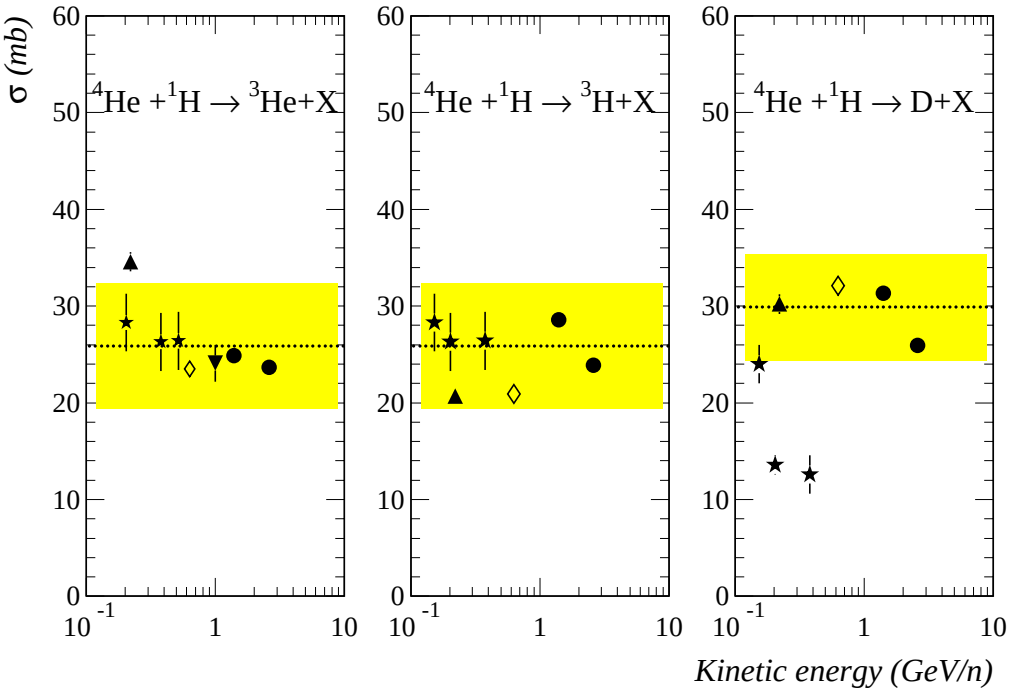

Figure 3.3: *Partial fragmentation cross-section for ^{4}He projectile on hydrogen target ([52, 53, 54, 55, 56]).*

fragmentation cross-section for the production of ^{3}He is same as that of ^{3}H. This is a reasonable expectation, since in both cases the reaction consists in the nucleon stripping from a nucleus with the same number of protons and neutrons. Therefore, the partial fragmentation cross-sections for the production of ^{3}H and ^{3}He have been assumed to be the same; the mean value is shown in fig. 3.3 by the dotted line. The mean value of the cross-section for deuterium has been obtained by excluding the Webber measurement.

The partial fragmentation cross-section trend for the collision of ^{4}He with hydrogen target has been extended to ^{4}He on carbon target. Beside the work of Webber[52], only one recent measurement is available for carbon target [57]. This measurement has been used in this calculation to evaluate the energy independent partial fragmentation cross-sections. These values, presented in the first row of tab. 3.1, show that the production of deuterium is much larger than the production of ^{3}H and ^{3}He for carbon target with respect of hydrogen target. This behavior is not unreasonable, since the probability of fragmentation is higher on carbon target than on hydrogen ta[57] rget, leading to the production of a larger amount of lighter fragments. For the production of ^{3}H and

Table 3.1: *Measured partial fragmentation cross-sections (in mb) for ^4He and ^{12}C projectiles with ^{12}C as the target.*

Reaction	Kinetic energy (GeV/n)	Fragment ^{4}He	^{3}He	^{3}H	D	Reference
^{4}He+^{12}C	4.5	-	49±8	58±9	91±27	
^{12}C+^{12}C	1.05	404±36	135±8	118±7	292±24	[51]
	2.1	373±33	125±7	129±11	314±28	[51]

^{3}He a mean cross-section value of 53.5 mb has been used. We have scaled the partial fragmentation cross-sections to air target, as described in section 3.3.1, using ^{4}He+Al data [57].

Measurement of the deuterium production from the ^{3}H and ^{3}He fragmentation are available for hydrogen target only [53]. The following two approaches have been considered to estimate the cross-sections on air target:

1. using the same scaling factor for deuterium production cross-section from ^{4}He projectile, from hydrogen target to air target;

2. using the same scaling factor for ^{3}H and ^{3}He production cross-sections from ^{4}He projectile, since the production of deuterium from ^{3}H and ^{3}He involve the stripping of one nucleon.

The obtained scaling factor values are 3 and 2.4. It may be pointed out that the total interaction cross-section for ^{3}He with hydrogen is 118.0 mb, while that of ^{4}He is 152.5 mb. The cross-section ratios

$$\frac{\sigma_{^3He+H\rightarrow D+X}}{\sigma'_{^3He+H}} \sim 0.295\,, \tag{3.22}$$

$$\frac{\sigma_{^4He+H\rightarrow D+X}}{\sigma'_{^4He+H}} \sim 0.170\,, \tag{3.23}$$

$$\frac{\sigma_{^4He+H\rightarrow ^3He+X} + \sigma_{^4He+H\rightarrow ^3H+X}}{\sigma'_{^4He+H}} \sim 0.312\,, \tag{3.24}$$

suggest that the deuterium production from ^{3}He, due to the stripping of one nucleon, is analogous to the ^{3}H and ^{3}He production from ^{4}He. We thus followed the second approach.

To estimate the production of ^{4}He, ^{3}He, ^{3}H and deuterium from heavy nuclei, the partial fragmentation cross-sections of ^{12}C projectiles with carbon target have been used. Two measurements are available, at 1.05 GeV/n and 2.1 GeV/n respectively (see tab. 3.1). Following the same approach used for ^{4}He spallation, we have assumed an energy independent partial fragmentation cross-section, with a mean value of 388.5 mb and 303 mb for ^{4}He and deuterium production respectively, and a mean value of 127 mb for both ^{3}He and ^{3}H. These values have been scaled to air target using ^{12}C+Al data [51].

All the values for partial fragmentation cross-sections used in the calculation are summarized in tab. 3.2.

Table 3.2: *Partial fragmentation cross-sections (in mb) scaled to air target used in the calculation.*

Reaction	Fragment		
	^{4}He	^{3}He,^{3}H	D
^{12}C+air	404±38	132±9	323±29
^{4}He+air	-	57±10	95±30
^{3}He,^{3}H+air	-	-	83.5±14

In equations 3.12 and 3.13 we have introduced the mean number of free protons $\langle p \rangle_i$ and neutrons $\langle n \rangle_i$ produced from the fragmentation of a nucleus of type i. It is difficult to find reliable data in literature on these parameters, due to some disagreements in the definition of projectile fragmentation protons [57]. In nucleus-nucleus interactions projectile fragments, consisting of two or more nucleons, are collimated in the forward direction and they can be identified by their kinetic energy per nucleon, which is very similar to that of the incident nucleus. On the contrary, it is extremely difficult, from the energy and angular characteristics of interaction products, to distinguish among protons coming from the projectile fragmentation and knock-on protons of the target nucleus. The parameters $\langle p \rangle_i$ and $\langle n \rangle_i$ have thus been evaluated from the relation:

$$\langle p + n \rangle_i = A_i - \sum_f \frac{\sigma_{i \to f}}{\sigma'_i} \,, \tag{3.25}$$

where $\sigma_{i \to f}$ is the inclusive cross-section for the production of a fragment of type f from the fragmentation of a nucleus of mass number A_i. By using the inclusive cross-section values presented in tab. 3.1 and by considering the deuterons as a free neutron and a

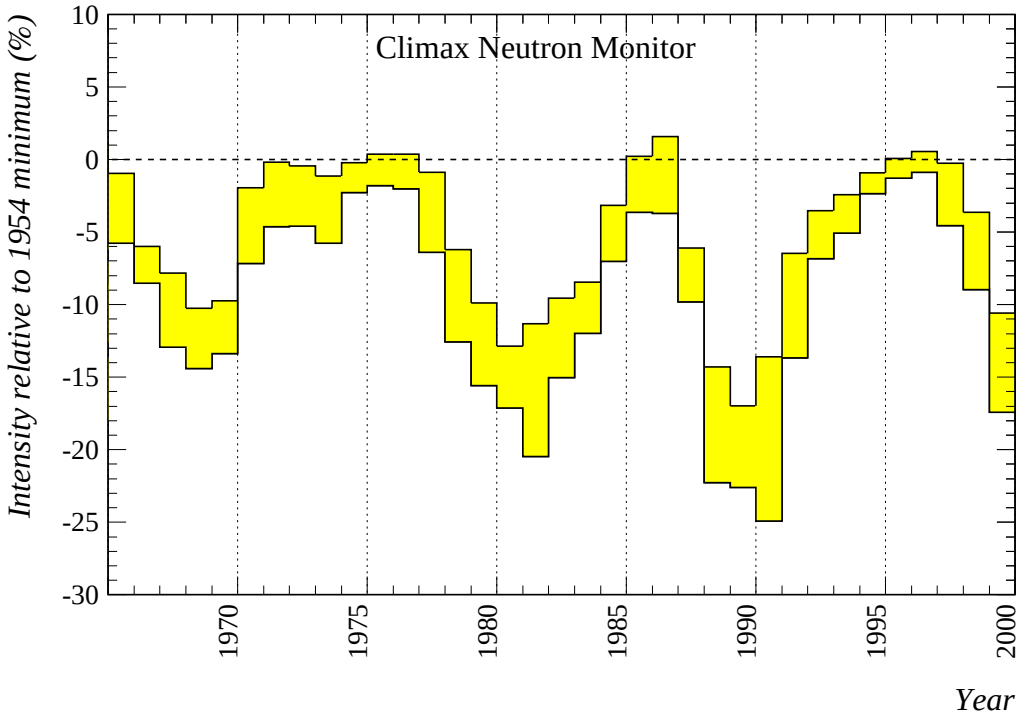

Figure 3.4: *Yearly averaged Climax neutron monitor flux (Courtesy of the National Science Fundation Grant ATM-9912341, University of Chicago). The shaded band represents the root mean square around the mean value.*

free proton, the estimated mean number of free nucleons produced per interaction is 3.3 and 6.7 for ^{4}He and ^{12}C, respectively. We have assumed that the same number of neutrons and protons are produced.

3.4 Flux of primaries

In order to solve the transport equations for nucleons and nuclei in the atmosphere (eq. 3.12-3.16), the energy spectra of primary proton, helium and carbon cosmic rays at the top of atmosphere have to be known as input data.

In this calculation different conditions of solar modulation have been considered, deriving a set of simple analytic expressions for the primary fluxes from experimental data.

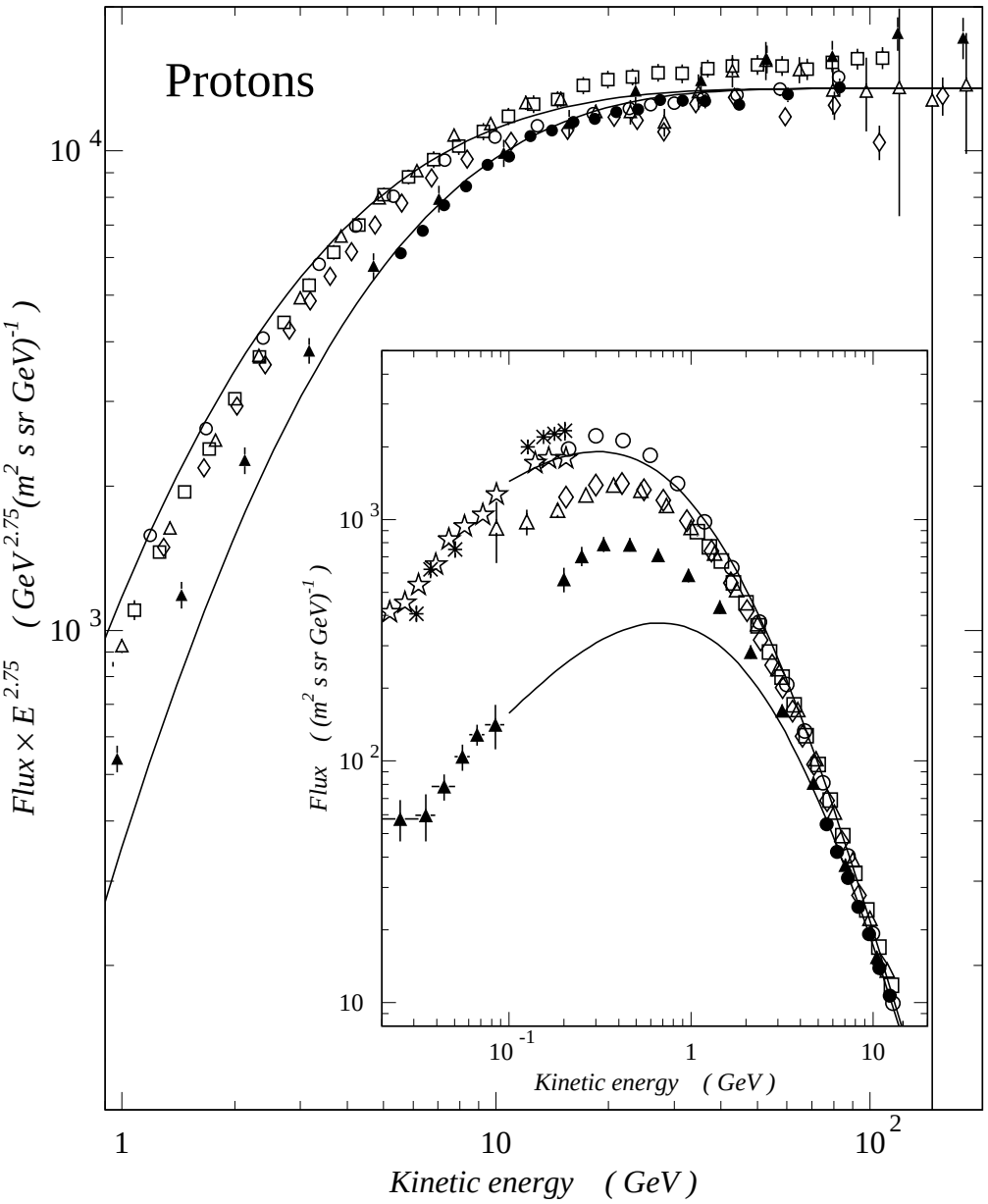

Figure 3.5: *Cosmic-ray proton flux. Symbols: results from several experiments (see tab. 3.3 for references). Solid curves: parameterization of the proton flux at minimum (upper curve) and maximum (lower curve) solar modulation level.*

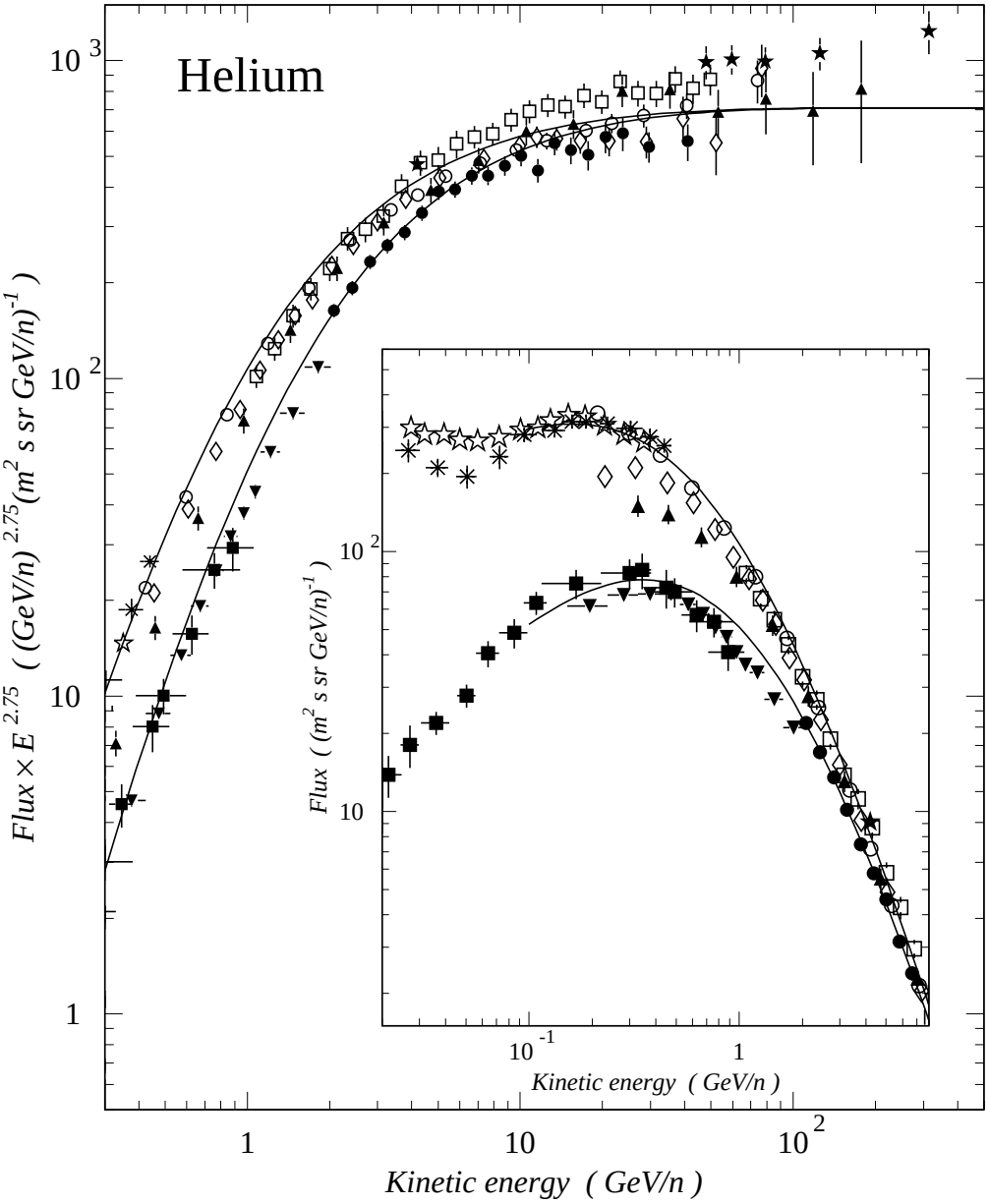

Figure 3.6: *Cosmic-ray helium flux. Symbols: results from several experiments (see tab. 3.3 for references). Solid curves: parameterization of the helium flux at minimum (upper curve) and maximum (lower curve) solar modulation level.*

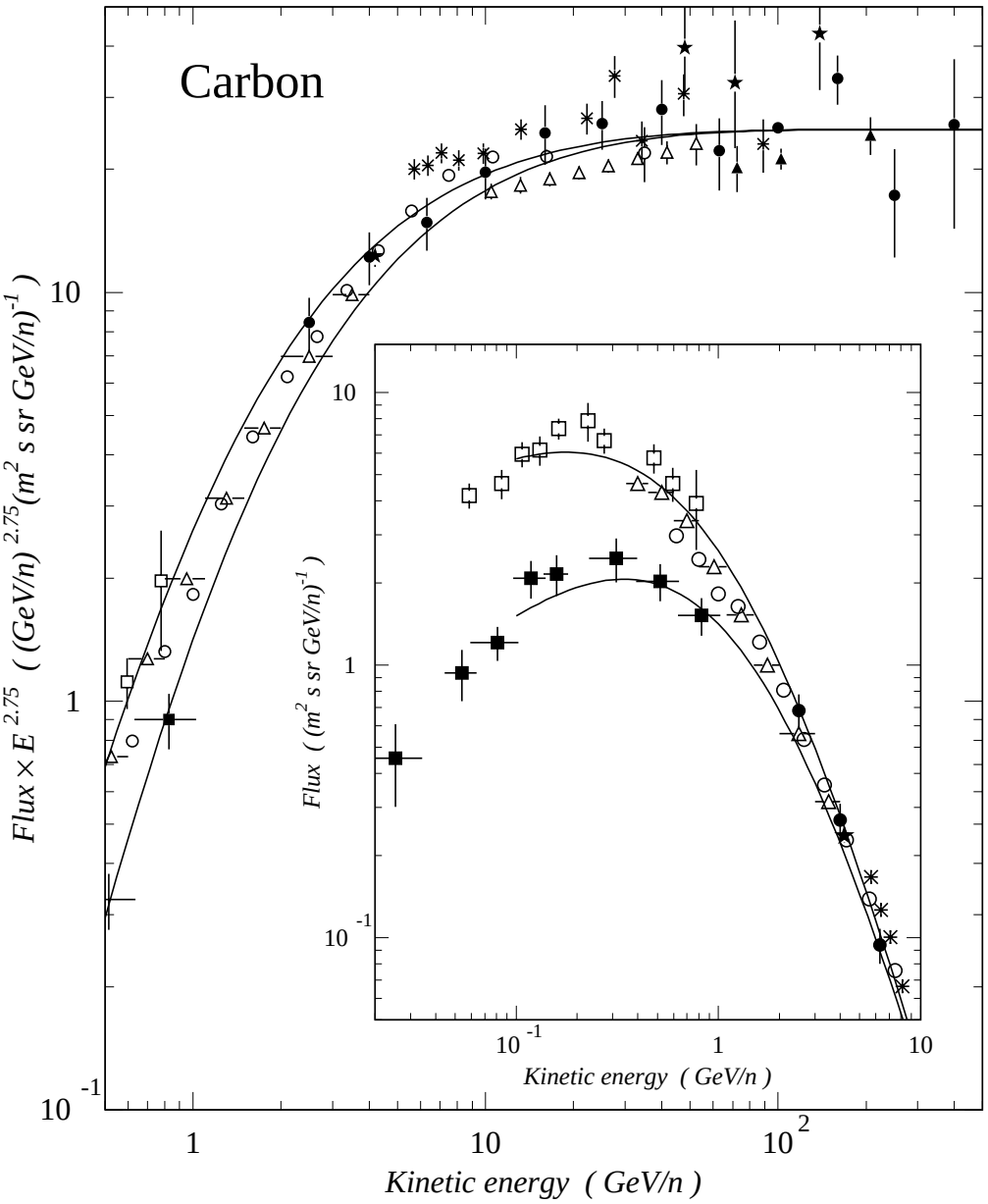

Figure 3.7: *Cosmic-ray carbon flux. Symbols: results from several experiments (see tab. 3.3 for references). Solid curves: parameterization of the carbon flux at minimum (upper curve) and maximum (lower curve) solar modulation level.*

3.4.1 Solar modulation

Figures 3.5-3.7 show the differential flux of protons, helium and carbon in the energy range from few tens of MeV/n up to hundred GeV/n. The references corresponding to given in tab. 3.3, while fig. 3.4 shows the Climax neutron monitor[3] data during the period covered by the measurements taken into consideration here. The collection of data includes all experiments carried out from the 1987 solar minimum for protons and helium, and from the 1973 solar minimum for carbon. We also included older measurements, down to the 1969 solar maximum, in order to determine the role of the solar modulation on the low energy cosmic-ray fluxes. It can be noticed that data are consistent with the solar activity indicated by the Climax neutron monitor.

The solid curves in fig. 3.5-3.7 represent the upper and lower extremes of solar modulation obtained by interpolating experimental data with the following relation:

$$J(E) = A\ (E + Be^{-\beta E})^{-\gamma-\alpha}\ E^{\alpha} \quad (\ m^2\ s\ sr\ GeV/n\ )^{-1}\ . \tag{3.26}$$

The obtained parameters are presented in tab. 3.4.

From the observed cosmic-ray abundances [76], it has been found that the flux of HN is equivalent to ~ 3.80 times the carbon flux.

3.5 Results

Fig. 3.8 shows how different production processes (solid curves) contribute to the overall deuterium energy flux at an atmospheric depth of 5 g/cm^2 in the vertical direction and at solar minimum. At low energy the deuterium production is dominated by the air nucleus fragmentation. The shape of the spectrum in this energy region reflects essentially that of the emitted fragments (eq. 3.5). This process dominates up to about $\sim$ 1 GeV/n. Deuterium production from incident nucleons gives a non-negligible contribution at very low energy only (up to about $\sim$ 300 MeV/n). The structures present in the spectrum resulting from this process are due to kinematic effects. In

[3]The purpose of the neutron monitor is to detect, deep within the atmosphere, variations of intensity in the interplanetary cosmic-ray spectrum through the measurement of the intensity of secondary particles produced by interaction with the air nuclei. Contrary to protons, atmospheric secondary neutrons are not slowed by ionization loss, so that the interaction rate in the atmosphere is more reliably measured by detecting neutrons. Because of the decreasing of the cosmic-ray energy spectrum the neutron intensity is more sensitive to the low energy range of the primary spectrum, so that these data are useful to monitor the solar activity.

Table 3.3: *Cosmic-ray primary flux reference list. Column 2 indicates the year when each experiment was carried out. The symbol * indicates the measurements performed during maximum solar modulation level.*

Reference	Year	Flux	Symbol
Alcaraz J. *et al.* [58]	1998	p	△
Sanuki T. *et al.* [59]	1997	p,He	□
Boezio M. *et al.* [60]	1994	p,He	◊
Menn *et al.* [61]	1992	p,He	▲
Bellotti R. *et al.* [62]	1991*	p,He	●
Buckley J. *et al.* [63]	1991*	He,C	★
Beatty J. J. *et al.* [64]	1989*	He	▼
Seo E. S. *et al.* [65]	1987	p,He	○
Müller D. *et al.* [66]	1985	C	▲
Engelmann J. J. *et al.* [67]	1980*	C	○
McDonald F. B. *et al.* [68]	1978	p,He	❋
von Rosenvinge T. T. *et al.* [69]	1978	p,He	☆
Lezniak J. A. *et al.* [70]	1976	C	△
Simon M. *et al.* [71]	1976	C	●
Caldwell J. H. [72]	1973	C	❋
Garcia-Munoz M. *et al.* [73]	1973	C	□
Mason G. M. *et al.* [74]	1969*	He,C	■
Hsieh K. C. *et al.* [75]	1969*	p	▲

particular the peak at $\sim$ 200 MeV/n corresponds to deuterium production in the forward direction in the center-of-mass system (see eq. 3.7). At higher energy the incident nucleus spallation process dominates. Deuterium is mainly produced by ^{4}He, even if heavier nuclei play a significant role. Production from ^{3}H and ^{3}He is negligible at small atmospheric depths. The dashed curves in fig. 3.8 show the attenuation terms. It can be noticed that at low energy the main contribution comes from the energy loss by ionization. The ionization energy loss becomes negligible for increasing energy and above ~ 1 GeV/n the deuterium attenuation length is given by the interaction length λ'_D.

In fig. 3.9 the deuterium atmospheric growth curves (thick solide curves) in the vertical direction are shown, for two values of the kinetic energy. In the same plots the growth curves for the different production and attenuation processes are also shown. About the production processes (solid curves), the relative contributions remain essentially unchanged for increasing atmospheric depth up to 80 g/cm^2. The only production

Table 3.4: *Parameters of the primary flux described by eq. 3.26, for minimum (min) and maximum (max) solar modulation level.*

	A	B		α		β
		min	max	min	max	
p	13500.	1.09	1.83	0.72	0.90	0.065
He	710.	0.79	1.10	0.55	0.85	0.020
C	25.	1.05	1.35	0.45	0.67	0.025

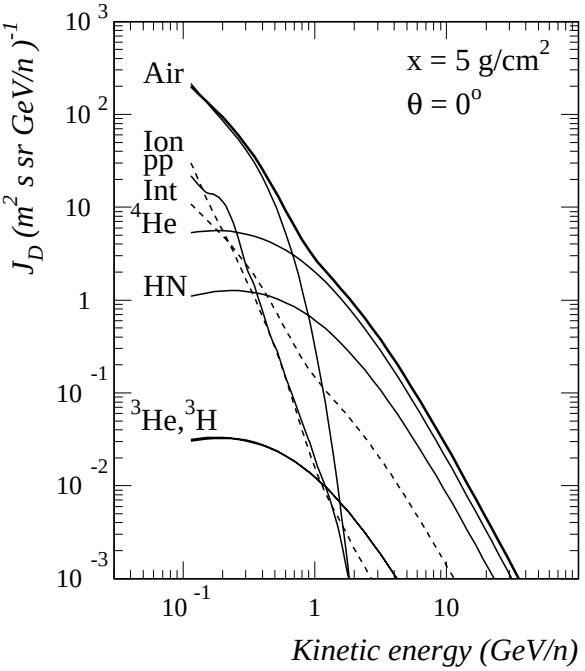

Figure 3.8: *Processes contributing to the flux of deuterium at an atmospheric depth of 5 g/cm^2 in the vertical direction at solar minimum. Solid thick line: total flux. Solid lines: production from air target nuclei (Air), incident nucleons (pp) and nuclei (^{3}H, ^{3}He, ^{4}He and HN). Dashed lines: loss of deuterons for energy loss by ionization (Ion) and interactions (Int).*

process that gives an increasing relative contribution for increasing x is the ^{3}H and ^{3}He spallation. The deuterium component produced by this process remains negligible at low energy, while at high energy and large atmospheric depth becomes comparable with the production from heavy nuclei. The attenuation terms (dashed curves) give a contribution that increases for increasing atmospheric depth. When the absolute value of the attenuation term equals the total production term, the flux begins to decrease. At high energy, where the attenuation is determined by particle loss for interactions, the deuterium flux starts to decrease at $x \sim 50$ g/cm^2. At low energy the ionization losses are comparable with the interaction process, so that the attenuation begins at an atmospheric depth of ~ 40 g/cm^2.

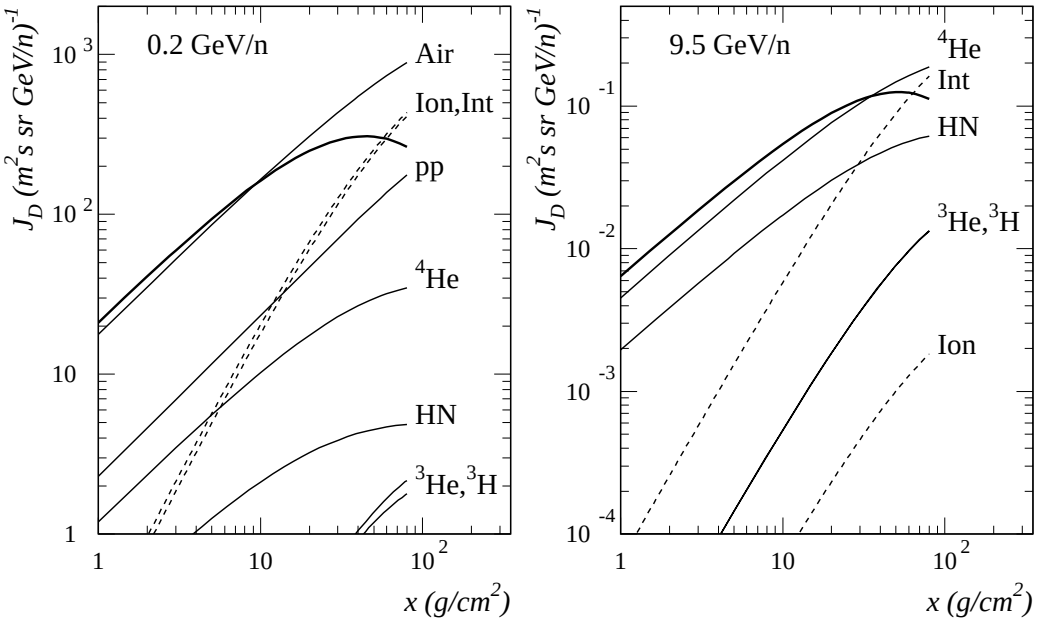

Figure 3.9: *Deuterium atmospheric growth curves at different energies in the vertical direction at minimum solar modulation level. The contributions from different production and attenuation processes are also shown, using the same notation of fig. 3.8.*

Fig. 3.10 shows the deuterium energy spectrum in the vertical direction, up to 40 g/cm^2, at minimum and maximum solar modulation level. As expected, the solar modulation affects the secondary deuterium flux mainly at low energy, resulting in a lower flux for greater solar activity. The flux has been multiplied by E^2 in order to better show the structures in the deuterium spectrum due to the different dominant production processes as a function of the energy.

Fig. 3.11 shows the deuterium flux as a function of the zenith angle, normalized to the flux in the vertical direction. At high energy (right plot), where the spallation process dominates, the deuterium is essentially produced in the forward direction. It follows that, for a given atmospheric depth and direction, the deuterium flux is approximately proportional to the path length, $l = x \sec\theta$, of nuclei through the atmosphere. This proportionality does not hold any more when the deuterium or the incident nuclei begin to attenuate. Since deuterium is mainly produced by ^4He and both have nearly the same interaction length, this occurs when $l \sim 50$ g/cm^2, that is, for example at an atmospheric depth of about 5 g/cm^2, when $\sec\theta \sim 10$. For increasing depths the maximum of the flux moves toward lower zenith angles, up to a depth $x \sim 50$ g/cm^2.

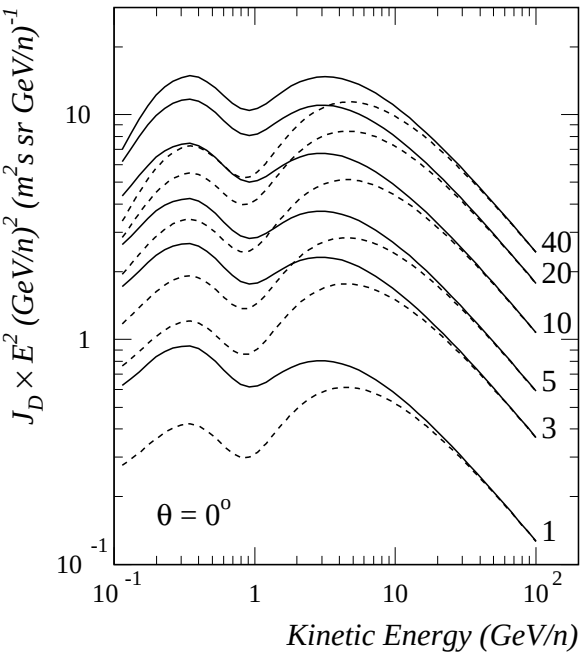

Figure 3.10: *Calculated deuterium energy spectrum in the vertical direction at various atmospheric depth (g/cm^2). Solid curves: minimum solar modulation level. Dashed curves: maximum solar modulation level.*

Starting from this depth the flux, if compared with the value in the vertical direction, decreases for increasing zenith angles.

At lower energies (left figure) the production from air target nuclei dominates. Deuterium is still mainly produced in the forward direction [29], therefore the same arguments used for the high energy flux can approximately be applied. Notice that the position of the maximum is determined by the attenuation length which is now affected by ionization losses. For increasing zenith angles the flux does not decrease but flattens. This is a consequence of the isotropic component in the production term [29], which results in a fraction of the produced deuterium to be emitted in any direction.

Fig. 3.11 shows that the angular dependence of the secondary deuterium at low energy depends on the solar modulation level. In particular, at a given depth x, the ratio between the flux in the direction θ and the flux in the vertical direction is larger at solar maximum. This is due to the fact that at large angles there is only the contribution from the isotropic component of the air target fragmentation. The relative difference between the deuterium flux at the extremes of solar modulation is related essentially to the relative difference between the integral primary flux above 1 GeV/n, because of the weighting factor $\omega(E')$ in the air production term (eq. 3.5).

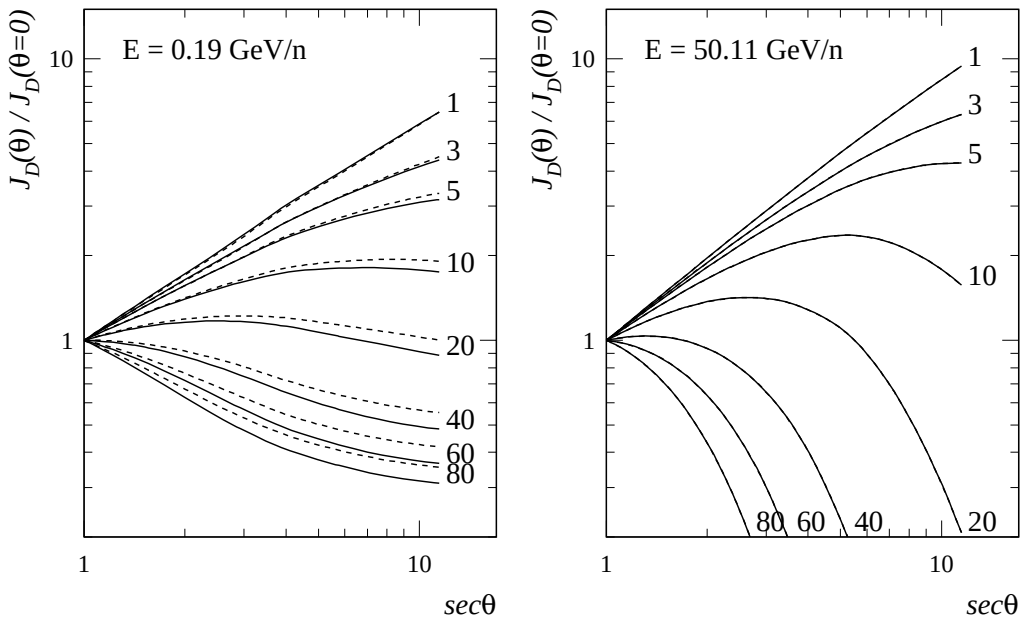

Figure 3.11: *Deuterium flux, normalized to the flux in the vertical direction, as a function of the zenith angle, for two different energy values. Solid lines: minimum solar modulation level. Dashed lines: maximum solar modulation level.*

In the vertical direction there is also a small contribution from the spallation of mainly ^{4}He. In this case the amount of deuterium produced is related to the differential helium flux at low energy that is much more affected by solar modulation with respect to the integral flux above 1 GeV/n. As a result, the flux in the vertical direction suffers a slightly larger variation than the flux at large angles, as it can be seen in fig. 3.11.

3.5.1 Conclusions

From the result of our calculation it is inferable that the dominant processes contributing to the deuterium atmospheric production are the spallation of cosmic-ray helium and heavier nuclei, above 1 GeV/n, and the fragmentation of air target nuclei, below 1 GeV/n. In particular, the former process results in a large amount of deuterons, which increases for decreasing kinetic energy. However, a reliable estimate of this low energy contribution is difficult to carry out, because of the lack of experimental data on the production of light target fragments in nucleon-nucleus and nucleus-nucleus reactions. Notice that the parameterization used for the angular distribution and the

spectrum of the emitted deuterons is derived from old nuclear emultion data [27] and it is subject to large uncertainties in the absolute normalization, which are difficult to evaluate. The same limitation holds for the contribution from the spallation of cosmic-ray helium. For this component the only high energy result of reference [57] has been used.

In this work we have proposed a method to calculate the secondary deuterium flux in the atmosphere, by taking into account all significant production and attenuation processes. This method allows to determine both the spectrum and the angular distribution of the deuterons. Uncertainties on nuclear cross-sections presently available constitute the main limitation for a correct estimate of the deuterium flux.

This calculation can be extended to heavier fragments such as ^3H and ^3He, and different target materials, by taking into account the proper nuclear reactions. Possible applications of this method, different from the atmospheric corrections for balloon-borne experiments, might be the cosmic-ray propagation in shielding materials and also in the interstellar medium.

Chapter 4

The CAPRICE98 experiment

CAPRICE98 is a balloon-borne experiment whose main scientific objective has been the study of cosmic-ray antiprotons. Beside this, the instrument configuration allows to obtain other scientifically significant results. Among these, are included the deuterium and ^3He abundance measurements at high energy. The present work is dedicated to the deuterium analysis, while the ^3He analysis will be pursued in the future, by extending to it the procedure developed for the deuterium.

In this chapter the CAPRICE98 apparatus is described, giving more relevance to those features directly involved in the deuterium analysis. In section 4.1 the instrument working concept is introduced. In the following sections 4.2-4.4 the CAPRICE98 detectors are described from the technical point of view and their basic performances are shown. Given the relevance of the RICH detector for the deuterium analysis, this instrument is discussed in greater detail.

4.1 Introduction

CAPRICE98 (Cosmic AntiParticle Ring Imaging Cherenkov Experiment, 1998) is the latest balloon-borne experiment carried out by the WiZard collaboration, whose primary objective is to study the antimatter component in cosmic rays by means of balloon and satellite-borne experiments. The balloon activity of the Wizard collaboration started in 1989 with MASS89, motivated by the recent discovery of the antiproton component in cosmic rays [9, 7]. This instrument was composed of a superconducting magnet spectrometer, a brass-streamer calorimeter and a gas Cherenkov detector. A new flight was performed in 1991 (MASS91) with an improved version of the previous telescope. In 1993 the Cherenkov detector and the calorimeter were replaced with a

Transition Radiation Detector (TRD) and a silicon-tungsten calorimeter, respectively. The aim of this new instrument (TS93) was to extend the positron search at high energy. The first CAPRICE flight was performed in 1994. The instrument concept was the same of TS93, with the difference that the TRD was replaced with a solid Ring Imaging CHerenkov (RICH) detector and the calorimeter was modified in order to increase the total radiation length.

CAPRICE98 is the evolution of CAPRICE94. In this new configuration the solid RICH detector was replaced by a gas RICH one and the tracking system was modified. The experiment flew from FT. Sumner, New Mexico, USA (34°N, 104°W) on 28th of May, 1998 [77]. The balloon flew under a residual atmosphere of 5.5 g/cm^2 for about 20 hours, collecting more than 5 millions events. The effective vertical cutoff for this location is $\sim$ 4 GV, hence CAPRICE98 was able to collect cosmic particles with rigidity above this value.

4.1.1 The CAPRICE98 science objectives

The main scientific objectives of the CAPRICE98 experiment have been:

- the measurement of the antiproton flux up to the energy of 50 GeV [78];
- the measurement of the positron component up to the energy of 30 GeV [80].

Antiprotons are present in the cosmic radiation as a product of interactions between the cosmic rays and the interstellar matter. The study of their abundance thus provides important information concerning the propagation mechanism of cosmic rays in the Galaxy. Moreover, antiprotons can be produced by primary or exotic sources hypothesized by several theories. Many other previous experiments studied the cosmic-ray antiproton, the most of them at energies below 4 GeV. Beyond this energy only few results exist, which differs by a large amount. A similar scenario holds for the positron component. The CAPRICE98 instrument was designed with the specific aim to extend the experimental knowledge on the positron and antiproton flux up to the less explored high energy region.

Beside the antimatter study, the instrument configuration allows other science goals:

- the measurement of the primary proton and helium spectra up to energies $\sim$ 300 GeV/n [81];

- the particle composition as a function of the atmospheric depth, with special focus on muons [82].

An accurate knowledge of the spectral shape of primary cosmic rays provides useful information to understand the mechanism of production and propagation of cosmic rays in the Galaxy. Beside this, the absolute normalization of the cosmic-ray flux and the spectrum of atmospheric muons, as a function of the atmospheric depth, are basic parameter to get reliable predictions for the atmospheric neutrino flux.

As will be shown afterwards, a further scientific result that CAPRICE98 can provide concerns

- the light isotopes D and ^3He abundance measurement at high energy.

As discussed in chapter 2, light secondaries are powerful tools to test propagation models, since their interaction length is considerably longer than the escape mean free path of cosmic rays from the Galaxy. Moreover, the CAPRICE98 experiment can give results in an energy range scarcely covered by previous experiments.

4.1.2 The CAPRICE98 apparatus

Since antimatter is a rare component in cosmic rays, a very good particle identification capability is required, due to the presence of a large quantity of protons, electrons, muons and pions which are the background in the antiproton and positron analysis. For this reason the CAPRICE98 apparatus was designed to efficiently identify particles in a wide energy range, from few hundred MeV up to some hundred GeV. This has been carried out by means of several detectors. Fig. 4.1 shows a schematic view of the payload in the 1998 configuration. The apparatus included, from top to bottom: a RICH detector, a Time-Of-Flight system (TOF), a superconducting magnet spectrometer equipped with three drift chamber, and a silicon-tungsten calorimeter.

Before going through the technical description of each detector, it is useful to introduce briefly the general working concept of the CAPRICE98 telescope. For each recorded event, both the particle magnetic rigidity R, defined as $R = pc/\mid Ze \mid$, and the sign of the electric charge are obtained by reconstructing the track inside the spectrometer. The absolute value of the charge Z is given by the measurement of the ionization energy loss inside the TOF scintillators. Given R and Z, the detected particle can be mass resolved by means of the independent measurement of another kinematical

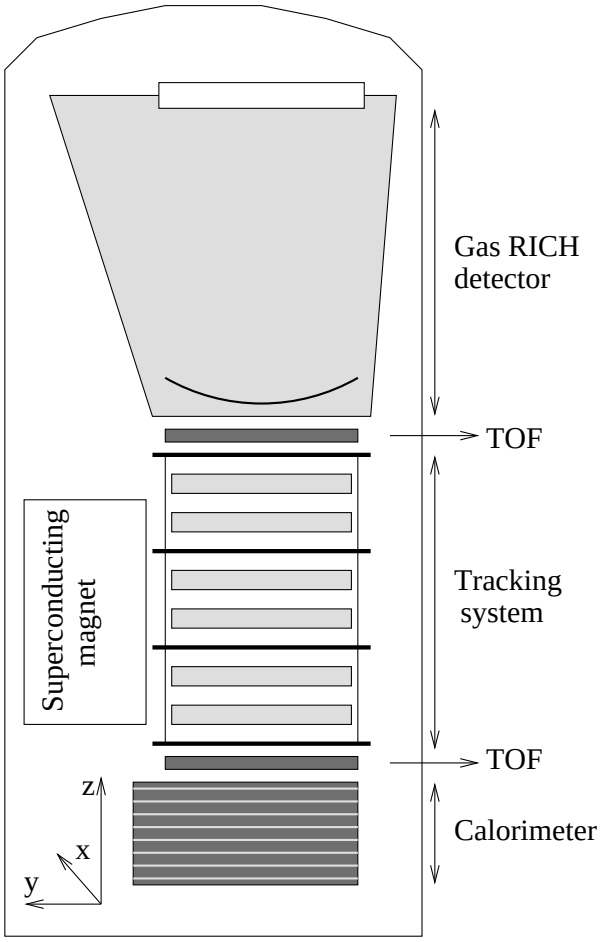

Figure 4.1: *Schematic view of the CAPRICE98 payload. On the bottom left corner of the picture is indicated the payload reference system, to which we will refer here and in the following. The outer shell was* 4.3 *m tall and* 1.6 *m wide. It contained, from top to bottom, a gas Ring Imaging CHerenkov (RICH) detector, a Time-Of-Flight (TOF) system, a tracking system, equipped with three drift chamber, and a silicon-tungsten electromagnetic calorimeter. On the left side of the tracking system is placed a superconducting magnet, which provided a magnetic field whose main component is parallel to the y axis. We will thus refer, in the following, to x as the bending view and to y as the non-bending one.*

quantity. This is fulfilled essentially through the measurement of the particle velocity (β), performed by using the TOF system and the gas RICH detector information, at low and high energy respectively. The RICH detector can be used also as a threshold device, giving a criterion to identify the particles. Further information for the identification is given by the imaging calorimeter, which, through the reconstruction of the energy release path, is used to separate interacting from non interacting particles and, among the interacting ones, electromagnetic particles from hadrons.

An essential feature of the CAPRICE98 apparatus is the redundancy of information coming from the different detectors. First of all, this allows to measure the efficiency of each detector by using directly flight data. This subject will be discussed in more detail in chapter 5, where the selection criteria for the deuteron analysis are described and the corresponding selection efficiencies are estimated. More generally, the redundancy enables to study the performances of a given detector by cross-checking its response with that one obtained independently by other detectors. As will be shown in chapter 6,

part of the presented analysis is based on this feature. In particular, the independent rigidity information given by the RICH detector has been used to parameterize the spectrometer response. The advantage of such approach is that the obtained results directly reflect the in-flight behavior of the instrument, so that these results can be applied to data without any assumption on the working conditions of the detectors.

The following sections are dedicated to the description of the CAPRICE98 detectors, from the point of view of both their technical characteristics and of their role in the contest of the experiment. Greater relevance is given to those sections describing the spectrometer and the RICH detector characteristics, since the deuterium analysis is based on these detectors. The features, relevant to this purpose, are highlighted in the following. In chapter 6 we will deal with a more exhaustive discussion on their performances finalized to the deuterium analysis.

4.2 The TOF system

The CAPRICE98 TOF system consists of two scintillator planes, placed above and below the tracking system, respectively (see fig. 4.1). Each plane is composed of two 25×50 cm^2 plastic scintillating paddles, each one viewed edge-on by two phototubes. The distance from the two planes is 1.19 cm. The TOF time resolution is 230 ps.

The signal coming from the scintillators provides both time and energy loss information. This signal was also used to generate the trigger for the data acquisition, which started when a four-fold coincidence between the two photomultipliers in one of the top and the bottom scintillator paddles occurred.

The amplitude of the signal, which is proportional to the energy loss inside the scintillator, gives the absolute value of the electric charge of a traversing particle. The time-of-flight information gives its direction and velocity (β). This provides both low energy particle identification and albedo (up-going) particle rejection.

4.3 The magnetic spectrometer

The spectrometer plays a basic role for the experiment, since it provides information on the particle rigidity. In order to study cosmic-ray flux up to energies of several tens of GeV, a high magnetic field and a tracking system with a good spatial resolution are required. The CAPRICE98 magnetic spectrometer is composed of three drift chambers

in the high field region of a superconducting magnet [85], which was the same one used in the previous experiments of the collaboration. The drift chambers were developed for the IMAX balloon-borne experiment [84] and have been used by the WiZard collaboration since then. They were designed to achieve the required spatial resolution in the presence of a strong magnetic field, while satisfying the mechanical constraints for a balloon-borne experiment.

4.3.1 The instrument

The magnet

The magnetic field inside the tracking volume was provided by means of a superconducting magnet [85]. It consists of a single coil of 11161 turns of copper-clad Nb-Ti wire, which has an inner and outer diameter of 36 cm and 61 cm, respectively, and an axial thickness of 7.6 cm. The coil is placed in a dewar filled with liquid helium surrounded by a vacuum jacket. The only thermal contact with the support structure is through a second dewar filled with liquid nitrogen that, through the reduction of the evaporation of liquid helium, permitted to reach a lifetime of the superconducting state of ~ 100 hours. The operating current was 120 A, producing an inhomogeneous field of approximately 4 T at the center of the coil. Inside the tracking volume the magnetic field was lower. Its intensity varied from a highest value of about 1.8 T down to a value of 0.1 T at the chamber corners furthest away from the magnet.

The strength of the field has been calculated and measured over all the apparatus volume and a magnetic field map has been constructed [86]. In this way the track reconstruction algorithm, described in section 4.3.2, can quickly calculate the field strength in every part of the instrument.

The drift chambers

Each drift chamber box [86] is made of 1 cm thick epoxy-composite lateral plates covered with two 0.7 mm thick mylar entrance windows on the top and bottom sides respectively, for a total inner volume of $47 \times 47 \times 35$ cm^3. The chambers are operating with pure CO_2 gas, chosen because the electron drift velocity is small compared to that of common drift chamber gases. This minimizes the action of the Lorentz force during the electron drift path, which could affect the spatial resolution. The effect of the magnetic field is in fact the distortion of the electron drift path. Previous studies of

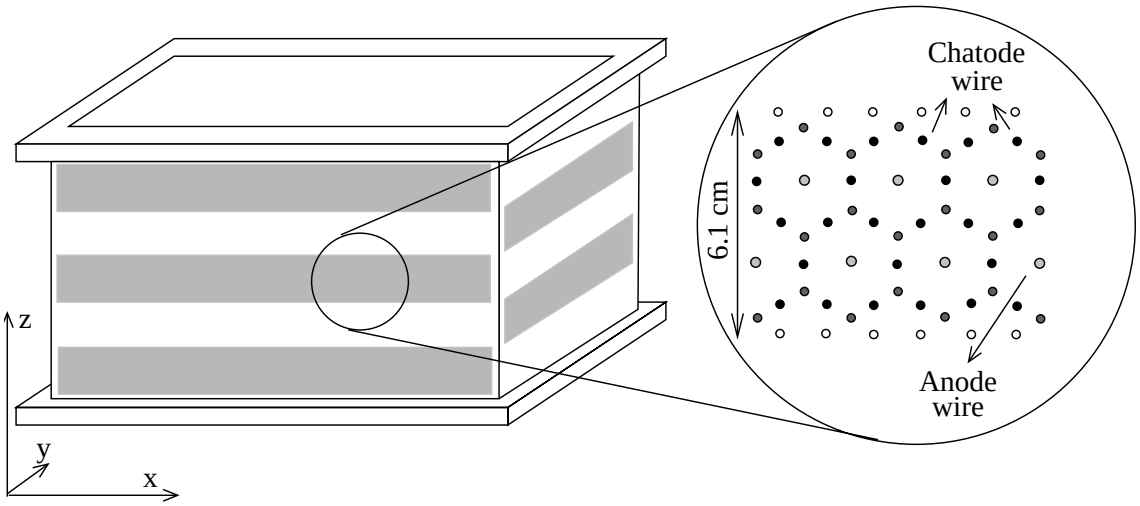

Figure 4.2: *Schematic view of a drift chamber module. The expanded view illustrates the wire cell structure of each layer.*

the drift chamber performances have shown that this instrument configuration allows little or no loss of spatial resolution when it is operating in a strong inhomogeneous field [86]. During the balloon flight the volume was flushed with the CO_2 gas, in order to maintain a constant pressure inside the boxes. Each box contains 5 double layers of sense-wires arranged in order to give 6 position measurements in the bending view (x) and 4 in the non bending view (y) (see fig. 4.2). Each double layer is composed of two adjacent arrays of 16 hexagonal drift cells, shifted of half a cell. In fig. 4.2 the hexagonal-close-packed structure of a layer is shown. A drift cell is composed of a central anode wire surrounded by cathode and potential wires that are shared between adjacent cells. With this arrangement the electric field lines and, as a consequence, the lines of equal drift time are symmetric over most of the cell [86].

When a ionizing particle crosses a cell, the released electrons drift to the anode wire under the influence of the applied electric field. The output signal of the detector is the drift time. From this quantity the distance between the particle track and the anode wire is calculated by means of the relation between the drift time and the drift path, obtained from experimental data [84]. The achieved spatial resolution is shown in fig. 4.3 as a function of the drift path. As can be seen, the overall performance is quite good, being the spatial resolution better than 100 μm over most of the possible drift paths.

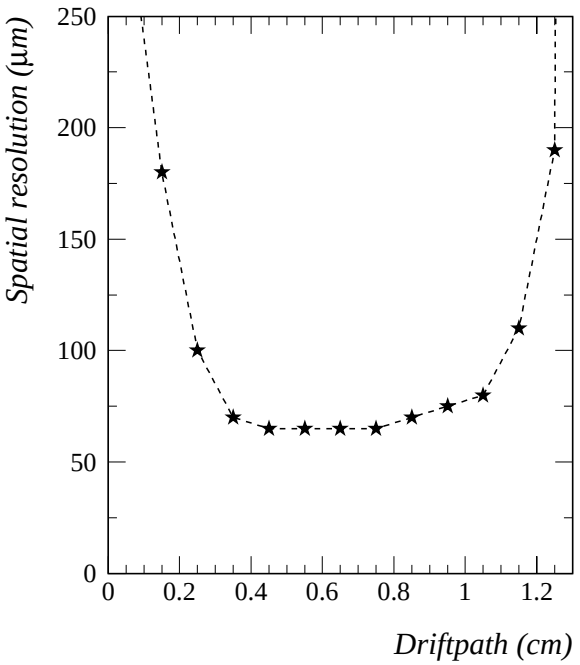

Figure 4.3: *The measured drift chamber spatial resolution as a function of the drift path.*

4.3.2 The track fitting procedure

The physically significant parameter measured by the spectrometer is the particle rigidity R. This parameter is determined by applying an iterative least squares procedure, whose detailed description can be found in reference [87]. In the fitting procedure the track is uniquely described by a state vector of five components, defined as follows:

$$\alpha = \left(x_b, y_b, \left(\frac{\partial x}{\partial z}\right)_b, \left(\frac{\partial y}{\partial z}\right)_b, \eta \right) \ . \tag{4.1}$$

The components of the state vector α express respectively the coordinates in the bottom plane of the tracking system, the two directional tangents and the magnetic deflection η, defined as $\eta = 1/R$. Given the state vector, the particle trajectory through the tracking volume is calculated by a stepwise integration of the equations of motion, performed using the magnetic field map. For each calculated trajectory, an estimate of the state vector α is obtained by minimizing the corresponding χ^2, that has the following expression:

$$\chi^2 = \chi^2_x + \chi^2_y = \sum_{i=1}^{N_{planes}} \left[\left(\frac{x_i - x_i^{meas}}{\sigma} \right)^2 + \left(\frac{y_i - y_i^{meas}}{\sigma} \right)^2 \right] \ . \tag{4.2}$$

In eq.4.2, x_i and y_i are the calculated coordinates in each tracking plane, x_i^{meas} and y_i^{meas} are the measured ones and σ is the spatial resolution shown in fig. 4.3. Starting from an initial guess of the state vector, the procedure is repeated until the result stabilizes.

The fitting routine calculates for each event also the errors on the parameters (for a description of how these quantities are computed see [87]). The most significant parameter is the uncertainty on magnetic deflection. This quantity, σ_η, defines the spectrometer resolution and it is related to the instrument characteristics through the approximated expression [88]:

$$\sigma_\eta \propto \frac{\sigma}{\int B \times dl} \frac{1}{\sqrt{N+4}} \,. \tag{4.3}$$

From eq.4.3 it follows that the deflection uncertainty does not depend on the particle deflection[1]. The spectrometer resolution is limited by the spatial resolution (σ) and by the number of position measurements (N), which are both characteristics of the tracking system. Beside this, the deflection uncertainty depends on the magnetic field strength along the particle trajectory. For a given tracking system, the stronger is the magnetic field the greater is the track curvature, resulting in a greater sensibility to deflection variations and, as a consequence, in a better resolution.

The deflection uncertainty σ_η, together with χ^2_x and χ^2_y, enables to check the fitting result on an event-by-event basis, which is useful in order to select a sample of reliable tracks.

4.3.3 The spectrometer performances

Fig. 4.4 shows the distribution of the deflection uncertainty σ_η calculated event-by-event by the fitting routine, for a large sample of particles from flight data, with rigidity $R > 10$ GV. The considered sample contains positive singly charged particles with a well reconstructed track in the tracking system. As can be seen, the deflection uncertainty varies over a wide range of values, whose distribution reflects essentially the variations of the magnetic field inside the tracking volume.

The error on the measured rigidity R is related to the deflection uncertainty through

[1] This is strictly true only at high energy. At low energy a dependence on the deflection value is introduced by the multiple scattering effect. We will deal more in detail with this subject in chapter 6.

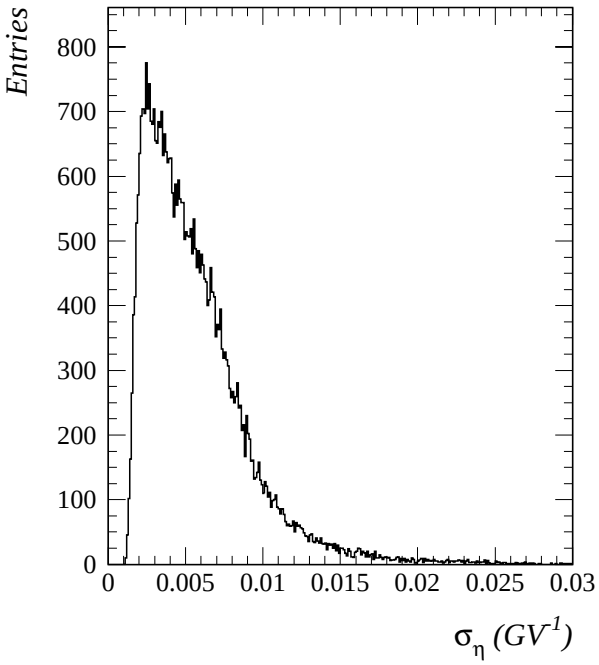

Figure 4.4: *Distribution of the deflection uncertainty, calculated event-by-event by the track fitting routine.*

the equation:

$$\frac{\delta R}{R} = \frac{\delta \eta}{\eta} = R\,\sigma_\eta\,. \tag{4.4}$$

From eq. 4.4 it follows that, assuming that σ_η does not depend on the deflection, the relative error on the rigidity increases linearly with rigidity. In order to characterize the spectrometer performance it is generally introduced the Maximum Detectable Rigidity (MDR), defined as the rigidity value at which the relative error is 100%. From eq. 4.4 it follows that the relation between MDR and σ_η is:

$$MDR = \frac{1}{\sigma_\eta}\,. \tag{4.5}$$

For the CAPRICE98 spectrometer, if we take the mean value of the distribution shown in fig. 4.4, a MDR of about 179 GV is obtained. Some authors define the MDR as the value corresponding to the maximum of the deflection uncertainty distribution: according to this definition we have $MDR \sim 400$ GV. Notice that the value of MDR obtained from the distribution of σ_η depends on the applied selection cuts.

The deflection uncertainty calculated in the fitting routine does not provide a complete information concerning the spectrometer response. Since the uncertainty on the

measured rigidity has a primary role in the deuterium measurement, an accurate knowledge of the spectrometer response is necessary. For this reason most of this work is dedicated to the parameterization of the spectrometer response (chapter 6).

4.4 The RICH detector

The CAPRICE98 apparatus was designed to perform particle identification in a wide energy range, with the specific aim of studying cosmic-ray antiprotons. The RICH detector was developed and built in order to fulfill this goal. It is composed of a gas radiator and a photosensitive MultiWire Proportional Chamber (MWPC) with pad read-out. The gas chosen as Cherenkov emitter was the one with the highest known refractive index. This configuration has allowed to mass resolve the (anti)proton from 18 GV, which is the (anti)proton Cherenkov threshold rigidity value, up to 50 GV, while below 18 GV it has acted as a threshold device [78].

The RICH detector has also a central role in the deuteron analysis, since the identification criterion is based on its response. Beside this, it is also involved in the parameterization of the spectrometer response. For this reason we dedicate to the RICH detector a large part of this chapter. In order to better understand the technical characteristics of the instrument, we begin this section with a concise review of the Cherenkov effect.

4.4.1 The Cherenkov effect

The Cherenkov effect is a consequence of the polarization of a medium traversed by a charged particle. Normally this does not produce any detectable effect at large distances from the particle trajectory. But, if the velocity of the particle is larger than the local phase velocity of light, an electromagnetic wave front is generated which can be detected far away from the trajectory.

Given a medium of refractive index n, the condition for Cherenkov light emission is

$$\beta > \frac{1}{n} \equiv \beta_{th} \, . \tag{4.6}$$

The light emission angle from the particle trajectory is fixed and depends on the particle

velocity through the relation:

$$\theta_c = \arccos(1/\beta n). \tag{4.7}$$

From eq. 4.7 it follows that the Cherenkov angle is zero for $\beta = \beta_{th}$ and increases with velocity toward an asymptotic value of $\theta_c{}^{max} = \arccos(1/n)$. Both the threshold velocity and the maximum angle depend only on the refractive index of the medium. The number of emitted Cherenkov photons per unit path length of a particle of charge Ze and per unit wavelength interval of the photons is given by [88]:

$$\frac{dN}{dxd\lambda} = \frac{2\pi Z^2\alpha}{\lambda^2}\left(1 - \frac{1}{\beta^2 n^2(\lambda)}\right) , \tag{4.8}$$

where α is the fine structure constant ($e^2/2\epsilon_\circ hc = 1/137.05$) and λ is the wavelength.

In a Cherenkov counter photons are converted in photoelectrons and detected. To obtain the number of detected photoelectrons (N_{pe}) eq. 4.8 must be integrated along the particle path length and over the wavelength interval where $\beta n(\lambda) > 1$, taking into account the detector efficiency. The resulting expression for N_{pe} is:

$$N_{pe} = L\ 2\pi Z^2\alpha \int_{\beta n(\lambda)>1} \epsilon_{coll}(\lambda)\epsilon_{det}(\lambda)\left(1 - \frac{1}{\beta^2 n^2(\lambda)}\right)\frac{1}{\lambda^2}\, d\lambda , \tag{4.9}$$

where L is the path length in the radiator, $\epsilon_{coll}(\lambda)$ is the efficiency for collecting the Cherenkov light and $\epsilon_{det}(\lambda)$ is the quantum efficiency of the transducer. In typical detectors the refractive index of the radiator is nearly constant over the useful range of the transducer sensitivity, so that eq. 4.9 reduces to:

$$N_{pe} \sim LN_\circ Z^2 sin^2\theta_c , \tag{4.10}$$

where

$$N_\circ = 2\pi\alpha \int_{\beta n(\lambda)>1} \epsilon_{coll}(\lambda)\epsilon_{det}(\lambda)\frac{1}{\lambda^2}\, d\lambda . \tag{4.11}$$

The quantity $N_\circ$ is often called *detector response parameter* (given in cm^{-1}) and characterize the properties of the whole detector.

The simplest Cherenkov counters take advantage of the existence of a velocity threshold for radiation. If the velocity of the particle is larger that the threshold velocity β_{th}, Cherenkov light is emitted and can be detected. If no Cherenkov light is detected this probably means that the particle velocity is lower than its threshold

value. This feature can be used to tag the particle enabling its identification. The overall identification capability is limited by Poisson fluctuations in the number of detected photoelectrons and by the δ-ray emission.

A more interesting feature of the Cherenkov light is the dependence of the Cherenkov angle on the particle velocity only. Detectors based on this property measure the Cherenkov angle, from which the particle velocity is determined. The combination of this information with, as an example, the measured momentum enables particle identification.

RICH detectors belong to the latter class. In this kind of detectors the Cherenkov light cone is generally focused on a projection plane by means of an optic system and the single photons detected by a position sensitive device. If the number of collected photons is high enough a ring-like image is formed from which the Cherenkov angle can be reconstructed.

Notations

The main features of the Cherenkov effect to which we will refer in the following can be expressed through the relation in eq. 4.12, obtained combining eq. 4.7 and 4.10.

$$\frac{N_{pe}}{N_{pe}^{max}} = \frac{sin^2\theta_c}{sin^2\theta_c{}^{max}} = 1 - \left(\frac{R_{th}}{R}\right)^2 . \tag{4.12}$$

From eq. 4.12 we have that the number of detected photoelectrons N_{pe} is directly proportional to the squared sine of the Cherenkov angle θ_c. Instead of expressing the energy dependence as a function of the velocity β, we have introduced the ratio R/R_{th}, where R_{th} is the Cherenkov threshold rigidity. In terms of this variable all the Cherenkov relations can be easily scaled to any particle by simply calculating the proper threshold rigidity R_{th}, which is given by:

$$R_{th} = \frac{Mc}{Ze}(\gamma\beta)_{th} , \tag{4.13}$$

where M is the particle mass.

4.4.2 The instrument

The CAPRICE98 RICH detector [91, 92, 93] is composed of a photosensitive MultiWire Proportional Chamber (MWPC), a gas radiator and a spherical mirror located at the

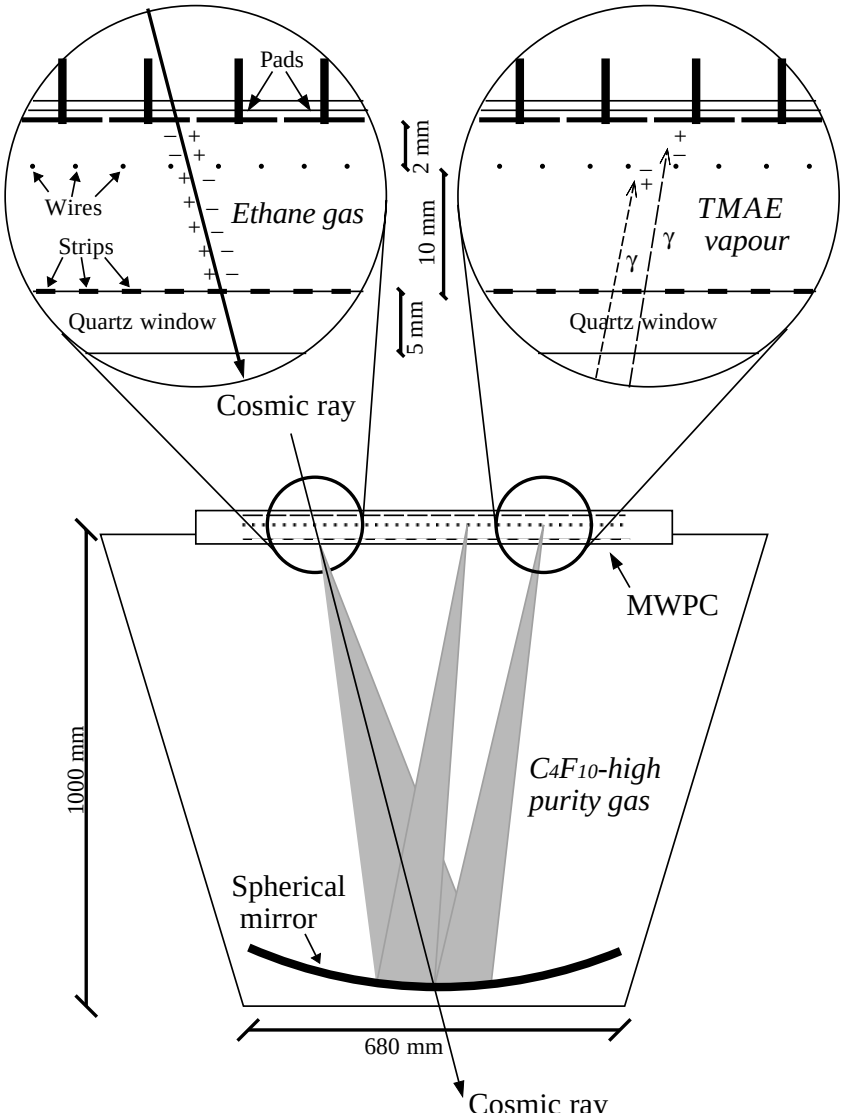

Figure 4.5: *A schematic view of the CAPRICE98 RICH detector. The upper expanded views illustrate how ionizing particles and photons are detected in the MWPC. See the text for a detailed description of the instrument.*

bottom of the radiator box. Fig. 4.5 shows a schematic view of the detector and illustrates its working concept. The picture shows a particle that enters the RICH detector traversing the MWPC, then crosses the radiator and, being its rigidity greater than the Cherenkov threshold rigidity, radiates creating a cone of light of half-angle θ_c. The emitted light is reflected back and focused by the spherical mirror toward the MWPC. The upper cathode plane of the MWPC is divided in pads, so that a ring-like image is detected.

The radiator

The radiator consists of an airtight aluminum box placed above the tracking system which upper plane holds the MWPC. The geometrical shape of the box was designed to cover the geometrical acceptance of the spectrometer and is about 1 m tall.

The radiator volume is filled with perfluorobutane (C_4F_{10}), also known as decafluorobutane, which was chosen as Cherenkov light emitter because is the gas with the highest known refractive index at room temperature. During the balloon flight the measured mean value of the refractive index [92, 93] was $n_{C_4F_{10}} \sim 1.001401$, from which we have

$$(\beta\gamma)_{th} \sim 18.88 \, . \tag{4.14}$$

The radiator box was equipped with a gas system which main purpose was to separate and clean the C_4F_{10} gas from all other gas and especially from oxygen. This is particularly important since oxygen can absorb Cherenkov photons reducing the overall efficiency of the detector.

The MWPC

The MWPC is composed by a frame with 128 anode wires placed between an upper cathode plane with 4096 pads (each 8×8 mm^2 wide) and a lower cathode of 160 conductive strips evaporated on a quartz window (see fig. 4.5). Both the anode wire plane and the pad plane are connected with the read-out electronics. The active area is 480×480 mm^2, which corresponds to the quartz window dimensions.

The MWPC is operated with pure ethane saturated with tetrakis-(dimethyl-amino)-ethylene (TMAE) gas. The former acts as the sensitive gas while the latter acts as photon converter. When a particle crosses the MWPC it ionizes the ethane gas. The

produced electrons drift toward the anode wire, where an avalanche multiplication occurs and a signal is induced. If Cherenkov photons are produced, they enter the MWPC through the 5 mm thick quartz window and are converted into detectable photoelectrons by the TMAE. Since the upper cathode plane has a two-dimensional segmentation, both the impact position of the particle and the Cherenkov ring are detected.

The detector response parameter

The quartz window is transparent for wavelengths longer than $\sim$ 170 nm, while the quantum efficiency of the TMAE drops to zero at $\sim$ 220 nm. These two factors define the RICH detector photon sensitivity region. From eq. 4.8 we estimate that a charge one particle with $\beta \sim 1$ traveling over a distance of 1 m in a gas radiator with the measured mean refractive index would produce ~ 172 photons. The resulting number of detected photoelectrons is determined by the reflectivity of the mirror, the quantum efficiency of the TMAE, the transmission factor of all the traversed materials and the detection efficiency of the MWPC after the pedestal subtraction. By integrating all these factors over the sensitivity region we obtain a rough estimate of the number of detected photoelectron of about 14 [93]. The resulting response parameter of the CAPRICE98 RICH detector is $N_\circ \sim 50$ cm^{-1}.

4.4.3 The Cherenkov angle reconstruction algorithm

The signal induced in the MWPC has different characteristics if due to photoelectrons, ionizing particles or noise. Each photoelectron that reaches the MWPC gives a signal that spreads over $3-5$ pads. For an event where Cherenkov light has been emitted, several photoelectrons are collected, which are distributed along a circle. Since the number of detected photoelectrons is generally large, there is a high probability that one pad would collect charge induced by two or more photoelectrons. A typical Cherenkov event is thus characterized by the presence of a ring-like image in the pad plane, resulting from the merging of the signals induced by each photoelectron. If the particle crosses the MWPC, beside the Cherenkov ring, a ionization cluster is detected, which total signal is about ten time larger than the signal induced by a photoelectron. The noise results instead in random hits, which does not have any significant structure.

For each event, the particle track is reconstructed up to the MWPC level. This is

done by using the information given by the spectrometer. If the track intersects the MWPC, the pads laying inside the 9×7 area surrounding the intersection point are excluded from the Cherenkov angle calculation[2]. For each one of the remaining hit pads, the Cherenkov angle (θ_i) is calculated by minimizing the path traveled by the light between the emission point and the position of the pad ([92, 93]). The position of the emission point along the trajectory is not essential, since parallel light rays are focused by the spherical mirror towards a single point in the focal plane, so that, for simplicity, it is assumed to be at half-way between the MWPC and the mirror.

The Cherenkov angle of the whole event is calculated using the *Gaussian potential method* [94]. It has been shown in a previous work on CAPRICE94 [96] that this method gives the best results in the Cherenkov angle determination. According to this method a weight ω_i is assigned to each pad following a Gaussian distribution around the Cherenkov angle θ_c of the event:

$$\omega_i = exp\left[\frac{-(\theta_i - \theta_c)^2}{2\sigma_i^2}\right] , \tag{4.15}$$

where σ_i is the single pad Cherenkov angle resolution. For the calculation a fixed value of $\sigma_i = 7.8$ mrad was used, which is the measured value obtained from flight data [92]. The value of θ_c is then obtained minimizing the function

$$f(\theta_c) = -\sum_{n_{pad}} \omega_i , \tag{4.16}$$

where the summation is performed over all the pads. Those pads with a Cherenkov angle θ_i far from the expected value are rejected.

A useful quantity provided by the reconstruction routine is

$$N_{eff} = \frac{(\sum_{n_{pad}} \omega_i)^2}{\sum_{n_{pad}} \omega_i^2} . \tag{4.17}$$

In the ideal case of Gaussian distributed θ_i, the expectation value of the above quantity is exactly n_{pad}. In the real case there are some spurious pad hits, due to e.g. electronic noise or δ-rays. Since these pads have generally a small weight, N_{eff} can be regarded as the *effective number of pads* used in the Cherenkov angle calculation. This number is closely related to the number of pad hits due to Cherenkov light and therefore to the number of detected photoelectrons.

[2]The excluded area is not squared because the spatial resolution of the MWPC is not the same in the x and y directions. This is due to the presence of the wires, which affect the signal collection in the x direction resulting in a worse spatial resolution.

4.4.4 The particle identification capability

As previously mentioned, the RICH detector provides the basic criterion for the deuteron identification. In this subsection the general RICH detector identification capabilities are discussed and its role in the deuteron selection specified.

Particle signatures

For a better understanding of the RICH detector performances it is useful to study the particle signature in a graphical view. We discuss separately the particle signature in the RICH detector, in order to highlight some basic features directly involved in the deuterium measurement. At the end of this chapter (section 4.6) we will also show the particle signature in the whole apparatus.

Fig. 4.6 shows the reconstructed signal of the RICH detector for different type of events. Since the RICH MWPC does not cover the whole acceptance of the tracking system, only a fraction of the events with a contained Cherenkov ring have the particle trajectory crossing the detector. In fig. 4.6 only events belonging to this category are shown, in order to better discuss the most important RICH detector features.

In fig. 4.6 each square correspond to one pad hit. The filled squares are those pads used in the Cherenkov angle reconstruction. The circles refer to information coming from the RICH data: the small circle is located at the position where the particle crossed the MWPC, the big one is derived from the reconstructed Cherenkov angle. The former information is obtained by means of a center of gravity calculation. Since a charged particle that crosses the MWPC induces a signal that is typically ten times larger than a signal induced by a photoelectron, the ionization area is unequivocally identifiable as the area surrounding the pad with the maximum signal. The other symbols represent information coming from the tracking system: the $\times$ indicates the extrapolated particle coordinates, the $+$ is the expected center of the circle and the $\nearrow$ shows the direction of the incident particle.

In fig. 4.6 we can observe, for some typical events, the clean appearance of the Cherenkov ring, if present, and of the ionization signal. Notice how spurious pad hits are suppressed by the Gaussian potential method, which makes use of the tracking system information about where in the pad plane the Cherenkov light should have been detected. It acts both when the Cherenkov is reconstructed and when no Cherenkov

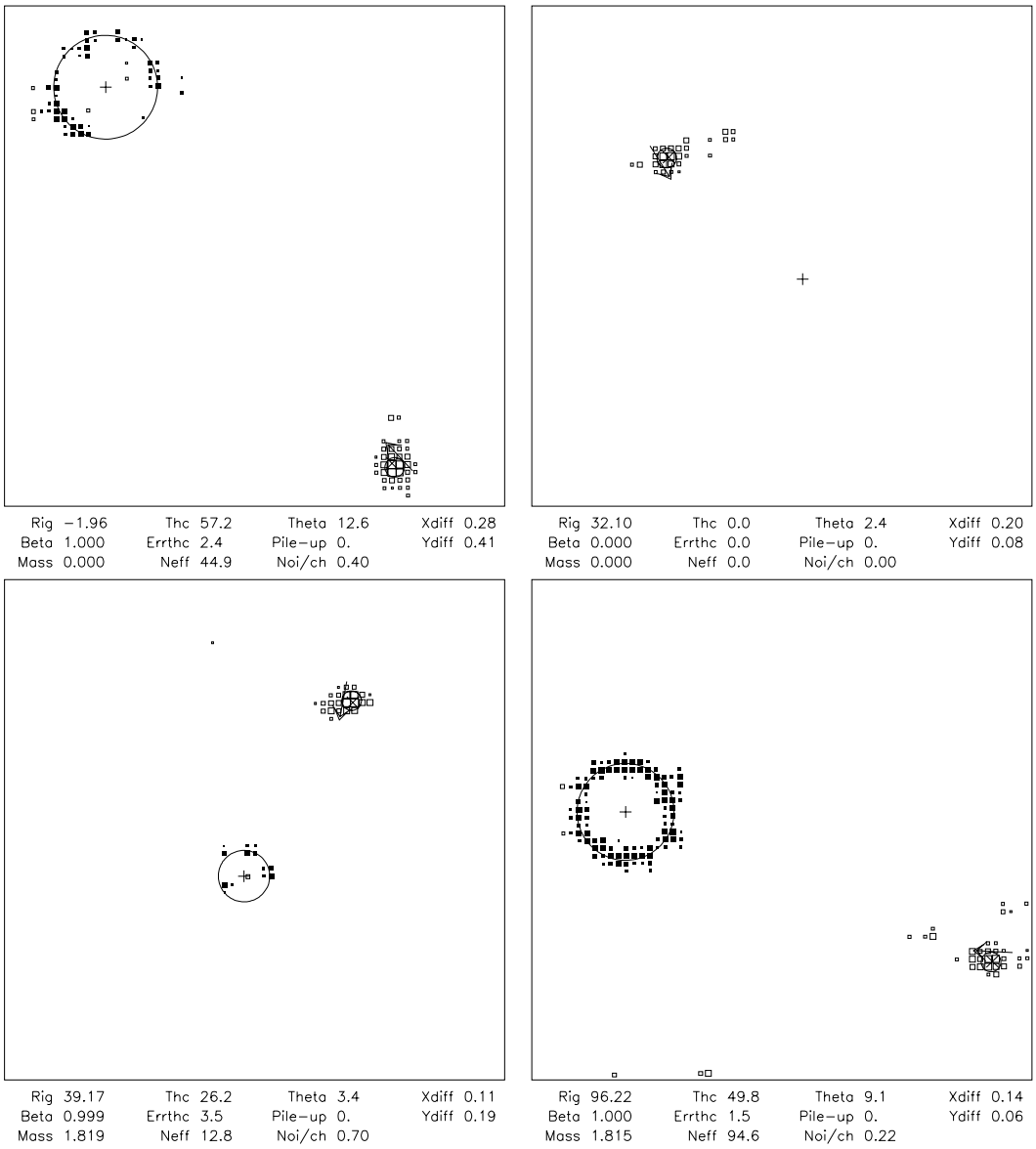

Figure 4.6: *The signature in the RICH detector pad plane from particles of different kind. Upper left plot: electron of measured rigidity* ~ 2 *GV, . Upper right and lower left plots: protons or deuterons of measured rigidity* ~ 32 *GV and* ~ 39 *GV respectively. Lower right plot: helium nucleus of measured rigidity* ~ 96 *GV. See the text for the symbol explanation.*

signal is detected.

The upper right plot in fig. 4.6 shows an event with $N_{eff} = 0$. Even if there are some pad hits outside the ionization area, probably due to δ-ray emission, they are rejected, being far from the region where the Cherenkov signal is expected. Notice also the low number of noise induced hits, which are anyway efficiently rejected by the algorithm. This is important when the RICH is used as a threshold device. In this cases the particle is identified by requiring no Cherenkov signal, if the measured rigidity is below the particle threshold for Cherenkov light emission. A large number of spurious hits would affect the selection efficiency.

The upper left plot in fig. 4.6 shows a relativistic electron and therefore both the Cherenkov angle and the number of detected photoelectrons are at their maximum. For the event shown in the lower left plot of fig. 4.6 the Cherenkov angle and the number of detected photoelectrons are instead significantly smaller than their maximum value. Nevertheless, even in this case the Cherenkov angle is well reconstructed. The lower right plot shows a helium nucleus. In this case we have to notice the much larger amount of detected Cherenkov light (see eq. 4.10).

Particle identification

Fig. 4.7 shows the reconstructed Cherenkov angle for a sample of singly charged particles selected from flight data. The curves superimposed to the plot represent the theoretical expected values for different particles. We can notice that particles of different type distribute around the theoretical curves.

For what concerns the deuterium selection, the most difficult task is to separate it from the most abundant protons. To this aim the RICH detector can, in principle, both act as a threshold device and can be used to mass resolve particles by means of a measured Cherenkov angle versus rigidity selection. The solid curves in fig. 4.7 show the theoretical expected Cherenkov angle as a function of the rigidity, for both protons and deuterons. The protons start to emit Cherenkov light at $\sim$ 18 GV, while the deuteron Cherenkov threshold rigidity is $\sim$ 35 GV. This provide a first identification criterion, since, between the two threshold rigidities, protons have a Cherenkov signal while deuterons have not. We will see, partly in chapter 5 and definitively in chapter 6, that this is not exactly true and the deuterium can actually be identified in the interval $\sim 30 - 45$ GV, due to both the spectrometer resolution and the rigidity dependent

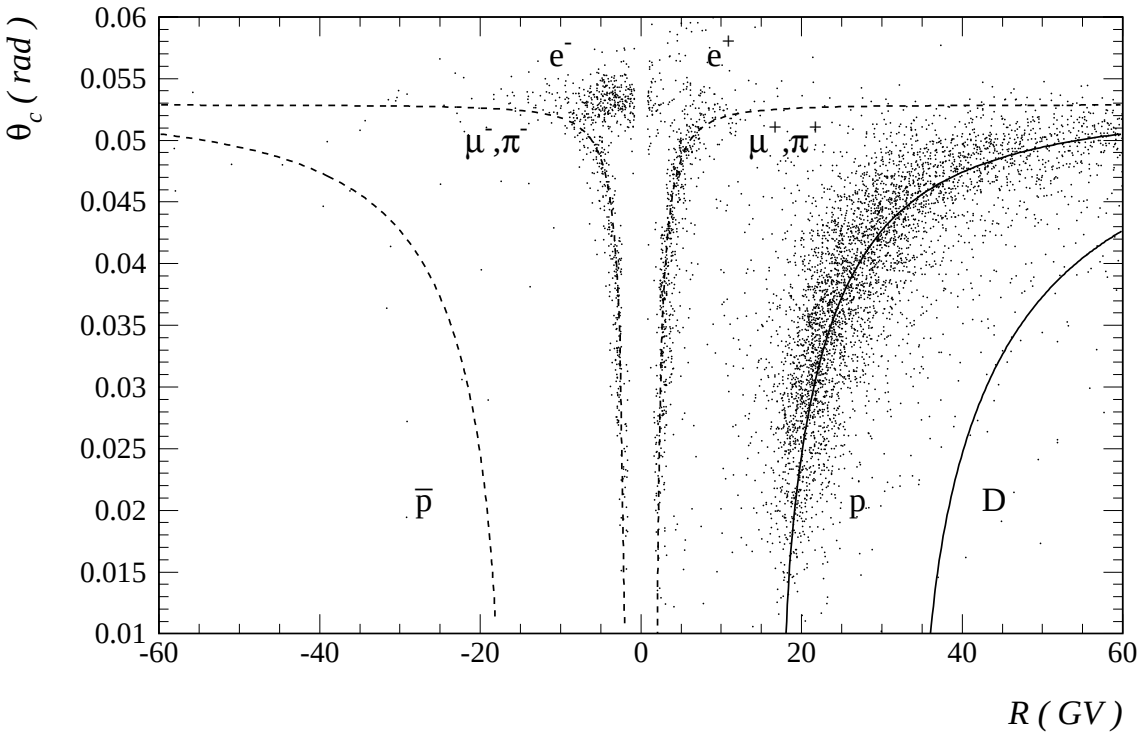

Figure 4.7: *The measured Cherenkov angle as a function of the rigidity for a flight sample of singly charged particles. Negative values of the rigidity refers to negatively charged particles. The curves represents the theoretical expected values for particles of different kind.*

probability for Cherenkov light emission.

When both protons and deuterons emit Cherenkov light, the Cherenkov angle can be reconstructed, and the result is shown in fig. 4.7. Experimental points are distributed around the theoretical curves with a spread which width is due to both the Cherenkov angle resolution and the rigidity resolution. This latter effect increases for increasing rigidity, according to eq. 4.4, and has a visible crucial role for deuterons and protons. Due to the difference, for a given rigidity value, between the measured Cherenkov angles, deuterons and protons can be in principle separated, starting from the deuteron Cherenkov threshold rigidity up to where the two curves are still distinguishable. Actually, the small number of detected photoelectrons near the threshold and the rigidity uncertainty reduce considerably this interval and make this analysis

quite complex. As a consequence we did not use this information.

4.5 The calorimeter

The CAPRICE98 silicon-tungsten calorimeter [89, 90] was the same one used during the 1994 CAPRICE flight.

The calorimeter role is antiproton (positron) detection out of the large electron (proton) background. This task requires a high identification capability of electromagnetic showers, which led to the choice of a tungsten absorber. The advantage of using a high-Z absorber material is that it minimizes the radiation length ($X_\circ \propto A/Z^2$ [95]), thus maximizing the electromagnetic shower development, against the nuclear interaction length ($\lambda_\circ \propto A^{1/3}$ [95]). The design of instruments qualified for balloon flight is subjected to severe constraints on weight and mechanical stability. This imposes restrictions in the calorimeter depth, which determines the shower containment. The study of several prototypes previously developed has shown that the limitations coming from an insufficient shower containment can be compensated by a high granularity and energy resolution. This led to the choice of strip silicon sensors as active layers.

4.5.1 The instrument

The instrument is composed of 8 silicon sensor planes interleaved with 7 layers of tungsten absorber, 1 $X_\circ$ deep each. The total depth is 7.2 $X_\circ$ and 0.33 $\lambda_\circ$. Each sensor layer is a matrix of 8×8 silicon modules having an active area of 6×6 cm^2. A single module is composed by two silicon sensors, 380 μm thick, divided in 16 strips, 3.6 mm wide. The silicon sensors are mounted back-to-back with perpendicular strips to provide double coordinates read-out in the xy plane. The strips of each silicon sensor are daisy-chained longitudinally to form one single strip 48 cm long.

4.5.2 The calorimeter performances

The CAPRICE calorimeter performances have been extensively studied by means of simulations and experimental data. The simulation program is a Monte Carlo code based on the GEANT library version 3.21, which was developed for the 1994 flight, and the results of that study were presented in references [95, 96].

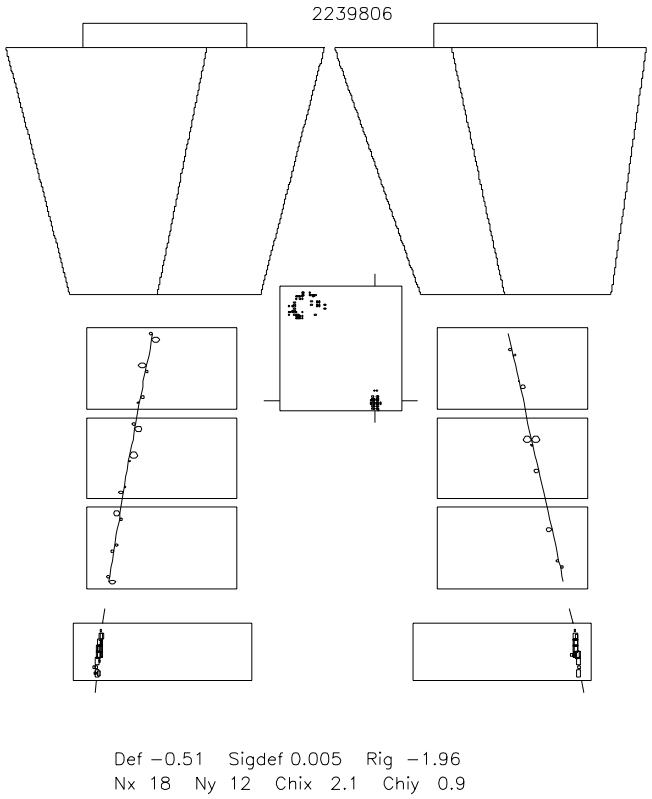

Figure 4.8: *Graphic view of the event, for an electron of measured rigidity* ~ 2 *GV. Notice the path in the calorimeter, which is typical of an electromagnetic shower.*

The high segmentation of the silicon-tungsten calorimeter, both in the longitudinal and transverse directions, combined with the energy loss in each silicon strip offers several selection criteria to perform particle identification. These features allow a good identification of electromagnetic showers against non-interacting particles and interacting hadrons. This was of primary importance in the antiproton analysis, where the estimated electron contamination was $(0.6 \pm 0.2)\%$ [78, 79].

The calorimeter has only a marginal role in the present analysis. We have used it to select muons from ground data, which have been used to study the RICH detector response (section 6.2). This has been done by requiring non interacting paths in the calorimeter. The calorimeter is also involved in the study of the detector efficiencies (section 5.2). It has instead no role in the deuteron selection.

4.6 Particle signature in the CAPRICE98 apparatus

We conclude the description of the CAPRICE98 telescope by showing some typical events in a graphic view (fig. 4.9-4.10), as was done in section 4.4.4 for the RICH

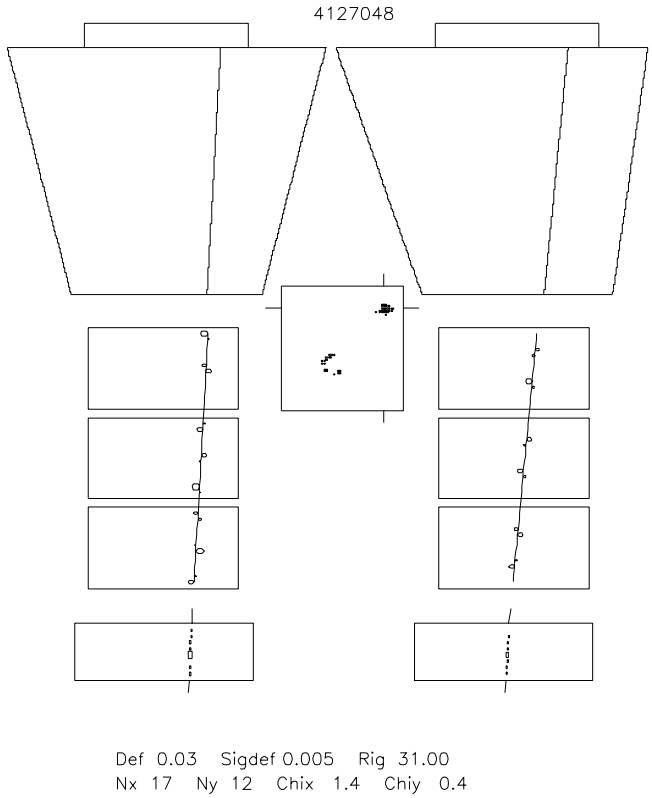

Figure 4.9: *Graphic view of the event, for (most probably) a proton of measured rigidity* ~ 31 *GV. Notice the path in the calorimeter, which is typical of a non-interacting particle.*

detector. This is useful to visualize the geometry of the apparatus as a whole and exemplify its identification power.

In each picture is shown the projection of the event on both the bending (left plot) and non-bending (right plot) view (compare with fig. 4.1 to identify each detector). The box in the middle represents the RICH detector pad plane, for which has been used the same representation of fig. 4.6 reduced. The continuous curves crossing both the views of the apparatus represent the two projections of the reconstructed track, extrapolated up to the RICH MWPC. The signal in the drift chamber is represented by small circles, which correspond to the wire hits. The radius of the circles represent the distance between the particle track and the wire, which is in the center, determined from the measured drift-time. The signal in the calorimeter is represented by small boxes which position corresponds to the position of the each hit strip. The size of each box is proportional to the collected charge.

Fig. 4.8 show a negative particle of measured rigidity ~ 2 GV. In the pad plane the ionization cluster, where the track intersect the RICH MWPC, and the Cherenkov ring are clearly visible . We have to notice the particle signature in the calorimeter,

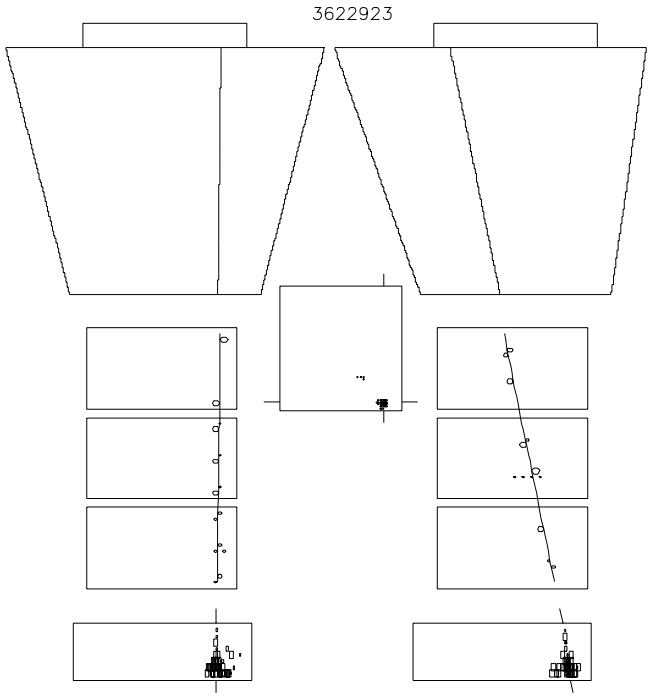

Figure 4.10: *Graphic view of the event, for (most probably) a deuteron of measured rigidity* $\sim$ *35 GV. Notice the path in the calorimeter, which is typical of a hadronic shower.*

characterized by a narrow shower collimated in the direction of the incident particle. This is the typical appearance of an electromagnetic shower, so that the particle is unambiguously identified as an electron. Fig. 4.9 shows a $Z = 1$ particle whose measured rigidity is $\sim$ 31 GV. Even in this case there is a Cherenkov signal detected. From the discussion of section 4.4.4 it follows that the recorded particle is most probably a proton. We have to notice in this case the non-interacting path in the calorimeter, which is generally characterized by only one strip hit for each plane. Finally, fig. 4.10 shows a $Z = 1$ particle with measured rigidity $\sim$ 35 GV. In this case no Cherenkov signal has been detected, so that only the ionization cluster in the MWPC is visible. From section 4.4.4 it follows that the particle is most probably a deuteron. We have to notice the particle signature in the calorimeter, which is typical of hadronic showers. In this case the shower has a much larger lateral spread than an electromagnetic one.

4.7 The live time

In order to obtain flux result it is necessary to know the live time (T_{live}) of the experiment. To this purpose the payload was equipped with two scalers. One was counting

during all the effective exposure time, when all the detectors were active. The other was counting only when the acquisition system was not busy, that is when the apparatus was able to accept a trigger from a particle event. The ratio between the two numbers gives the fractional live time, which during the CAPRICE98 flight was $(48.65 \pm 0.02)\%$. Events were collected at float during a period of about 21.1 hours, resulting in a live time of:

$$T_{live} = 32712 \pm 27 \text{ s} \tag{4.18}$$

Chapter 5

Selection of protons and deuterons

In order to obtain a reliable response from the instrument, the recorded event sample must be cleaned. This has been done by applying proper selection cuts on several variables, which allow to select $Z = 1$ particles with a well reconstructed track in the tracking system and a trajectory contained in the sensitive volume of the detectors. The deuterons have then been selected among the surviving particle sample.

Sections 5.1 and 5.2 are dedicated to the description of all the basic cuts together with their selection efficiencies. This is an essential information in order to give flux results. Finally, in section 5.4 we describe the deuterium selection, which is based on the information given by the RICH detector, used as a threshold device.

5.1 Basic selection criteria

The particle identification with the CAPRICE98 apparatus is based on the measurement of the rigidity R and the charge Z, to which some further specific selection criteria must be added. In the present work the deuterium has been selected, among positive singly charged particles, by means of the RICH detector used as a threshold device. In order to assure the reliable reconstruction of each event some basic conditions must be imposed on data. First of all geometrical constraints are necessary, to ensure the containment of the selected events inside the sensitive volume of those detectors involved in the particle identification. Of primary importance is also to check the track fitting result, in order to ensure a good measurement of the particle rigidity. As will be shown in chapter 6 the spectrometer resolution sets strong constraints on the rigidity interval over which the deuteron is identifiable out of the large proton background. Last but not least is the necessity of rejecting those events where the particle interacted in the

payload material above the spectrometer, which are characterized by multiple tracks.

The present section is dedicated to the description of all the basic criteria for the selection of $Z = 1$ particles with a well reconstructed path in the apparatus and a reliable measurement of the rigidity R. The applied cuts are enumerated in tab. 5.1 and are discussed in the following. The deuterium has been selected out of the resulting particle sample as described afterwards, in section 5.4.

Table 5.1: *Basic criteria applied to select $Z = 1$ downward-going particles with a well reconstructed track in the spectrometer.*

	TOF selection
1	no upward-going particles ($\beta > 0$)
2	only one pad hit in the top scintillator plane
3	$dE/dx < 1.8$ *mip* in the top scintillator plane
	Tracking system selection
4	$\eta > 0$
5	$N_x \geq 11$ and $N_y \geq 7$
6	$\chi^2_x < 4$ and $\chi^2_y < 8$
7	$\sigma_\eta < 0.008$ GV^{-1}
8	containment of the track in the tracking volume ($0 < x_{fit}, y_{fit} < 41.9$ cm)
	RICH detector selection
9	no saturated pads outside the ionization area
10	if the track intersect the pad plane, consistency between the extrapolated trajectory in the MWPC and the center of gravity position of the ionization cluster
11	rejection of tracks going through the support frame of the RICH detector
12	containment of the center of the expected Cherenkov ring inside the pad plane, excluding an outer frame of ~ 5 cm

5.1.1 The TOF selection

The scintillator system provides two sets of information: a measurement of the particle time-of-light and the energy loss by ionization in the top and bottom scintillators.

The time-of-light measurement has been used to reject albedo (upward-going) particles. This has been done by requiring that the measured velocity was $\beta > 0$ (cut 1). The TOF system resolution assures that no albedo contamination remains in the sample.

The scintillator amplitude signal has been instead used to both identify multiparticle events and to perform charge selection. The segmentation of the scintillators enables to partly reject multiparticle events by requiring only one pad hit on the top scintillator (cut 2). Above 10 GV both deuterons and protons are minimum ionizing particles (*mip*), so that the charge selection has been done by simply requiring that the energy loss in the top scintilaltor was $dE/dx < 1.8\ mip$ (cut 3). The estimated residual contamination of helium nuclei is $\sim 0.2\%$. As shown in reference [95], this cut maximizes the statistic while leaving a negligible contamination of double tracks, which signal in the top scintillator have a peak at $\sim 2\ mip$. The bottom scintillator has not been used in the charge selection since it could collect signals from backscattered particles produced in the calorimeter if an hadronic interaction occurred. This would led to the rejection of good proton or deuteron events which interacted in the calorimeter.

5.1.2 The tracking system selection

After the TOF charge selection (cut 3) the sample contains both positive and negative singly charged particles. The negative charge component has been excluded by requiring a positive deflection (cut 4).

A reliable measurement of the particle rigidity is of main importance for the deuteron analysis. Therefore, strict selection constraints on the quality of the fitted tracks have been applied. The tracking selection criteria have been extensively studied in previous works related to the same experiment. The criteria applied here are based on the gained experience. A minimum number of position measurements on both the bending and non-bending view has been required (cut 5). The uncertainty on the measured deflection depends in fact on the number of points used in the track fitting (see eq. 4.3). The quality of the fitted track is characterized by the resulting reduced χ^2. As a consequence, constraints on this quantity have been applied in order to select well reconstructed tracks (cut 6). To all the above conditions a constraint on the deflection uncertainty, estimated analytically by the fitting routine for each event, has been added (cut 7). From what discussed in section 4.3.2 it follows that an effect of this cut is the rejection of those particles that traversed the tracking volume in low magnetic field regions. For these particles the deflection measurement is intrinsically less accurate.

Since the field of view of the TOF system is larger than that of the spectrometer, not

all the triggered particles had a track contained inside the tracking volume. Therefore, some geometrical constraints have been applied by requiring that the fitted track was contained in the spectrometer (cut 8).

5.1.3 The RICH detector selection

Beside a criterion for the deuteron identification against the bulk of protons, the RICH detector provides other useful information. The RICH MWPC is in fact a tracking detector and its information can be used to efficiently reject multiparticle events. A ionizing particle induces a signal on the MWPC that is high enough so that at least one pad signal, in the ionization cluster, generally saturates the electronics. This provide a criterion to identify multiparticle events, which are rejected by requiring no saturated pads outside the ionization area (cut 9). For those tracks traversing the MWPC, we have also required that the center-of-gravity of the ionization cluster was consistent with the intersection point position (cut 10).

The deuteron identification is based on the RICH detector information. It is thus necessary that if the particle emitted Cherenkov light it could be detected, that means that the possible Cherenkov ring must be contained in the pad plane. This has been assured by requiring that the center of the Cherenkov ring, inferred by using the tracking information (see section 4.4.3), was contained inside an inner perimeter in the pad plane (cut 11). The thickness of the excluded frame is ~ 5 cm, which corresponds to about the radius of the maximum Cherenkov ring.

An additional geometrical constraint has been applied, in order to exclude those particle traversing the support frame of the RICH detector. This frame is about 53 mm thick, corresponding to almost one half of the interaction length. Since its thickness is much larger than the total thickness of the whole materials above the spectrometer, we have decided to exclude it, by requiring that the fitted track did not intersect it (cut 12).

5.2 Selection efficiencies

In order to give flux results it is necessary to know the selection efficiencies, that is the probability for a particle of a given type to pass the selection criteria of each detector. The general procedure to estimate the efficiencies is to take a sample of

Table 5.2: *The detector selection efficiencies and the geometrical factor for the basic selection criteria. In column 2 are summarized the conditions, listed in tab. 5.1, to which the corresponding efficiency refers. All the geometrical conditions have been included in the geometrical factor GF.*

Condition	Applied cuts	Result
Selection efficiency		
TOF	1 2 3	$\epsilon_{TOF} = 0.9122 \pm 0.0043$
Tracking system	4 5 6 7	$\epsilon_{Trk} = 0.7739 \pm 0.0086 + 0.0145$
RICH detector	9 10	$\epsilon_{RICH} = 0.8851 \pm 0.0077$
Geometrical factor		
Geometry	8 11 12	$GF = 133.2$ cm^2 sr

particles of a given type and to apply the selection cuts for the detector under study. The fraction of surviving events gives the efficiency of the detector. There are several methods to obtain efficiency samples: with simulations, with beam tests or through the analysis of flight data. As partly discussed in section 4.1.2, the general approach for the CAPRICE98 analysis has been to study the efficiencies by using directly flight data, which is possible thanks to the redundancy of information provided by the several detectors. The efficiency samples have been obtained by selecting samples of particles, as cleaner as possible, by using the information of all the detectors but that one under study. This method has the advantage that the obtained results can be immediately applied to flight data, while this is not so straightforward for the other two methods. The procedure has anyway a drawback, since wrong assumptions or correlations among selection cuts may bias the sample. As a consequence, the analysis requires extreme caution and a good knowledge of the detectors.

The procedures to estimate the efficiency of the CAPRICE98 detectors have been developed for the previous antiproton analysis [79] and are partly based on the experience gained during the analysis of data from similar experiments. The same procedures have been applied, modified here to take into account the different selection parameters, in order to estimate the detector efficiencies for protons in the rigidity range $20 - 50$ GV[1]. The cuts 8 and 11-12 express only geometrical conditions. Therefore, their effect has been included in the geometrical factor calculation, described in section 5.3. Given the geometrical constraints, the effect of all the other cuts has been

[1]We have assumed that the selection efficiencies for the basic cuts was the same for protons and deuterons.

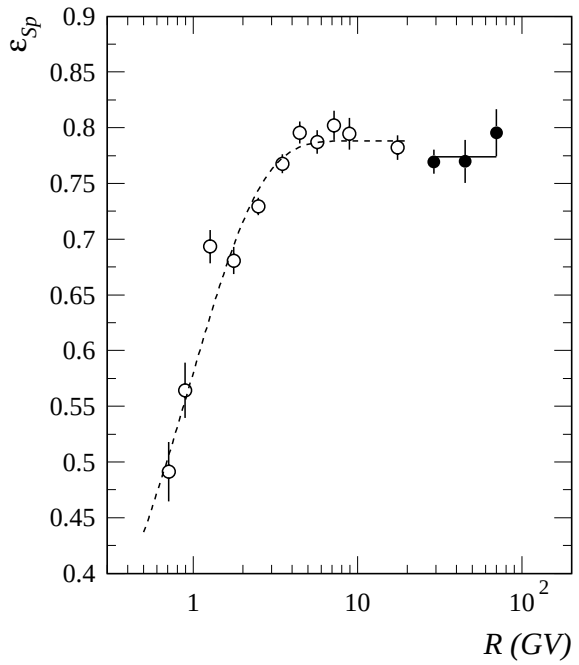

Figure 5.1: *The tracking system selection efficiency. Filled circles: result from the RICH method. Open circles: result from the no-DC method. (see the text for explanations). Solid and dashed lines: fits to the data.*

included in the efficiency of each detector and estimated as briefly described in the following. The results are summarized in tab. 5.2. For more details see reference [79] and references therein.

The TOF efficiency

The efficiency of the TOF selection (cuts 1-3) has been estimated using a sample of particles selected by applying all the basic tracking and RICH conditions (cuts 5-7 and 9-10) and the additional requirement that the signal in the first two layers of the calorimeter was less than 3 *mip*, in order to reject helium and heavier nuclei. The TOF efficiency (ϵ_{TOF}) has been found to be constant in the rigidity range $20 - 50$ GV, and its average value is shown in tab. 5.2.

The tracking system efficiency

In order to estimate the tracking system selection efficiency, an independent measurement of the particle rigidity is necessary. This information can be obtained with two different methods: the *RICH method* and the *no-DC method* [79].

The RICH method uses the rigidity value derived from the reconstructed Cherenkov angle. The efficiency sample has been selected by applying both the TOF and the

RICH detector basic conditions (cuts 1-3 and 9-10) and the additional requirements of a well reconstructed Cherenkov ring and a non-interacting path in the calorimeter. The Cherenkov angle has been calculated by applying the algorithm described in section 4.4.3, modified in order to use an extrapolation of the track in the calorimeter, instead that in the spectrometer. The reconstructed track in the calorimeter has also been used to ensure the basic geometrical conditions (cuts 8 and 11-12). For each measured Cherenkov angle, the rigidity has been obtained by assuming a mass of a proton. To the selected sample the basic tracking cuts 4-7 have then been applied, and the surviving fraction of events is shown in fig. 5.1 by filled circles. This method provides an estimate of the efficiency only above the proton rigidity threshold for Cherenkov light emission $R_{th} \sim 18$ GV. The solid line in fig. 5.1 is a straight-line fit to the data, which result is 0.7739 ± 0.0086.

The no-DC method is based on the same track fitting routine used for the tracking system, described in section 4.3.2, modified in order to use the position measurements given by all the tracking detectors but the drift chambers. The tracking planes used for the calculation are the RICH MWPC, the top scintillator and at least five calorimeter layers in each view. The efficiency sample has been selected by applying both the TOF and the RICH detector basic conditions (cuts 1-3 and 9-10) and by adding the requirement of no Cherenkov signal detected. Among the resulting particle sample, protons have been selected by using the TOF β measurement. The resulting selection efficiency for the tracking cuts 4-7 are shown in fig. 5.1 by open circles. The no-DC method allows to check the tracking system efficiency only in the low rigidity range, due to limitations in the achievable MDR.

The dashed line represents a fit to the data. It can be seen that the efficiency increases for increasing rigidity up to a constant value of 0.7884 ± 0.0057 above ~ 7 GV.

We have taken the value given by the RICH method as the best estimate of the tracking selection efficiency (ϵ_{Trk}). The difference between this value and that one obtained from the no-DC method has been considered as a systematic uncertainty, which is expressed by the one-sided error on ϵ_{Trk} presented in tab. 5.2.

Events with backscattering into the tracking system were investigated for the CAPRICE94 and no evidence was found that they would affect the efficiency of the tracking system [60].

The RICH efficiency

The proton sample for the RICH detector selection efficiency study has been selected by applying both the TOF and the tracking system basic conditions (cuts 1-3 and 4-7) and by adding some calorimeter requirements to select interacting hadrons. The RICH detector conditions 9-10 have then been applied to the selected particle sample, resulting in the efficiency value (ϵ_{RICH}) presented in tab. 5.2.

5.3 Geometrical factor

The geometrical factor for a particle telescope is defined as the proportionality constant $GF = C/J$ that relates the measured counting rate C to an isotropic flux intensity J, and it is determined by the geometry of the detector and by any applied geometrical constraints. The GF for the CAPRICE98 apparatus, with the geometrical conditions 8 and 11-12, has been evaluated with simulation techniques [97]. A reduced version of the CAPRICE98 simulation code, which takes into account only the geometry of the apparatus, has been used. Due to the presence of the magnetic field, which bends the particle tracks, the GF is in general rigidity dependent, but approaches a constant value for rigidity values above ~ 1 GV, when the particle track is nearly straight. The high rigidity value of GF is presented in tab. 5.2.

5.4 The deuteron identification

The task of the conditions listed in tab. 5.1 is the selection of $Z = 1$ particles with a well reconstructed track. The open circles in fig. 5.2 show the rigidity distribution of the events surviving all the basic cuts. This sample contains both protons and deuterons.

In order to identify the deuterons among the most abundant protons, the RICH detector has been used as a threshold device (see section 4.1.2). Protons emit Cherenkov light for rigidities above $R_{th} \sim 18$ GV, while deuterons start to emit at $R_{th} \sim 35$ GV. Therefore, deuterons can be identified, above the proton threshold rigidity, by requiring no Cherenkov signal detected. Fig. 5.2 shows the distribution (filled circles) of the events, selected by applying the above condition, as a function of the rigidity. The dashed lines indicate the position of the Cherenkov threshold rigidities for both protons and deuterons. As expected, the number of selected events drops above

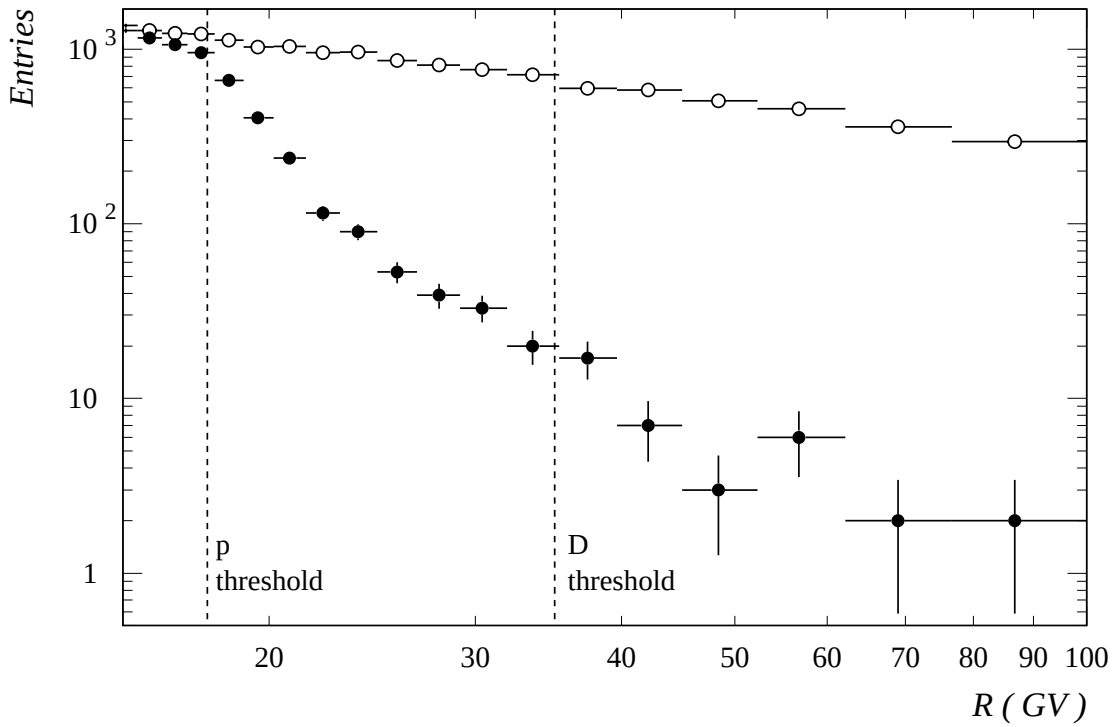

Figure 5.2: *Distributions of the selected events as a function of the measured rigidity. Filled circles: events without a Cherenkov signal. Open circles: all selected events. Dashed lines: proton and deuteron Cherenkov threshold rigidities.*

the proton Cherenkov threshold rigidity, where the protons start to emit Cherenkov light. For increasing rigidities, the distribution flattens while approaching the deuteron Cherenkov threshold rigidity and drops again above it. The rigidity region where the distribution flattens indicates the range where the deuteron component outnumbers the proton background. The proton contamination level is however significant over the whole rigidity interval, so that, in order to obtain the deuteron component, it must be estimated and subtracted.

Unlike the basic selection criteria, the deuteron selection criterion cannot be cross-checked by using the others devices, since the RICH detector is the only one whose information can be used to identify the deuterons. Therefore, a simulation has been used. This is the subject of the following chapter, where we will describe the instrument response model developed to estimate both the proton contamination and the deuteron

selection efficiency.

Chapter 6

Proton contamination and deuteron selection efficiency

The deuterium is identified among charge one particles by requiring no Cherenkov signal from the RICH detector, for rigidity values above the proton threshold for Cherenkov light emission. Nevertheless, the resulting subsample of selected particles contains a non-negligible component of protons, which must be estimated and subtracted. Since the deuteron identification is possible only using the RICH detector information, the background level has been determined by means of a simulation. The simulation has been used also to evaluate the selection efficiency for the deuterium.

The followed approach has been to develop an empirical response model of the instrument based on characteristic quantities obtained from experimental data. The basic functions needed to estimate the proton contamination and the deuteron selection efficiency are the spectrometer resolution function and the probability of zero detected photoelectron in the RICH detector as a function of the rigidity. Both these quantities can be obtained by experimental data, but require a good understanding of both the spectrometer and the RICH detector. In this chapter the analysis procedure developed to parameterize the instrument response is described.

The basic concept of the analysis is introduced in section 6.1. Section 6.2 is dedicated to the study of the RICH detector basic performances. In sections 6.3 and 6.4 the results concerning the probability of zero detected photoelectrons and the spectrometer resolution function are presented and discussed. In the final section 6.5 these two functions are used as input for the simulation. At the end of the section the estimated number of protons and deuterons in the spectrometer is presented.

6.1 Introduction

The proton background origin

The presence of protons without a Cherenkov signal, with measured rigidity above the threshold for Cherenkov light emission, is mainly due to the following two causes: the probability of zero detected photoelectrons, that is different from zero even above the rigidity threshold for Cherenkov light emission, and the uncertainty in the measured deflection.

The Cherenkov light emission and detection is a statistical process. The number of detected photoelectrons fluctuates around a mean value N_{pe} which is a function of the rigidity according to the relation 4.12. It follows that, even if the proton rigidity is above the threshold for Cherenkov light emission, the number of detected photoelectrons can be equal to zero, so that the criterion for deuteron selection is satisfied. The overall effect is that the probability to have no Cherenkov signal decreases gradually for increasing rigidity, starting from the Cherenkov rigidity threshold. The shape and the value of this probability as a function of the ratio R/R_{th} are an intrinsic characteristic of the RICH detector. In the following we refer to the **probability of no Cherenkov signal detected** using the notation P_{OFF}.

The detection of protons without a Cherenkov signal with a measured rigidity greater than the Cherenkov threshold is also a consequence of the finite resolution of the spectrometer. Its effect is the broadening of the distribution of protons without a Cherenkov signal, so that, as an example, a proton which has a rigidity under the Cherenkov threshold can be detected, due to the uncertainty in the measured deflection, with a rigidity value greater than the threshold. Also in this case the proton satisfies the criterion for the deuterium selection. The spectrometer response is characterized by the so called **spectrometer resolution function**, defined as the probability distribution function of the variable $\delta_{spec} = \eta_{spec} - \eta$, where η is the real deflection value[1]. The width of this distribution is related to the deflection uncertainty σ_η and, as a consequence, to the MDR parameter (see eq. 4.5). We refer to the spectrometer resolution function using the notation $f_{spec}(\eta; \delta_{spec})$, which expresses also its general dependence on the deflection η.

[1] In this chapter we refer to the measured deflection in the spectrometer using the notation η_{spec}, to distinguish this value from that one obtained from the RICH detector (η_{RICH}).

The distribution of background protons is related to P_{OFF} and f_{spec} as follows:

$$\frac{dN_{p,bk}}{d\eta_{spec}} = \int F_p(\eta)\, P_{OFF}(\eta)\, f^{he}_{spec}(\eta_{spec} - \eta)\, d\eta = (F_p P_{OFF}) * f^{he}_{spec}\,. \qquad (6.1)$$

In eq. 6.1, $N_{p,bk}$ is the number of background events, F_p is the proton deflection spectrum and $f^{he}_{spec}(\delta_{spec})$ denotes the high energy resolution function $f_{spec}(\eta \to 0; \delta_{spec})$, which does not depends on the deflection. The functions P_{OFF} and f^{he}_{spec} have been parameterized and the parameters have been derived from data.

The probability P_{OFF} of no Cherenkov signal detected

In order to estimate the probability of no Cherenkov signal detected muons from ground data have been used. The probability P_{OFF} is an intrinsic quantity of the RICH detector and, as a consequence, it does not depend on the particle type when it is expressed as a function of the variable R/R_{th}, or equivalently η/η_{th} (see section 4.4). The Cherenkov deflection threshold for muons is about 10 times greater than that of protons (eq. 4.13). It follows that the probability P_{OFF} as a function of the deflection varies for muons over a deflection range wider than for protons. As a consequence, the spectrometer uncertainty, which is constant in deflection, has a smaller effect on the distribution of muons without a Cherenkov signal than on the proton distribution.

If the deflection uncertainty is neglected, the probability P_{OFF} can be directly obtained from the distribution of muons without a Cherenkov signal, since the two quantities are related through the equation:

$$\frac{dN_{\mu,OFF}}{d\eta} = F_\mu(\eta) P_{OFF}(\eta)\,. \qquad (6.2)$$

In eq. 6.2, $N_{\mu,OFF}$ is the number of muons without a Cherenkov signal and F_μ is the muon deflection spectrum.

Nevertheless a non negligible effect results from the increase of the deflection uncertainty at low energy due to the multiple scattering inside the spectrometer. This would affect the estimate of the probability P_{OFF} obtained from eq. 6.2 and, as a consequence, the final estimate of the proton background in the deuteron sample (eq. 6.1). Taking into account the deflection uncertainty, the distribution of muons without a Cherenkov signal can be expressed, using the same notation of eq. 6.1, as:

$$\frac{dN_{\mu,OFF}}{d\eta_{spec}} = (F_\mu P_{OFF}) * f^{le}_{spec}\,, \qquad (6.3)$$

where f^{le}_{spec} denotes the low energy spectrometer resolution function. therefore, the probability P_{OFF} can be inferred from the muons experimental distribution after the unfolding of the spectrometer response. This procedure implies the knowledge of the low energy spectrometer resolution function f^{le}_{spec}.

The low energy spectrometer resolution function f^{le}_{spec}

There are two contributions to the deflection uncertainty. The first one is mainly related to the finite spatial resolution of the tracking system (eq. 4.3) and can be regarded as the intrinsic spectrometer uncertainty.

The second contribution comes from the multiple scattering effect. When a particle crosses the tracking volume it undergoes nuclear and Coulomb interactions with the medium nuclei. As a consequence, the particle deviates from its ideal trajectory. Since the deflection is estimated by fitting the experimental points with a smooth trajectory, obtained integrating the equations of motion (see section 4.3.2), this results in an error on the reconstructed deflection which is approximately given by [88]:

$$\sigma^{ms}_{\eta} \propto \frac{1}{\int B \times dl} \frac{Z}{p\beta} \sqrt{\frac{L}{X_{\circ}}}\,, \tag{6.4}$$

where Z is the electric charge of the incident particle, p is the momentum, L is the total track length and $X_{\circ}$ is the radiation length of the scattering medium.

From eq. 6.4 it follows that the multiple scattering contribution is negligible at high energy and increases for decreasing energy. At low energy, the variable δ_{spec} can be expressed as the sum of the two contributions:

$$\delta_{spec} = \delta^{ms}_{spec} + \delta^{int}_{spec}\,, \tag{6.5}$$

where δ^{ms}_{spec} and δ^{int}_{spec} refer respectively to the multiple scattering effect and the intrinsic spectrometer response. According to the definition of the spectrometer resolution function, f^{le}_{spec} is the probability distribution function of δ_{spec}. Since at high energy the multiple scattering contribution is negligible, f^{he}_{spec} is the probability distribution function of δ^{int}_{spec}, hence it can be regarded as the intrinsic spectrometer resolution function. If it is assumed that the two contribution are independent, the resulting low energy spectrometer resolution function can be expressed as:

$$f^{le}_{spec}(\eta;\delta_{spec}) = \int f^{ms}_{spec}(\eta;\delta)\, f^{he}_{spec}(\delta_{spec}-\delta)\, d\delta = f^{ms}_{spec} * f^{he}_{spec}\,. \tag{6.6}$$

Since the multiple scattering effect is energy dependent, f_{spec}^{ms} and therefore f_{spec}^{le} depend on the deflection. The function f_{spec}^{ms} is related only to the deviation of the particle track from the ideal trajectory, due to the particle interactions with medium nuclei. As a consequence it can be constructed without any assumption on the tracking system response. Assuming that f_{spec}^{he} is known, the low energy spectrometer resolution function can be obtained as the convolution of the two functions.

The high energy spectrometer resolution function f_{spec}^{he}

The high energy spectrometer resolution function has been estimated using protons from flight data. For rigidity values greater than the proton rigidity threshold for Cherenkov light emission the RICH provides an independent measurement of the particle deflection. This information is obtained from the reconstructed Cherenkov angle assuming the mass of a proton. We refer to this value using the notation η_{RICH}.

Likewise the spectrometer, the *RICH deflection resolution function* (f_{RICH}) is defined as the probability distribution function of the variable $\delta_{RICH} = \eta_{RICH} - \eta$. As will be shown in sec. 6.2.2, the probability distribution function of the Cherenkov angle is well represented by a Gaussian function with mean value $\Delta\theta_\circ$ and width σ_θ, where both the parameters depend on the deflection. The RICH resolution function is related to the above parameters through the relation:

$$f_{RICH}(\eta;\delta_{RICH}) = \frac{1}{\sqrt{2\pi}\,\sigma_\theta(\eta)}\,\exp\left[\frac{(\theta_c(\delta_{RICH}) - \Delta\theta_\circ(\eta))^2}{2\,\sigma_\theta(\eta)^2}\right]\,\left|\frac{d\theta_c}{d\delta_{RICH}}\right| . \qquad (6.7)$$

Given a sample of protons with a well reconstructed Cherenkov angle, for each event the following quantity can be calculated:

$$\xi = \eta_{spec} - \eta_{RICH} = \delta_{spec} - \delta_{RICH} . \qquad (6.8)$$

Since η_{spec} and η_{RICH} are independent, the proton distribution as a function of ξ is given by:

$$\frac{dN_p}{d\xi} = N_{p,TOT}\int \tilde{f}_{RICH}(\delta)\, f_{spec}^{he}(\delta-\xi)\, d\delta = N_{p,TOT}\cdot(\tilde{f}_{RICH} * f_{spec}^{he}) , \qquad (6.9)$$

where N_p^{tot} is the total number of selected protons. The function $\tilde{f}_{RICH}$ denotes the *mean RICH deflection resolution function* for the considered particle sample and it is related to f_{RICH} as follows:

$$\tilde{f}_{RICH}(\delta) = \int \frac{F_p(\eta)P(\eta)}{N_{p,TOT}}\, f_{RICH}(\eta;\delta)\, d\eta . \qquad (6.10)$$

In eq. 6.10, F_p is the proton spectrum and P denotes the selection efficiency for the conditions applied to ensure a well reconstructed angle.

Once $\tilde{f}_{RICH}$ is known, f^{he}_{spec} can be obtained from eq. 6.9 by applying an unfolding procedure.

The general procedure to estimate P_{OFF} and f^{he}_{spec}

The quantities P_{OFF} and f^{he}_{spec} have been inferred from experimental distributions, the former using ground muons and the latter using flight protons. By comparing the basic equations, it emerges that the procedures to obtain P_{OFF} and f^{he}_{spec} from data are not independent, because the experimental distributions are related to both. In fact, from eq. 6.3 follows that the procedure to estimate P_{OFF} implies the knowledge of f^{he}_{spec}. Beside that, f^{he}_{spec} is related to P_{OFF} through the probability P introduced in eq. 6.10 (this relation will be specified afterwards, in section 6.4). Therefore, an iterative procedure has been applied, starting from a rough estimate of P_{OFF} using eq. 6.2. The results converged at the second estimate of f^{he}_{spec}, since this quantity depends only weakly on P_{OFF}.

6.2 The RICH detector response

In order to study the RICH detector response, events from ground data have been used. At the ground level the detected particles are mostly muons. This allows to select large and clean samples of positive and negative muons, which are useful to study the RICH detector performances without the complications arising from the presence of particles of different kinds. Furthermore, as discussed in the previous section, when dealing with quantities related to the Cherenkov effect, the effect of the spectrometer uncertainty is smaller for light particles. If the spectrometer uncertainty is neglected[2], all the Cherenkov effect quantities derived from muons, expressed as a function of R/R_{th}, are only related to the RICH detector intrinsic behavior. From the experimental point of view, another advantage of expressing the Cherenkov relations as a function of R/R_{th} is that the effects of the rigidity threshold variations due to the refractive index fluctuations are reduced.

[2]We have made this assumption for all the RICH detector quantities but P_{OFF}. In this case data have been corrected by unfolding the spectrometer response (section 6.3).

The ground muon sample

The ground data sample has been taken with the CAPRICE telescope in the same configuration of the flight, immediately before the balloon launch. For this reason the results obtained from ground data are applicable to flight data after only some small corrections, which will be discussed afterwards.

The muon samples have been selected by first applying all the basic requirements for the deuteron analysis, summarized in table 5.1, excluding the requirement for the selection of $Z > 0$ particles (cut 4). The surviving events are essentially charge one particles with a well reconstructed track in the spectrometer. Among these, events having a non-interacting path in the calorimeter have been selected. This has been done by applying the calorimeter conditions summarized in table 6.1. In the table,

Table 6.1: *Criteria applied to select non-interacting particles in the calorimeter.*

Calorimeter selection	
1	$\sum_{i=1}^{8} n_x(i) \geq 3$ and $\sum_{i=1}^{8} n_y(i) \geq 3$
2	not more than one plane with multiple hits
3	$s = \sum_{i=1}^{8} [n_x(i) + n_y(i)] \cdot i > 40$

$n_{x(y)}(i)$ denotes the number of strip hits inside three Moliere radii around the particle track, in the $x(y)$ view of the i-th calorimeter plane. A minimum total number of hits has been required (cut 1), but those events with more than one plane having multiple hits have been excluded (cut 2). The quantity s, defined in the table, characterizes the topological development of the particle path in the calorimeter [95]. A lower limit on s has been required (cut 3), in order to reject low energy electrons that were absorbed in the upper layers of the calorimeter. The applied conditions efficiently eliminates the electron component, but the sample still contains a residual contamination of non-interacting protons. Then, among the surviving particles, positive and negative muons have been selected by requiring $\eta > 0$ or $\eta < 0$, respectively.

6.2.1 The maximum number of detected photoelectrons

The overall performances of the RICH detector are strictly connected to the number of detected photoelectrons. The greater is this number the lower is the error on the measured Cherenkov angle. Furthermore, a large number of detected photoelectrons is also

important if the RICH detector is used as a threshold device, since this identification method is affected by Poisson fluctuations.

Data do not give a direct information on the number of detected photoelectrons. The signal of each photoelectron, as discussed in section 6.2.2, spreads over several pads and there is an high probability that one pad could collect charge induced by several photoelectrons. Nevertheless an estimate can be obtained from the effective number of pads N_{eff} [93]. According to eq. 4.12, for relativistic particles the number of detected photoelectrons has a constant mean value N_{pe}^{max}. The resulting mean effective number of pads is also constant and equal to $\langle N_{eff} \rangle = kN_{pe}^{max}$. Since the number of detected photoelectrons follows the Poisson statistic, the variance of N_{eff} is given by $var(N_{eff}) = k^2 N_{pe}^{max}$. By combining the two relations it follows that the maximum number of detected photoelectrons can be estimated as:

$$N_{pe}^{max} = \frac{\langle N_{eff} \rangle^2}{var(N_{eff})} \,. \tag{6.11}$$

The above procedure has been applied to a sample of relativistic negative muons with a measured rigidity $R > 12R_{th}$, where R_{th} is the Cherenkov threshold rigidity for muons. The positive muons have been excluded since the residual proton contamination could affect the final estimate of N_{pe}^{max}. In fact, the positive charge sample contains also protons for which the number of detected photoelectrons has not reached its maximum value. The quantities $\langle N_{eff} \rangle$ and $\sqrt{var(N_{eff})}$ have been estimated as the mean value and the root mean square of N_{eff} for the sample. The result is shown in the first row of tab. 6.2.

Table 6.2: *The maximum number of detected photoelectrons from flight and ground data.*

	$\langle N_{eff} \rangle$	RMS	N_{pe}^{max}
ground	45.7 ± 0.6	10.1 ± 0.4	20.6 ± 1.7
flight	40.7 ± 0.9	10.0 ± 0.7	16.6 ± 2.3

6.2.2 The Cherenkov angle resolution

To study the angular resolution of the RICH detector both negative and positive muons have been used. In this case the residual proton contamination does not affect significantly the result, so that the positive muons have been included in order to have a larger statistic.

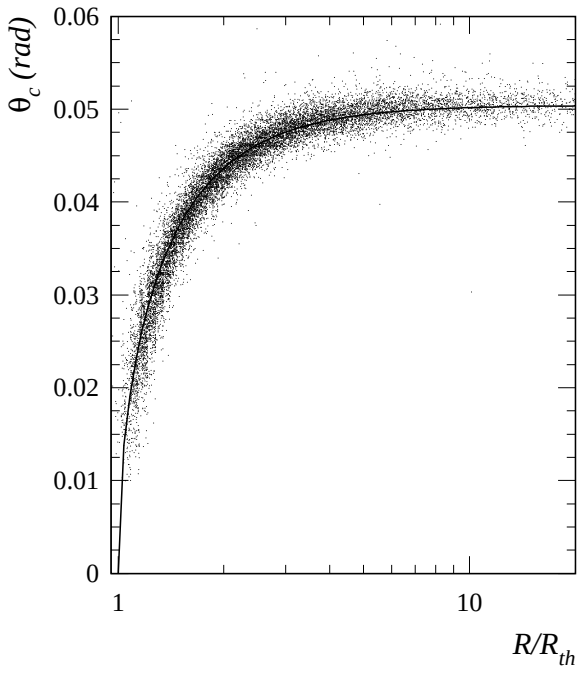

Figure 6.1: *The measured Cherenkov angle as a function of R/R_{th} from ground muons. Solid curve: expected theoretical Cherenkov angle.*

Fig. 6.1 shows the distribution of the measured Cherenkov angle as a function of R/R_{th} for the selected sample. The solid curve represents the theoretical value (θ_c^{theor}) calculated from eq. 4.12; the Cherenkov angle increases for increasing rigidity, up to an asymptotic value of $\theta_c^{max} \sim 50.42$ mrad.

Fig. 6.2 shows the distribution of the difference $(\theta_c - \theta_c^{theor})$ between the measured Cherenkov angle and its theoretical value, for a sample of relativistic muons. The solid curve represents a Gaussian fit to the data, with reduced $\chi^2 \sim 1.1$. The width of the Gaussian function, which is ~ 1.1 mrad, represents the RICH detector angular resolution for relativistic particles, when both the number of detected photoelectrons and the Cherenkov angle have their maximum value.

Fig. 6.3 (left plot) shows the measured angular resolution as a function of R/R_{th}. The plotted values have been obtained by dividing data in several rigidity bins and by applying a Gaussian fit to the distributions of the variable $\theta_c - \theta_c^{theor}$ obtained for each bin. One can see that the RICH angular resolution is rigidity dependent. Its value increases for decreasing rigidity up to a value of ~ 3.2 mrad near the Cherenkov rigidity threshold, following the decrease of the effective number of pads involved in the angle reconstruction. In the right plot of fig. 6.3 the center of the fitted Gaussians is also

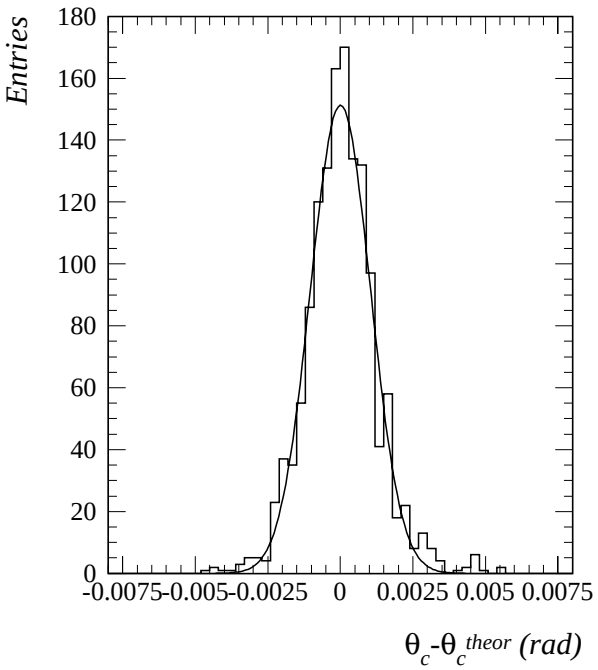

Figure 6.2: *Distribution of the difference between the measured Cherenkov angle and its expected theoretical value, for a sample of relativistic muons. Solid curve: a Gaussian fit to the data.*

shown as a function of R/R_{th}. It can be noticed that there is a small systematic shift of the measured Cherenkov angle towards values lower than the expected theoretical one. We attributed the observed shift to an effect resulting from the discretization of the signal due to the pad plane segmentation, which could have a crucial role at small Cherenkov angles.

The dashed curves in fig. 6.3 show the given parameterizations for both the angular resolution (σ_θ) and the shift ($\Delta\theta_\circ$), obtained by fitting experimental data. The expressions of the plotted functions are the following[3]:

$$\sigma_\theta(R/R_{th}) = 1.07 \left[1 - \left(0.84\frac{R_{th}}{R}\right)^2\right]^{-1.45} \text{ mrad} \quad (6.12)$$

$$\Delta\theta_\circ(R/R_{th}) = \max\left\{-1.11, -1.76\ exp\left[-2.17\left(\frac{R}{R_{th}}\right)\right]\right\} \text{ mrad}\,, \quad (6.13)$$

which holds for $R > 1.15R_{th}$. The parameterization below this value is not significant for the present analysis.

[3]Here and in the following all the parameter values are presented without specifying the error but expressing the number up to the last significant digit. The error values are reported only if they are involved directly in the discussion.

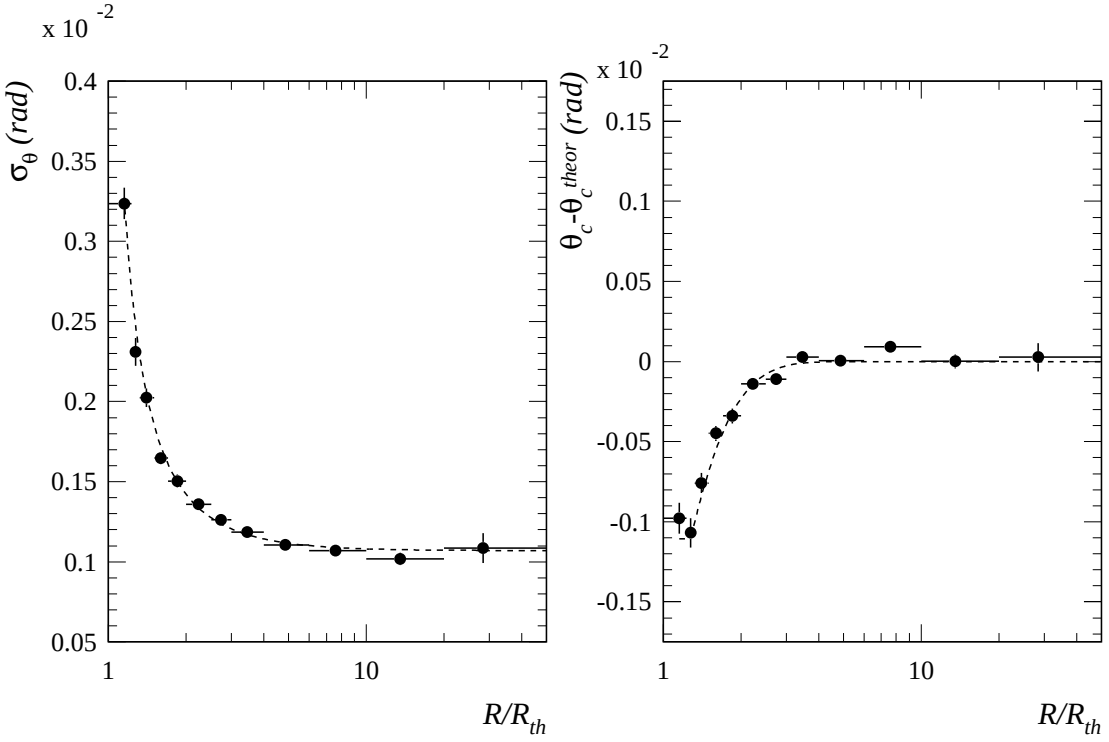

Figure 6.3: *Left plot: the measured Cherenkov angle resolution as a function of R/R_{th}. Right plot: difference between the measured Cherenkov angle and the expected theoretical value. Dashed curves: a fit to the data.*

6.2.3 Performances during the flight

The RICH detector response has been parameterized by using ground data. In order to make a comparison between the RICH detector response at ground and during the flight, it is useful to refer to the plot of the effective number of pads N_{eff} as a function of $sin^2\theta_c$. This is shown in fig. 6.4, where the filled circles refer to flight data while the open circles refer to ground muons. The flight sample, which contains mostly protons, has been selected by applying the basic cuts described in table 5.1, plus the requirements of $R > 10$ GV and $N_{eff} > 0$. Since N_{eff} is in first approximation proportional to the number of detected photoelectrons N_{pe}[4], from eq. 4.12 and 4.10 it follows that the two variables N_{eff} and $sin^2\theta_c$ are linearly dependent, with a proportionality constant which is directly related to the detector response parameter

[4]The relation between N_{eff} and N_{pe} is connected to the MWPC response. In this discussion it is assumed that the MWPC behavior was the same at ground and during the flight. This point will be further discussed in section 6.3.3 and in appendix B where it will be shown that this assumption is reliable.

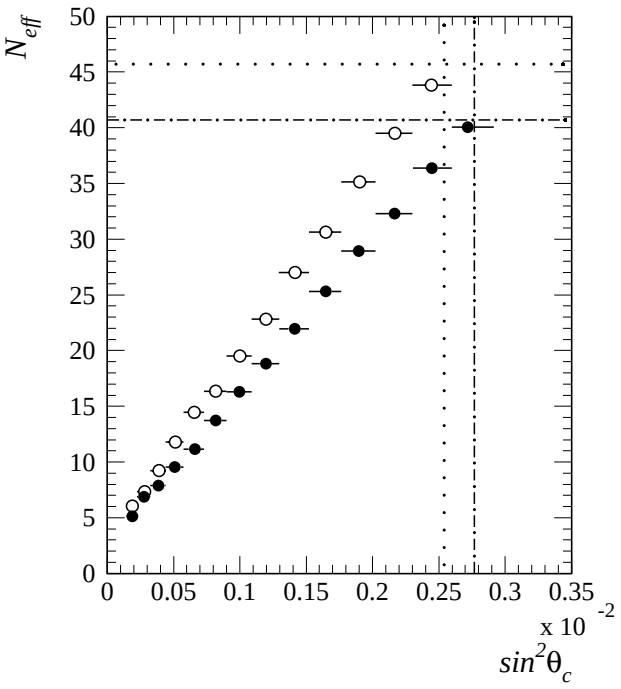

Figure 6.4: *The mean effective number of pads as a function of the squared sine of the Cherenkov angle. Filled circles: flight data. Open circles: muons from ground data. Dotted lines: N_{eff}^{max} and $sin^2\theta_c^{max}$ from ground data. Dotted-dashed lines: N_{eff}^{max} and $sin^2\theta_c^{max}$ from flight data.*

$N_\circ$. From fig. 6.4 it is inferable that the response parameter of the detector during the flight was slightly lower than at ground. This was due to different pressure and temperature conditions of the gas radiator during the flight, which affected both the refractive index of the radiator and the photoelectron absorption length. The dotted lines in fig. 6.4 represents the values of N_{eff}^{max} and $sin^2\theta_c^{max}$ obtained from relativistic ground muons as described in section 6.2.1 and 6.2.2 respectively. The same procedures has been applied to flight data and the results are shown by dotted-dashed lines in the same figure. The maximum number of detected photoelectrons in the flight conditions has also been estimated[5] and the result is presented in tab. 6.2. The variation of the gas radiator conditions during the flight resulted in an higher value of θ_c^{max}, which was due to the increase of the refractive index. The parameter N_{pe}^{max} is instead related also to the photoelectron transmission factor of the radiator, which led to a lower number of detected photoelectrons at float.

[5]During the flight there were refractive index fluctuations due to the gas pressure variations [92, 93]. This led also to fluctuations in the mean number of detected photoelectrons which could invalidate the estimate of N_{pe}^{max} obtained from N_{eff} as described in section 6.2.1. Nevertheless the uncertainty due to this effect resulted to be negligible if compared with the statistical error.

6.3 The probability P_{OFF} of no Cherenkov signal detected

According to the procedure described in section 6.1, the probability P_{OFF} has been obtained by unfolding the muon data from the distortions due to the spectrometer finite resolution. The unfolding procedure implies the knowledge of the low energy spectrometer resolution function f^{le}_{spec}, which has been evaluated by means of a simulation.

6.3.1 The low energy spectrometer resolution function f^{le}_{spec}

The low energy spectrometer uncertainty is in first approximation given by two independent contributions, which are due to the intrinsic spectrometer resolution function and the multiple scattering effect, respectively. Under the independence hypothesis the whole resolution function is given by the convolution of the resolution functions related to the two contributions (eq. 6.6). The followed approach has been to construct the low energy spectrometer resolution function on an event-by-event basis by means of a simulation.

The CAPRICE98 simulation program has been used. The program includes the code developed to study the calorimeter [95]; all the other detectors, but the scintillators, are simulated only from the point of view of the geometry and the materials. As a consequence, if we consider the simulation output relative to the spectrometer, the only physical process included is the multiple scattering with the medium nuclei. The reconstruction algorithm has been applied to the simulated tracks. The resulting difference between the reconstructed deflection and the generated value is distributed according to the probability distribution function f^{ms}_{spec}, defined in section 6.1. In order to simulate the whole detector response, the intrinsic spectrometer contribution δ^{int}_{spec}, generated event-by-event according to f^{he}_{spec}, has been added to the deflection value obtained from the fitting routine. Since the two contributions have been generated independently the probability distribution function of the resulting deflection is f^{le}_{spec} as defined in eq. 6.6.

In order to check if the procedure reproduces the spectrometer resolution function at an adequate approximation level, the result of the simulation has been compared with experimental data obtained from a ground run with the magnet switched off. The

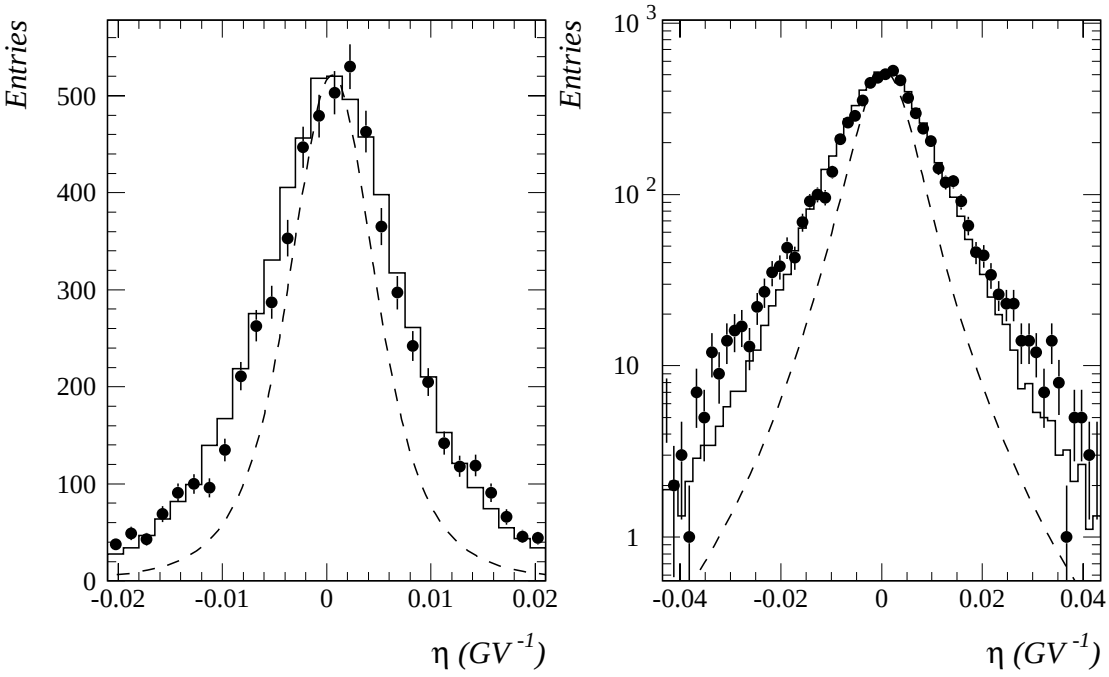

Figure 6.5: *The low energy spectrometer resolution function. Filled circles: experimental deflection distribution obtained from magnet-off ground data with the requirement of a Cherenkov signal from the RICH detector. Solid line: the same distribution obtained from the simulation, normalized to the total number of events. Dashed curve: the high energy spectrometer resolution function (eq. 6.26). The same plot is shown in both linear (left plot) and logarithmic (right plot) scale.*

basic cuts listed in tab. 5.1 have been applied to the data. The sample has then been cleaned from low energy electrons by applying the calorimeter conditions of tab. 6.1. The resulting sample of events consists of straight tracks which have been analyzed as if they were high rigidity events with magnet on. In this spectrometer configuration the measured deflection distribution gives directly the spectrometer resolution function.

The low energy spectrometer uncertainty depends on both the particle energy and the intensity of the magnetic field along the particle track (see equations 4.3 and 6.4). The super-conducting magnet provides a large inhomogeneous field that results in a dependence of the spectrometer uncertainty on the track position inside the tracking volume. Since the observed resolution function is averaged over the full tracking volume and over the muon spectrum, to get a reliable comparison between data and simulation the input kinematic parameters of the simulated track sample must reproduce the

energy and spatial distributions of the real tracks.

A large sample of muons has been simulated with the magnetic field set to zero. The muon rigidity has been generated according to the experimental ground spectrum obtained from muons collected with the magnet switched on. Since the presence of the magnetic field affects the geometrical factor below 1 GV, the rigidity distribution of the particles entering the spectrometer is different if the magnet is on or off. For this reason, to reproduce the magnet-off rigidity distribution, muons have been selected by requiring the presence of a Cherenkov signal from the RICH detector. This condition allows the selection of muons with rigidity greater than ~ 2 GV. Above this value GF is constant. The starting input data of the tracks have been generated according to the angular and spatial experimental distributions obtained from magnet-off data.

Fig. 6.5 shows the comparison between the simulated resolution function (solid line) and the deflection distribution obtained from magnet-off data (filled circles). The simulated distribution has been normalized to the total number of events. From the quite good agreement between data and simulation it follows that the model reproduces the main characteristics of the spectrometer response at low energy. For comparison, the high energy spectrometer resolution function f_{spec}^{he} is also shown by dashed curve.

The observed differences between the distributions shown in fig. 6.5 are probably due to two main reasons. The first one lies on the assumption that the whole deflection uncertainty is given by two independent contributions. In principle this could be a good approximation if the magnetic field was uniform. Since this is not the case, the multiple scattering and the intrinsic contributions are correlated. This means, as an example, that if a particle crosses the tracking volume in a low field region, both the contributions to the deflection error are most probably greater than their averaged value. These events contribute to the tails of the experimental deflection distribution shown in fig. 6.5.

There is a second assumption that can account for the disagreement between data and simulation. In order to simulate the intrinsic response of the spectrometer, the high energy resolution function obtained from flight data has been used. The magnet off data came instead from a ground run taken some weeks before the flight (9 April). Between this run and the flight there was a further launch that failed, which has led to slight mechanical distortion of the payload structure. As a consequence, the spectrometer performance during the magnet-off run could be slightly different than

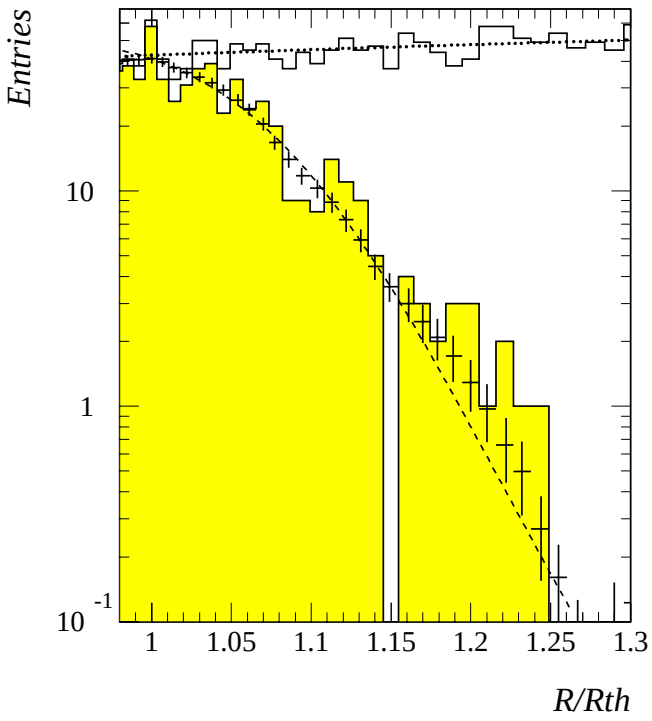

Figure 6.6: *Distribution of muons from ground data. Solid line: total muon distribution. Shaded area: distribution of muons without a Cherenkov signal. Crosses: distribution of muons without a Cherenkov signal after the unfolding of the low energy resolution function. Dashed and dotted curves: results of the fit (equations 6.14 and 6.15).*

during the flight, resulting in a different intrinsic resolution function. The magnet on data come instead from a run taken only some days before the flight (24 May). During the acquisition of these data the instrument was in the flight configuration, so that the assumption is expected to be more reliable.

6.3.2 The unfolding result

The probability of zero detected photoelectrons has been obtained using negative muons from ground data. The positive sample has been excluded because of the residual contamination of protons, which around the muon Cherenkov rigidity threshold do not emit Cherenkov light and could invalidate the resulting estimate of the probability P_{OFF}. In fig. 6.6 the number of muons without a Cherenkov signal ($N_{\mu,OFF}$) is shown (shaded area) as a function of R/R_{th}. In the same plot the total number of muons (N_{μ}) is also shown (solid line).

The probability P_{OFF} has been obtained by unfolding the low energy resolution function f^{le}_{spec} from the distribution of muons without a Cherenkov signal (see eq. 6.3). The developed unfolding procedure is based on the Bayesian unfolding method de-

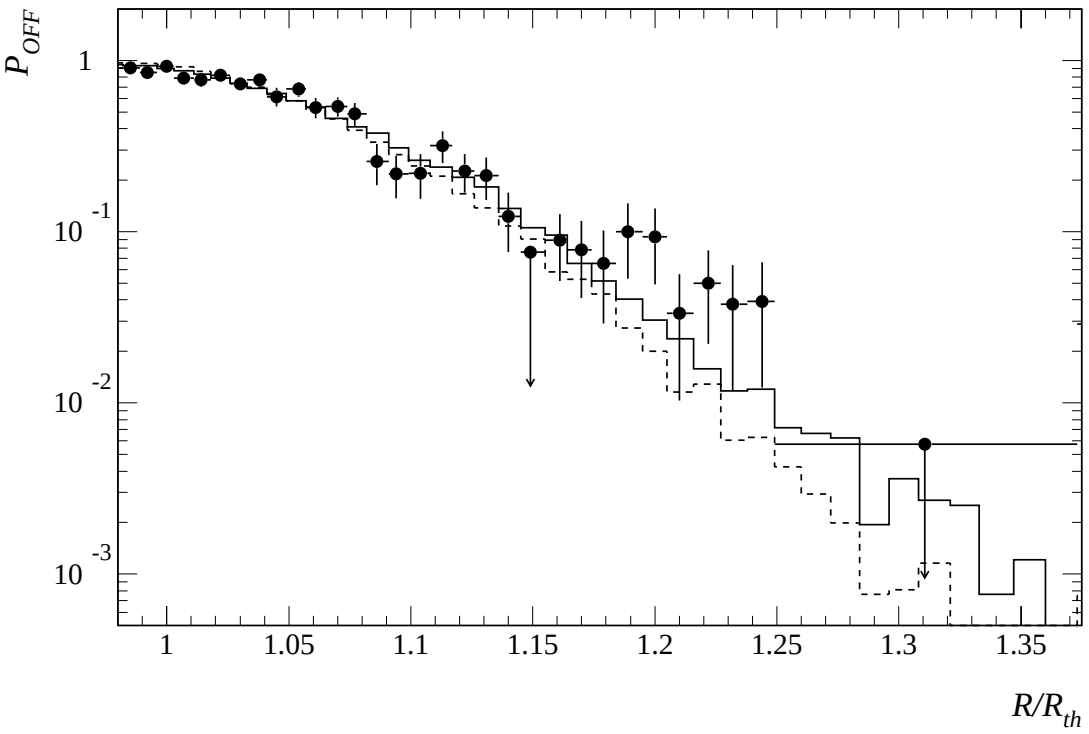

Figure 6.7: *Probability P_{OFF} of no Cherenkov signal detected estimated according to eq. 6.16. Solid line: simulated data, by taking into account the spectrometer uncertainty. Dashed line: simulate data, without taking into account the spectrometer uncertainty. Filled circles: experimental data.*

scribed in reference [98]. This method was chosen since it can easily take into account any kind of detector response. The basic input of the method is the probability for an event occurring in the i-th bin to be recorded, due to the finite instrument resolution, in the j-th bin. In this case this probability is related to f^{le}_{spec}, which is rigidity-dependent, and has been constructed by simulation as described in section 6.3.1. The crosses in fig. 6.6 represent the result of the unfolding procedure[6].

In order to obtain P_{OFF} the total muon distribution has been parameterized with

[6]The error bars shown in the picture refer to the square root of the variance obtained propagating the statistical errors on experimental data. The unfolded points have also some degree of correlation that we did not take into account in the fitting procedure.

a power law as follows:

$$dN_{\mu}(R/R_{th}) = 42.6 \left(\frac{R}{R_{th}}\right)^{0.62} . \tag{6.14}$$

The function 6.14 has been obtained by fitting experimental data and is indicated by dotted line in figure 6.6. The probability P_{OFF} has then been derived by fitting the unfolded distribution with the function:

$$dN_{\mu,OFF}(R/R_{th}) = 42.6 \left(\frac{R}{R_{th}}\right)^{0.62} P_{OFF}\left(R/R_{th}\right) , \tag{6.15}$$

where P_{OFF} is a parametric function of the variable R/R_{th}, which expression is specified and discussed in section 6.3.3. The result of the fit is shown in fig. 6.6 by dashed curve.

The effect of the unfolding procedure is difficult to evaluate from fig. 6.6. In order to visualize it, the probability P_{OFF} resulting from the fit of the unfolded data has been used to simulate a sample of muons. Fig. 6.7 shows the comparison between the probability P_{OFF} obtained as

$$P_{OFF} = \frac{N_{\mu,OFF} + 1}{N_{\mu} + 2} \tag{6.16}$$

from the simulated data, by including (solid line) and without including (dashed line) the deflection error. By comparing the solid and dashed lines it can be deduced that the spectrometer uncertainty gives a small but not negligible effect. In fig. 6.7 it is also shown for comparison the probability P_{OFF} obtained according to eq. 6.16 from experimental data (filled circles).

6.3.3 Parameterization of P_{OFF}

Theoretically the probability of no Cherenkov signal detected is expected to be described by the Poisson probability $\mathcal{P}$ of zero detected photoelectrons, when the expected number is N_{pe}:

$$P_{OFF}(R/R_{th}) = \mathcal{P}(0; N_{pe}) = P_{\circ}\, e^{-N_{pe}} , \tag{6.17}$$

where N_{pe} is rigidity dependent according to the relation (see eq. 4.12):

$$N_{pe}(R/R_{th}) = N_{pe}^{max} \left[1 - \left(\frac{R_{th}}{R}\right)^2\right] . \tag{6.18}$$

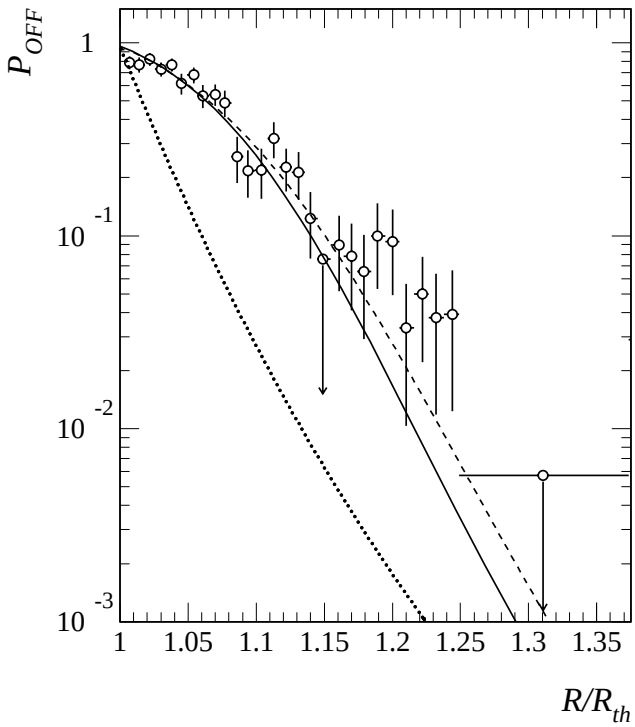

Figure 6.8: *The probability P_{OFF} of no Cherenkov signal detected. Open circles: probability obtained from ground muon data according to eq. 6.16. Dotted curve: probability as expected from Poisson statistics. Dashed curve: parameterization derived by fitting experimental points. Solid curve: parameterization obtained after the correction for the spectrometer effect.*

In equations 6.17 and 6.18, both the parameters $P_\circ$ and N_{pe}^{max} can be determined independently from the described procedure to estimate P_{OFF}. $P_\circ$ is related to the probability to have a signal in the MWPC which is not induced by Cherenkov photoelectrons but, as an example, by the instrument noise. This parameter has been determined using particles below the threshold for Cherenkov light emission. The value obtained from ground muons is $P_\circ = 0.962 \pm 0.006$. The parameter N_{pe}^{max} represents the maximum number of detected photoelectrons. Its value has been estimated as described in section 6.2.1 and the result obtained from ground data is $N_{pe}^{max} = 20.6 \pm 1.7$ (tab. 6.2).

In fig. 6.8 the function 6.17 (dotted curve), with N_{pe} obtained from eq. 6.18, is compared with the probability P_{OFF} obtained from experimental data according to eq. 6.16 (open circles). It can be seen that the two quantities differ of a large amount. This is true even after the unfolding of the spectrometer resolution function. In fact, as a result of the procedure described in the previous section (eq. 6.15), the unfolded data are well described using for P_{OFF} the eq. 6.17 with N_{pe} given by the following

function:

$$N_{pe}\left(R/R_{th}\right) = N_{pe}^{max}\left[1-\left(\frac{R_{th}}{R}\right)^2\right] K(R/R_{th})\,, \tag{6.19}$$

where $K(R/R_{th})$ has the parametric expression:

$$K(R/R_{th}) = \left[1+\exp\left(\frac{1.149-R/R_{th}}{0.088}\right)\right]^{-1}\,. \tag{6.20}$$

This is the expression of the solid curve shown in fig. 6.8. In the same figure it is shown, for comparison, this same function (dashed curve) with parameters obtained by fitting data without the spectrometer correction. Eq. 6.19 differs from eq. 6.18 for the rigidity dependent factor $K(R/R_{th})$ that multiplies the expected number of detected photoelectrons. The RICH detector behaves as if the photon detection efficiency increases for increasing particle rigidity, starting from the rigidity threshold up to an asymptotic value which results in N_{pe}^{max} detected photoelectrons. An effect of this kind can be accounted by some technical features of the RICH MWPC, which are discussed in appendix B. In the following the discussion of the instrument response model is continued, taking as the best estimate of P_{OFF} the equations 6.17 and 6.19 with the the empirical correction factor $K(R/R_{th})$ obtained by fitting the unfolded experimental data (eq. 6.20).

6.3.4 Scaling from ground to flight conditions

The described parameterization of the probability P_{OFF} reproduces the RICH detector response at ground. Since the detector conditions during the flight were different, the parameters which define P_{OFF} must be properly scaled in order to reproduce the flight performances.

The probability P_{OFF} has been described by four parameters: $P_\circ$, N_{pe}^{max} and the two parameters that define the correction factor $K(R/R_{th})$. The parameter $P_\circ$ is mainly related to the MWPC noise. Its value during the flight has been estimated as the fraction of particles without a Cherenkov signal below the proton rigidity threshold for Cherenkov light emission, obtaining a value consistent with the ground value, within the experimental errors. The correction factor $K(R/R_{th})$ is related, according to our interpretation, to the characteristics of the MWPC, which did not changed significantly at float (see appendix B). The above considerations suggest that both $P_\circ$ and $K(R/R_{th})$ were unchanged during the flight.

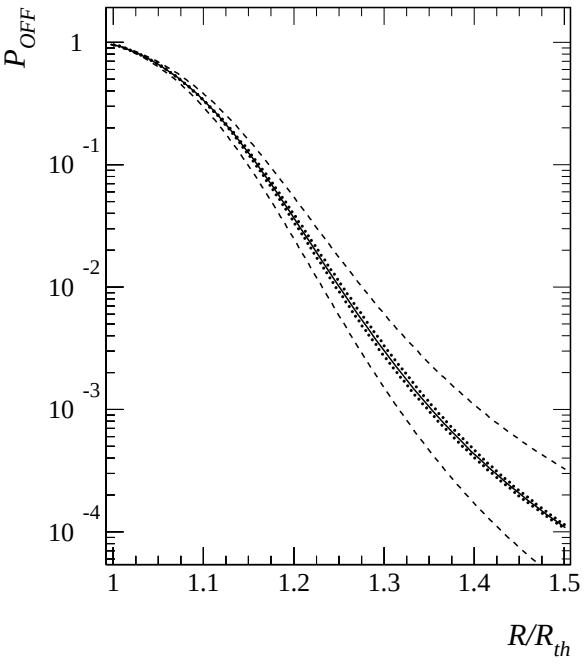

Figure 6.9: *Uncertainties on the probability P_{OFF}. Solid curve: best estimate of P_{OFF}. Dotted curves: upper and lower bounds derived from the statistical errors on the parameters that defines $K(R/R_{th})$. Dashed curves: upper and lower bounds derived from the statistical error on N_{pe}^{max}.*

On the contrary, as discussed in section 6.2.3, the gas radiator conditions changed from ground to the flight. This resulted in a different number of detected photoelectrons. It has been found that in flight $N_{pe}^{max} = 16.6 \pm 2.3$ (see tab. 6.2).

In conclusion, The probability P_{OFF} has been parameterized according to equations 6.17 and 6.19, with N_{pe}^{max} scaled to the flight value. therefore, the resulting expression of P_{OFF} used to reproduce the flight performances has been:

$$P_{OFF}(R/R_{th}) = 0.962\, e^{-N_{pe}}\ , \tag{6.21}$$

with N_{pe} given by:

$$N_{pe}\,(R/R_{th}) = 16.6\ \left[1 - \left(\frac{R_{th}}{R}\right)^2\right]\ \left[1 + \exp\left(\frac{1.149 - R/R_{th}}{0.088}\right)\right]^{-1}\ . \tag{6.22}$$

6.3.5 Systematic effects

The whole procedure to estimate the probability P_{OFF} at float lays on several assumptions. The resulting uncertainties have a systematic effect on the determination of the proton background distribution. For this reason any significant source of indetermination has been investigated and their relative contributions have been evaluated. The main ones are summarized in the following list.

1. The procedure to construct the low energy spectrometer resolution function f^{le}_{spec}. On this procedure is based the correction of the distribution of muons without a Cherenkov signal for the spectrometer resolution at low energy (section 6.3.1).

2. The statistical errors on the parameters that define the correction factor $K(R/R_{th})$, obtained by fitting the unfolded ground muon distribution (section 6.3.2).

3. The interpretation of the parameterization used to reproduce the observed shape of P_{OFF} for ground muons (appendix B). The criterion applied to scale from ground muons to flight protons are based on the assumption that the correction factor $K(R/R_{th})$ and the parameter $P_\circ$ depend only on the MWPC response which did not change (section 6.3.4).

4. The statistical error on the parameter $P_\circ$, which has been estimated from muons with rigidity under the threshold rigidity for Cherenkov light emission (section 6.3.3).

5. The statistical error on the parameter N^{max}_{pe}, which has been obtained from relativistic flight protons (section 6.2.3).

The item 1 has been discussed partially in section 6.3.1, where the procedure to construct f^{le}_{spec} has been checked by comparing the result with magnet-off muon data. From the comparison it emerged that the experimental low energy resolution function is slightly wider than the simulated one. If the observed disagreement is attributed entirely to the low energy spectrometer model, this should affect the estimate of P_{OFF}. In order to evaluate the resulting effect, the spectrometer response function in the unfolding routine has been modified according to the relative difference of the two distributions shown in fig. 6.5[7]. The difference on the correction factor $K(R/R_{th})$ obtained by fitting the new unfolded distribution has been found to be of the same order of magnitude of the errors on the parameters (item 2).

The item 3 is discussed in appendix B, where it is shown that the interpretation of $K(R/R_{th})$ is plausible. Under this hypothesis, all the examined data suggest that the MWPC performances did not change during the flight. As a consequence, the item 3 is expected to not affect significantly the final estimate of the probability P_{OFF}.

[7]This is not a rigorous procedure, since the resolution function estimated from magnet-off data is averaged over the muon the energy. Therefore, this correction procedure has been used only to evaluate its systematic effect on the estimate of the proton background.

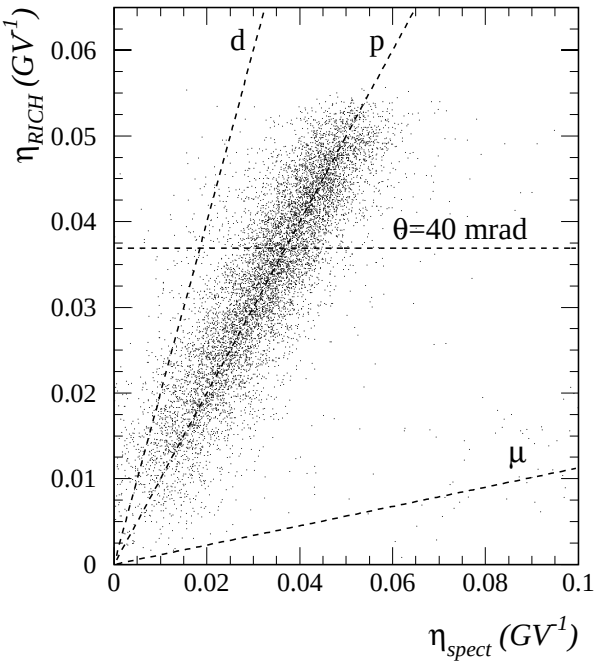

Figure 6.10: *Plot of the deflection derived from the reconstructed Cherenkov angle assuming a mass of a proton (η_{RICH}) as a function of the deflection measured with the spectrometer (η_{spec}). Inclined dashed lines: expected shape for deuterons, protons and muons. Horizontal dashed line: applied cut on the Cherenkov angle (the selected sample include events above this line).*

In fig. 6.9 the upper and lower bounds (dashed curves) of P_{OFF} derived from the statistical error on N_{pe}^{max} (item 5) are compared with the bounds set by the errors on the fitted parameters (item 2). From the comparison it follows that, above the Cherenkov threshold, the dominant contribution comes from the error on N_{pe}^{max}. The error on $P_\circ$ (item 4) determines the uncertainty on P_{OFF} below the Cherenkov threshold rigidity. Above the threshold it gives a contribution which is instead of the same order of magnitude of that coming from the item 2.

6.4 The high energy spectrometer resolution function f_{spec}^{he}

The high energy spectrometer resolution function has been estimated from flight protons by using the deflection information given by the RICH detector. The value of η_{RICH} has been obtained from the measured Cherenkov angle assuming a mass of a proton. In fig. 6.10 this quantity is plotted as a function of the deflection η_{spec} measured with the spectrometer, for a sample of particles selected by applying all the basic selection criteria of tab. 5.1 plus the requirement $N_{eff} > 10$. This latter condition has been required to reduce the contamination of events having a signal in the RICH detector

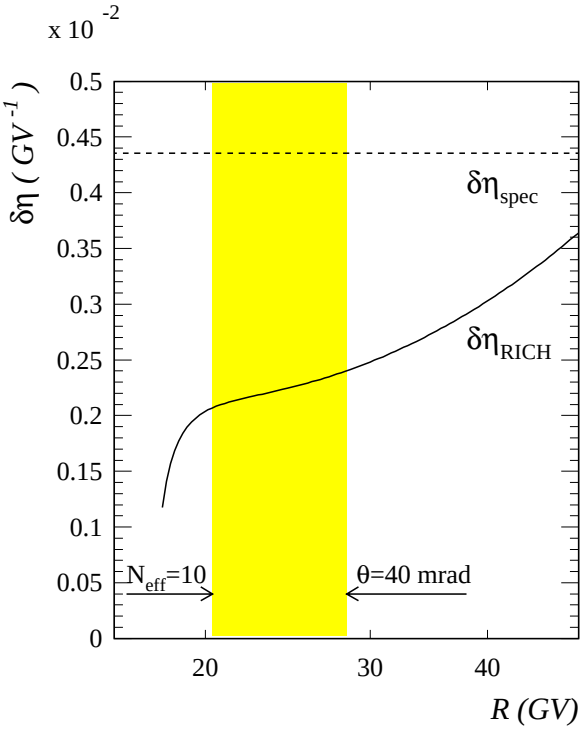

Figure 6.11: *Solid line: theoretical uncertainty in the deflection measured with the RICH detector, obtained propagating the error on the reconstructed Cherenkov angle. Dashed line: mean spectrometer deflection error given by the fitting routine. Shaded area: rigidity range corresponding to the applied selection cuts.*

due to noise. For these events the reconstructed value of η_{RICH} is meaningless and their presence would affect the final result. In the same plot the expected shapes for different particles are shown by dashed lines. One can notice that the sample contains mostly protons, with a small fraction of deuterons and positive muons.

As described in section 6.1 the high energy spectrometer resolution function f^{he}_{spec} has been evaluated from the distribution of the variable $\xi = \eta_{spec} - \eta_{RICH}$, by unfolding the mean RICH deflection resolution function. In order to get a reliable result from the unfolding procedure it is useful to minimize the RICH deflection uncertainty. This reduces the systematic effect on the final estimate of f^{he}_{spec} due to the uncertainty in the construction of the mean RICH deflection resolution function $\tilde{f}_{RICH}$ (eq. 6.10). Therefore, a further cut has been applied, by requiring that the Cherenkov angle was less than 40 mrad. In fig. 6.11 the theoretical error ($\delta\eta_{RICH}$) on the variable η_{RICH} for protons is plotted as a function of the rigidity and the range corresponding to the two applied selection criteria is highlighted by shaded area. In the same figure this quantity is compared with the mean spectrometer uncertainty given by the track fitting routine for the sample ($\delta\eta_{spec} = \langle\sigma_\eta\rangle$). The maximum value of the reconstructed Cherenkov angle has been chosen in order to minimize the RICH deflection uncertainty while

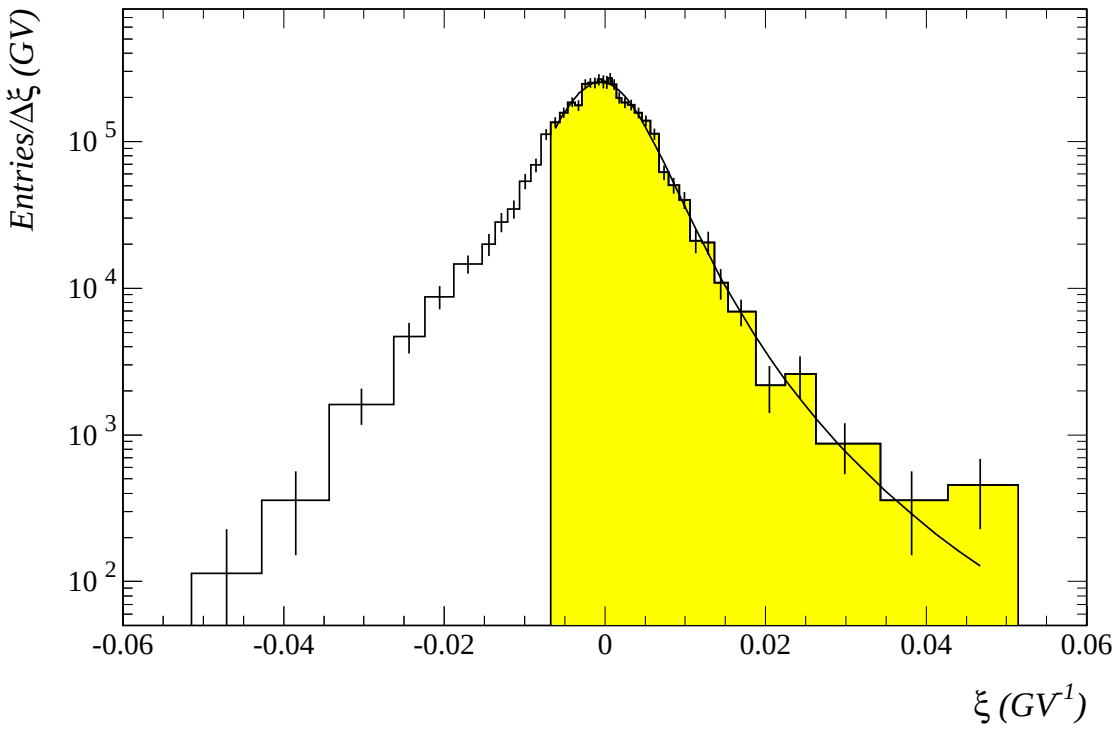

Figure 6.12: *Differential distribution of the number of selected protons as a function of the variable* $\xi = \eta_{spec} - \eta_{RICH}$. *Solid curve: result of the fit, performed in the range highlighted by the shaded area.*

maintaining the statistic as larger as possible. The effect of the cut $\theta_c < 40$ mrad on the sample can be seen in fig. 6.10, where it is represented by the horizontal dashed line. The selected particles are those above this line. Notice that this cut also reduces the muon contamination.

The differential distribution as a function ξ for the particle sample satisfying all the requirements is shown in fig. 6.12.

6.4.1 The mean RICH deflection resolution function

The procedure to determine the high energy resolution function, discussed in section 6.1, implies the knowledge of the mean RICH deflection resolution function $\tilde{f}_{RICH}$, which is defined by eq. 6.10. This function has been constructed by means of a simulation.

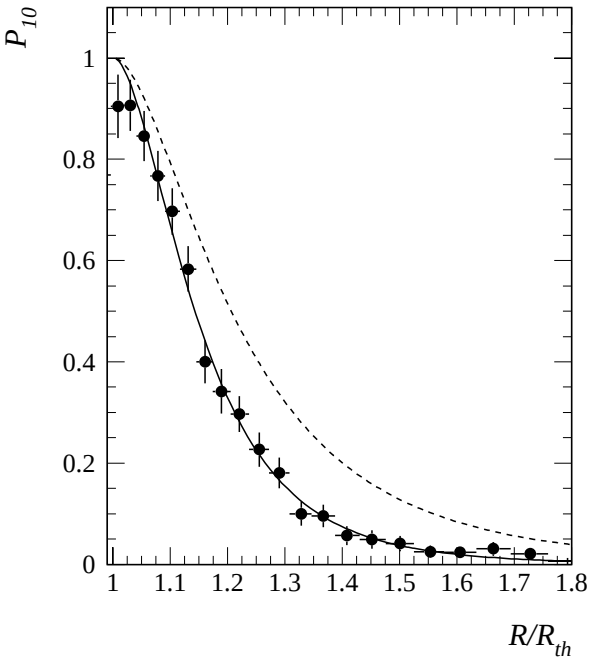

Figure 6.13: *Probability for a particle giving a Cherenkov signal to have $N_{eff} \leq 10$. Filled circles: probability obtained from ground negative muons. Solid curve: a fit to the data. Dashed curve: the fitted function scaled to flight conditions.*

A large sample of protons has been generated according to the following rigidity spectrum:

$$F_p(R) \propto \left[R + 1.05 \exp\left(\frac{-R}{11.89}\right)\right]^{-5.11} R^{2.20} \; . \tag{6.23}$$

The above parameterization has been obtained from experimental data by fitting the spectrum of the particles satisfying all the basic cuts (tab. 5.1).

For each generated rigidity value, the selection probability P, introduced in eq. 6.10, has been simulated in two steps. The probability P_{OFF} has been first used to tag those particles giving a signal in the RICH detector. The second step has been to simulate the probability to pass the selection requirement $N_{eff} > 10$. This latter information has been obtained from ground negative muons. Fig. 6.13 (filled circles) shows the probability (P_{10}) for a particle giving a signal in the RICH detector to be rejected by the cut on the effective number of pad hits. In order to parameterize the probability P_{10} it has been assumed that the cut $N_{eff} > 10$ was equivalent to require $N_{pe} > 2$. This is only an approximation, since the effective number of pad hits for a photoelectrons is not a fixed quantity. Following the same approach used to parameterize P_{OFF}, the

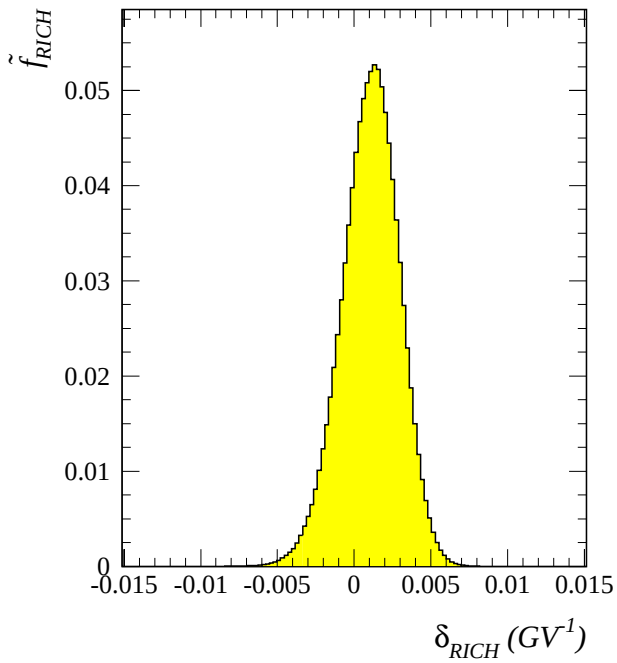

Figure 6.14: *The mean RICH deflection resolution function obtained from the simulation.*

probability P_{10} has been expressed as:

$$P_{10} = \frac{\mathcal{P}(1;N_{pe}) + \mathcal{P}(2;N_{pe})}{1 - \mathcal{P}(0;N_{pe})} = \left(N_{pe} + \frac{N_{pe}^2}{2}\right)\left(e^{-N_{pe}} - 1\right)^{-1} , \tag{6.24}$$

where N_{pe} is given by eq. 6.19, with the correction factor $K(R/R_{th})$ given by:

$$K(R/R_{th}) = \left[1 + \exp\left(\frac{1.03 - R/R_{th}}{1.45}\right)\right]^{-1} . \tag{6.25}$$

Eq. 6.24 expresses the Poisson probability to have 1 or 2 detected photoelectrons when at lest 1 photoelectron is detected and the expected number is N_{pe}. Similarly to the determination of P_{OFF}, the eq. 6.25 has been obtained by fitting experimental data[8]. In eq. 6.25 the maximum number of detected photoelectrons has been set to the ground value to fit the muon data and then scaled to the flight value. The results are shown in fig. 6.13 by the solid and the dashed curve respectively.

The third step of the simulation has been to generate the reconstructed Cherenkov angle. Given the rigidity, the theoretical angle has been calculated taking into account the threshold fluctuation of the Cherenkov threshold due to the refractive index

[8]The parameter values for the correction term $K(R/R_{th})$ are different from those obtained for P_{OFF}. This is not unreasonable, since the arguments discussed in appendix B could have a different effect on the two probabilities.

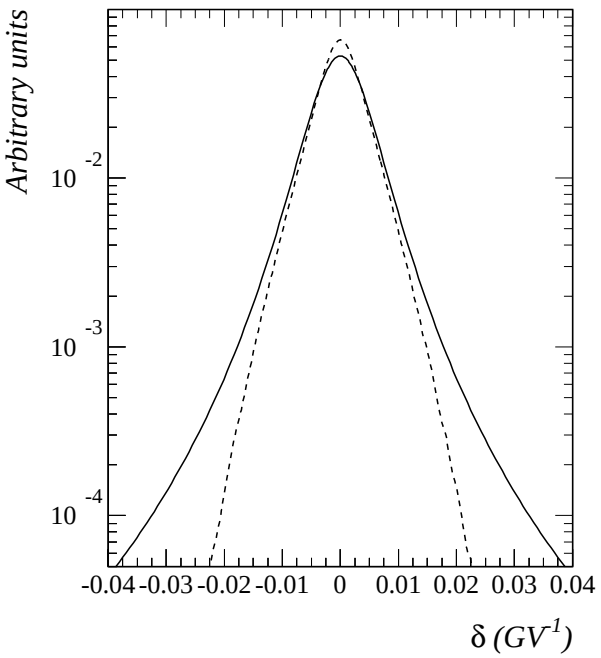

Figure 6.15: *Comparison between the spectrometer resolution function obtained from the unfolding and fitting procedure (solid curve) with those one estimated from the deflection uncertainty given by the fitting routine (dashed curve). In order to have a more clear comparison of the functions the deflection offset is set to zero.*

variation. This has been done by generating event-by-event the refractive index from the experimental distribution. The RICH detector response has then been simulated according to σ_θ and $\Delta\theta_\circ$, obtained from ground muons (see section 6.2.2). The angular resolution is approximately proportional to the inverse of the square root of the effective number of pads used in the Cherenkov angle fitting. Since this variable was changed during the flight, the angular resolution σ_θ was scaled by multiplying for a factor 1.056, obtained from the square root of the ratio between the maximum effective number of pads at ground and in flight.

Finally, the selection requirement on the measured angle has been applied. The resulting mean RICH deflection resolution function is shown in fig. 6.14. Notice that the distribution is not symmetric around the origin. The skewness is due to the non-linear relation between the Cherenkov angle and the deflection. The shift toward positive values is a consequence of the observed shift $\Delta\theta_\circ$ in the reconstructed Cherenkov angle (see fig. 6.3 and eq. 6.13).

6.4.2 The unfolding result

In order to determine the spectrometer resolution function the experimental differential distribution, shown in fig. 6.12, has been fitted with a function obtained convolving the mean RICH resolution function with a Lorentzian function, which parameters have been left free to vary. A variable binning has been chosen in order to have a fine division around the peak, while maintaining enough statistic in every channel. Since the Lorentzian parameters are strongly dependent on the tails of the distribution, where the bins are larger, the data points have been centered using the method suggested by Lafferty & Wyatt [99] . This has required an iteration of the fitting procedure. Furthermore, in order to avoid that the deuteron component altered the result, the left tail of the distribution has been excluded from the fit. The solid curve in fig 6.12 shows the result of the fit ($\chi^2 \sim 1.1$). The resulting best estimate of f^{he}_{spec} is:

$$f^{he}_{spec}(\delta) \propto \left[1 + \left(\frac{2(\delta - 0.3704 \cdot 10^{-3})}{0.15 \cdot 10^{-1}}\right)^2\right]^{-2.1} . \tag{6.26}$$

The center of the Lorentian function, which value resulted to be different from zero, has the physical meaning of an offset in the measured deflection. However the estimated offset value is significantly smaller than the MDR parameter.

Other procedures exists in literature to derive the spectrometer resolution function. A common method [87] is to derive f_{spec} making a superposition of Gaussians with width given by the uncertainty in the measured deflection resulting from the track fitting routine. In fig. 6.15 The function expressed by eq. 6.26 (solid curve) is compared with the estimate obtained by applying the above mentioned method (dashed curve). As can be seen, this method underestimates both the width and the tails of the resolution function. This is mainly due to the Gaussian approximation.

Another approach to the problem is to obtain the resolution function using muons from magnet-off data [78, 79]. In section 6.3.1 it has been shown that the resolution function in this case is affected by the multiple scattering effect (see fig. 6.5), which reduces the spectrometer resolution at low energy. Nevertheless, the high energy resolution function estimate can be improved by requiring a high value of the measured Cherenkov angle in the RICH detector, so to select close to fully relativistic muons. However, our approach has been to do not use this method since it provides an estimate of f^{he}_{spec} that could be still affected by the multiple scattering effect. Moreover,

as discussed in section 6.3.1, the spectrometer performances could have been changed from the magnet-off ground run to the flight run.

6.4.3 Systematic effects

Likewise to P_{OFF}, the resulting uncertainty on the estimate of f_{spec}^{he} have a systematic effect on the final proton background evaluation. The main sources of indetermination, which affect the estimate of f_{spec}^{he}, are enumerated in the following list.

1. The parameterization of σ_θ and $\Delta\theta_\circ$. These two quantities has been used to construct the RICH deflection resolution function f_{RICH} (section 6.4.1).

2. The parameterization of P_{OFF} and P_{10}, obtained from ground muon data. These two quantities, combined with the measured all-particle spectrum, have been used to simulate the rigidity spectrum of the proton, from which the mean RICH detector resolution function $\tilde{f}_{RICH}$ has been obtained.

3. The statistical errors on the parameters of the Lorentian function resulting from the fit.

From fig. 6.11 it can be deduced that the uncertainty on η_{RICH} is significantly smaller than the uncertainty on η_{spec}. From this it follows that any uncertainty on the width of the mean RICH deflection resolution function $\tilde{f}_{RICH}$ has a reduced effect on the width of the resulting spectrometer resolution function. The width of $\tilde{f}_{RICH}$ is related first of all to σ_θ. Beside that, it depends on the rigidity spectrum of the proton sample. Since the uncertainty on η_{RICH} is nearly constant over the considered rigidity range (fig. 6.11), any deviation of the simulated proton spectrum from the real one does not affect significantly the determination of $\tilde{f}_{RICH}$. From these considerations, the sources of indetermination summarized by items 1 and 2 are expected to have a limited effect on the estimate of the width of f_{spec}^{he}.

The last point left is the effect of the uncertainty on the measured shift $\Delta\theta_\circ$ of the reconstructed Cherenkov angle. This directly affect the mean value of $\tilde{f}_{RICH}$ and, as a consequence, the resulting estimate of the offset on the deflection measured with the spectrometer. This systematic effects could explain the small but non negligible offset obtained by fitting the experimental data (see eq. 6.26).

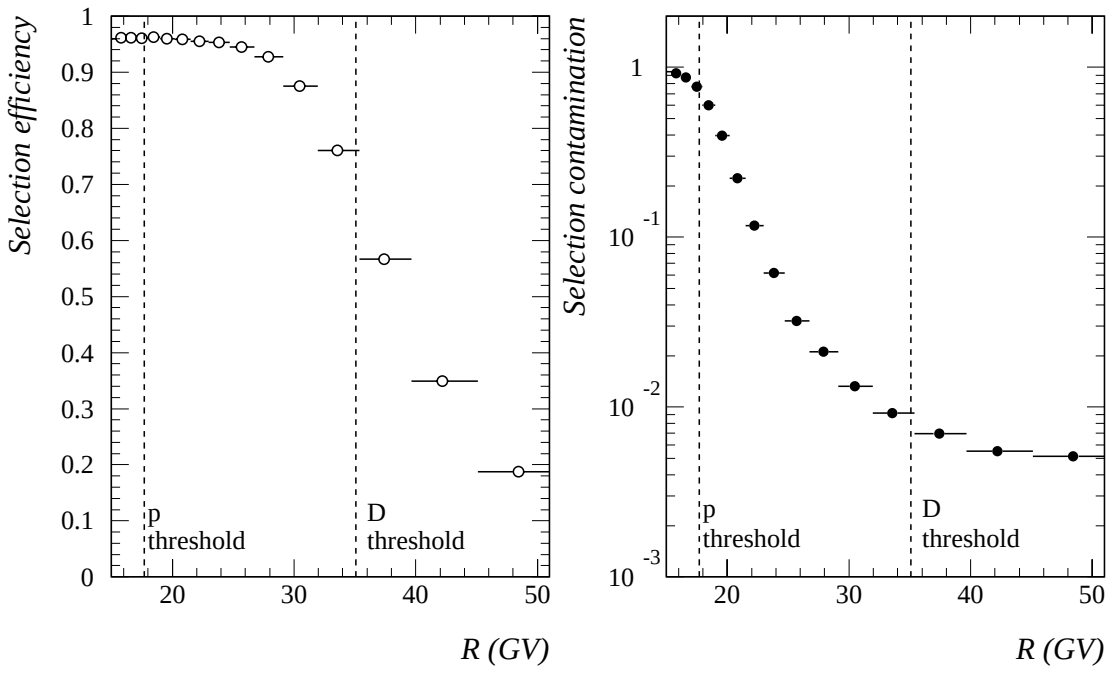

Figure 6.16: *The deuteron selection efficiency (left plot) and the proton contamination (right plot) resulting from the simulation. Dashed lines: proton and deuteron thresholds for Cherenkov light emission.*

6.5 The deuteron selection and proton background simulation

The proton background distribution has been estimated, according to eq. 6.1, with P_{OFF} and f^{he}_{spec} set to the expressions previously presented (equations 6.21-6.21 and 6.26), by means of a simulation. A large sample of protons, with a rigidity spectrum given by eq. 6.23, has been generated. For each generated rigidity value, the probability of zero detected photoelectrons has been calculated according to P_{OFF} and this information has been used to determine if the simulated event had a Cherenkov signal detected. The uncertainty contribution, distributed according to f^{he}_{spec}, has then been added to the generated value. The refractive index variations have been also simulated, by generating the value of n event-by-event from the experimental distribution.

In section 6.1 the instrument response model has been described, limiting the discussion to the necessity of estimating the proton contamination in the deuteron sample.

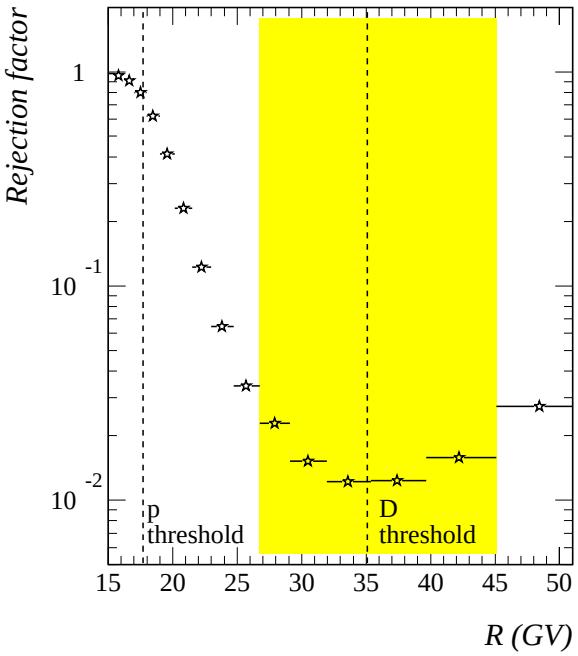

Figure 6.17: *The proton to deuteron rejection factor resulting from the simulation. Dashed lines: proton and deuteron threshold for Cherenkov light emission. Shaded area: rigidity range for the deuteron selection.*

Nevertheless, the same effects that causes the presence of background protons determines the deuteron selection efficiency. A large sample of deuterons has been also generated, following the same procedure applied for protons, but scaling the probability P_{OFF} to the deuteron Cherenkov threshold rigidity.

6.5.1 Selection efficiency and contamination

The fraction of deuterons without a Cherenkov signal in the total deuteron sample gives the selection efficiency (ϵ_{sel}). This quantity is shown in fig. 6.16 (left plot) as a function of the measured rigidity. The same ratio calculated for the generated proton sample gives the contamination level (c_{sel}), which is also shown in 6.16 (right plot).

In order to quantify the deuteron selection capability of the instrument, it is useful to calculate the rejection factor (r_{sel}), defined as the ratio between the contamination and the efficiency[9]. This quantity is plotted in fig. 6.17 as a function of the measured rigidity. Starting from the proton threshold, the rejection factor decreases for increasing rigidity following the trend of the contamination. It reach a minimum around the deuteron threshold, after which it increases again because of the efficiency decrease.

[9]Some authors define the rejection factor as the reciprocal of this value.

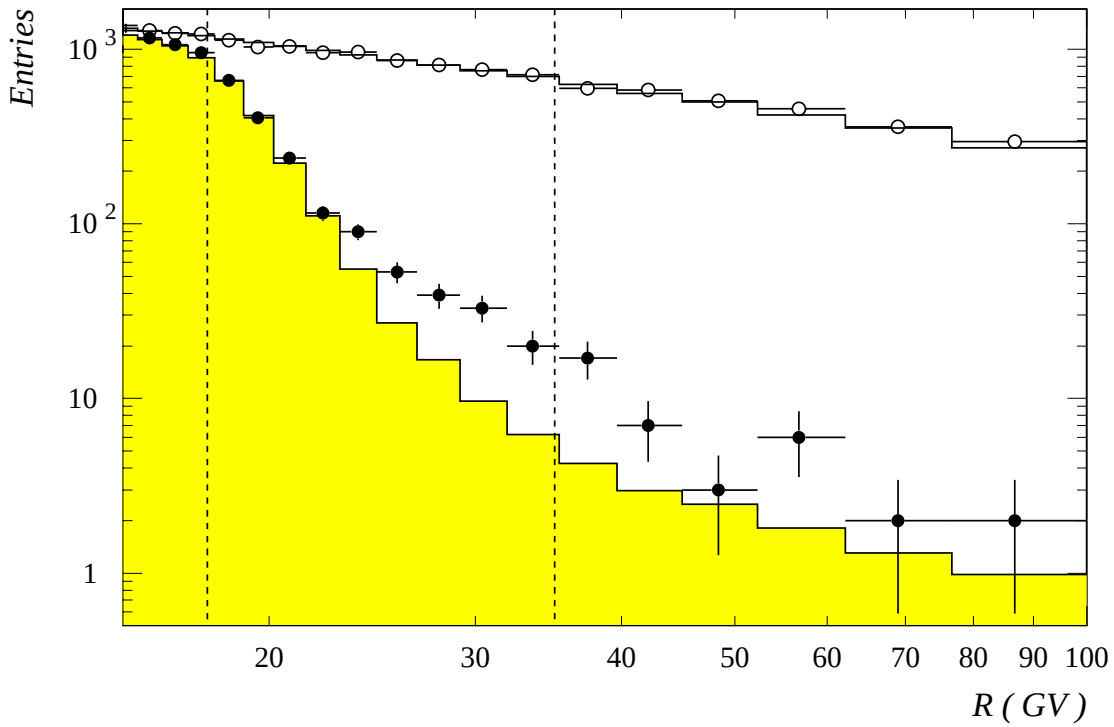

Figure 6.18: *Distributions of the selected events as a function of the measured rigidity compared with the simulated background distribution. The simulated distribution has been normalized to data as described in appendix C. Filled circles: events without a Cherenkov signal. Open circles: all selected events. Dashed lines: proton and deuteron Cherenkov threshold rigidities. Shaded area: simulated background distribution.*

The meaning of the rejection factor is that, given a deuteron to proton ratio equal to D/p, when $r_{sel} = D/p$ the selected sample contains a 50% of background event. Since the minimum value of the rejection factor is $r_{sel} \sim 0.012$, if a contamination level of 50% is accepted, the result of the simulation is that CAPRICE98 is able to identify the deuteron component down to a ratio $D/p \sim 1.2\%$.

6.5.2 The proton and deuteron components

The selection criterion applied to identify the deuterons requires no signal from the RICH detector, above the proton rigidity threshold for Cherenkov light emission (see section 5.4). Given N_{TOT} events satisfying all the basic cuts, after the further requirement of no Cherenkov signal detected the surviving subsample of events N_{OFF} contains

Table 6.3: *The deuteron and proton components, N_D and N_p, in N_{TOT} selected events determined bin-by-bin from the observed number N_{OFF} of events without a Cherenkov signal. In column 4 the estimated number $N_{p,bk}$ of proton background events is shown for comparison with N_{OFF}. The quoted errors are only statistical.*

Rigidity bin (GV)	Selected events		$N_{p,bk} = c_{sel}N_p$	N_p	N_D
	N_{TOT}	N_{OFF}			
$26.7 - 29.1$	813	39	16.67 ± 0.60	788.9 ± 28.4	24.1 ± 6.6
$29.1 - 31.9$	765	33	9.79 ± 0.36	738.5 ± 27.4	26.5 ± 6.4
$31.9 - 35.4$	715	20	6.45 ± 0.25	697.2 ± 26.7	17.8 ± 5.8
$35.4 - 39.7$	597	17	4.00 ± 0.17	574.0 ± 24.6	23.0 ± 7.2
$39.7 - 45.1$	582	7	3.15 ± 0.14	571.0 ± 24.9	11.0 ± 7.6

both protons and deuterons. Fig. 6.18 shows N_{TOT} (open markers) and N_{OFF} (solid markers) as a function of the rigidity over a wide rigidity range. In the same plot the estimated background content is also shown (shaded area).

The comparison shows that the proton background dominates the sample up to ~ 23 GV. For increasing rigidity the deuteron component emerges from the background, resulting in a flattening of the selected event distribution, up to the deuteron rigidity threshold for Cherenkov light emission. Above this value the deuterons radiates too, so that the number of selected events drops again.

The observed quantities N_{TOT} and N_{OFF} are related to the total proton and deuteron components (N_p and N_D) as follows:

$$\begin{cases} N_{TOT} = N_p + N_D \\ N_{OFF} = c_{sel}N_p + \epsilon_{sel}N_D \end{cases} \tag{6.27}$$

The values of N_p and N_D in each rigidity bin have been estimated by solving the linear system 6.27 with c_{sel} and ϵ_{sel} set to the values obtained from the simulation. The results for the significant rigidity bins of the shown distribution (fig. 6.18) are reported in tab. 6.3 (columns 5 and 6) together with the number of selected events (columns 2 and 3).

In column 4 of the same table the calculated proton background content is shown for comparison. A background level of less than 50% of the number of selected events has been accepted, setting the lower rigidity bound for the deuteron selection to 26.7 GV. The rigidity bins above ~ 45 GV have been rejected since the probability for a deuteron to emit Cherenkov light is lower than $\sim 10^3$.

In order to reduce the statistical uncertainty on the final result, N_{TOT} and N_{OFF}

have been grouped in larger bin and the corresponding values of N_D and N_p have been calculated by applying the described procedure. The estimated deuteron component is reported in tab. 6.4 together with the deuteron-to-proton ratio.

The muon contamination

The sample of particles satisfying the basic selection cuts in tab. 5.1 contains, besides protons and deuterons, also relativistic positive muons. The muon-to-proton ratio at balloon altitude is about $\sim 0.3 \cdot 10^{-2}$, at 20 GeV of kinetic energy [100]. At this energy the probability of zero detected photoelectrons is $P_{OFF}(R \gg R_{th}) \sim 0.6 \cdot 10^{-7}$ (equations 6.21 and 6.22). Thus it follows that the positive muon contamination is negligible.

The helium contamination

The charge selection (cut 3 in tab. 5.1) gives also a residual contamination of helium nuclei. If this component is taken into account, the equations 6.27 have to be modified as follows:

$$\begin{cases} N_{TOT} = N_p + N_D + sN_{He} \\ N_{OFF} = c_{sel}N_p + \epsilon_{sel}(N_D + sN_{He}) \end{cases} \tag{6.28}$$

where N_{He} is the number of helium nuclei satisfying all the basic cuts, but cut 3, and s is the charge selection contamination for the helium. From eq. 4.13 it follows that deuterium and helium have nearly the same rigidity threshold for Cherenkov light emission, so that the selection efficiency for the requirement of no Cherenkov signal detected can be assumed to be ϵ_{sel} for both. By comparing the linear system in eq. 6.28 with eq. 6.27, it follows that the calculated number of deuterons N_D, presented in tables 6.3 and 6.4, contains an amount sN_{He} of helium nuclei. The parameterization of the cosmic-ray flux given in section 3.4 gives an helium-to-proton ratio, in the rigidity

Table 6.4: *The estimated number of selected deuterons with the final binning. Both the statistical and the systematic errors are quoted, respectively.*

Rigidity bin (GV)	Number of selected deuterons N_D	Deuteron-to-proton ratio D/p (%)
$26.7 - 31.9$	$50.4 \pm 9.2\,^{+2.5}_{-2.4}$	$3.30 \pm 0.61\,^{+0.17}_{-0.16}$
$31.9 - 45.1$	$53.1 \pm 11.5\,^{+2.6}_{-2.3}$	$2.89 \pm 0.64\,^{+0.13}_{-0.14}$

range taken into consideration, of ~ 0.17. Being the charge selection contamination for helium $s \sim 0.2\%$ (section 5.2), it can be concluded that also the residual helium contamination is negligible.

Statistical uncertainties

In order to estimate the statistical errors of N_p and N_D it has been assumed that the joint probability of the number of events s without a Cherenkov signal in a sample of t selected events was given by

$$p(s,t) = \mathcal{P}(t; N_{TOT})\mathcal{B}(s; t, N_{OFF}/N_{TOT}) \,, \tag{6.29}$$

where $\mathcal{P}$ expresses the Poisson probability of t events when the expected number is N_{TOT} and $\mathcal{B}$ expresses the Binomial probability of s selected events given t trials with probability N_{OFF}/N_{TOT} of success. The errors on c_{sel} and ϵ_{sel} are instead negligible. The variance-covariance matrix of N_p and N_D has been obtained from the variance-covariance matrix of s and t. In tables 6.3 and 6.4 only the square root of the variance is quoted. N_p and N_D have also a non-negligible degree of correlation that has been taken into account in the deuteron-to-proton ratio uncertainty calculation.

Systematic uncertainties

The estimated components of deuterons and protons are also affected by systematic errors due to the uncertainties on both P_{OFF} and f^{he}_{spec}. All these uncertainties, included the statistical ones, have been considered as sources of systematic errors in the estimate of the deuteron component. From the comparison of the listed sources of indetermination (sections 6.3.5 and 6.4.3) it has resulted that the simulation output is mainly affected by the uncertainty on the parameters $P_\circ$ and N^{max}_{pe}. It has been found that all the other sources of indetermination do not affect significantly the results.

In order to evaluate the systematic effect on the estimate of the proton and deuteron component, the simulation code has been run by setting the values of both $P_\circ$ and N^{max}_{pe} to $\pm 1\sigma$ around their best estimate. For each simulated sample, the values of c_{sel} and ϵ_{sel} have been calculated and a new estimate of N_p and N_D has been obtained. The systematic errors quoted in table 6.4 have been calculated as the difference between the new values and the previous ones[10].

[10]The systematic errors related to $P_\circ$ and N^{max}_{pe} have been added.

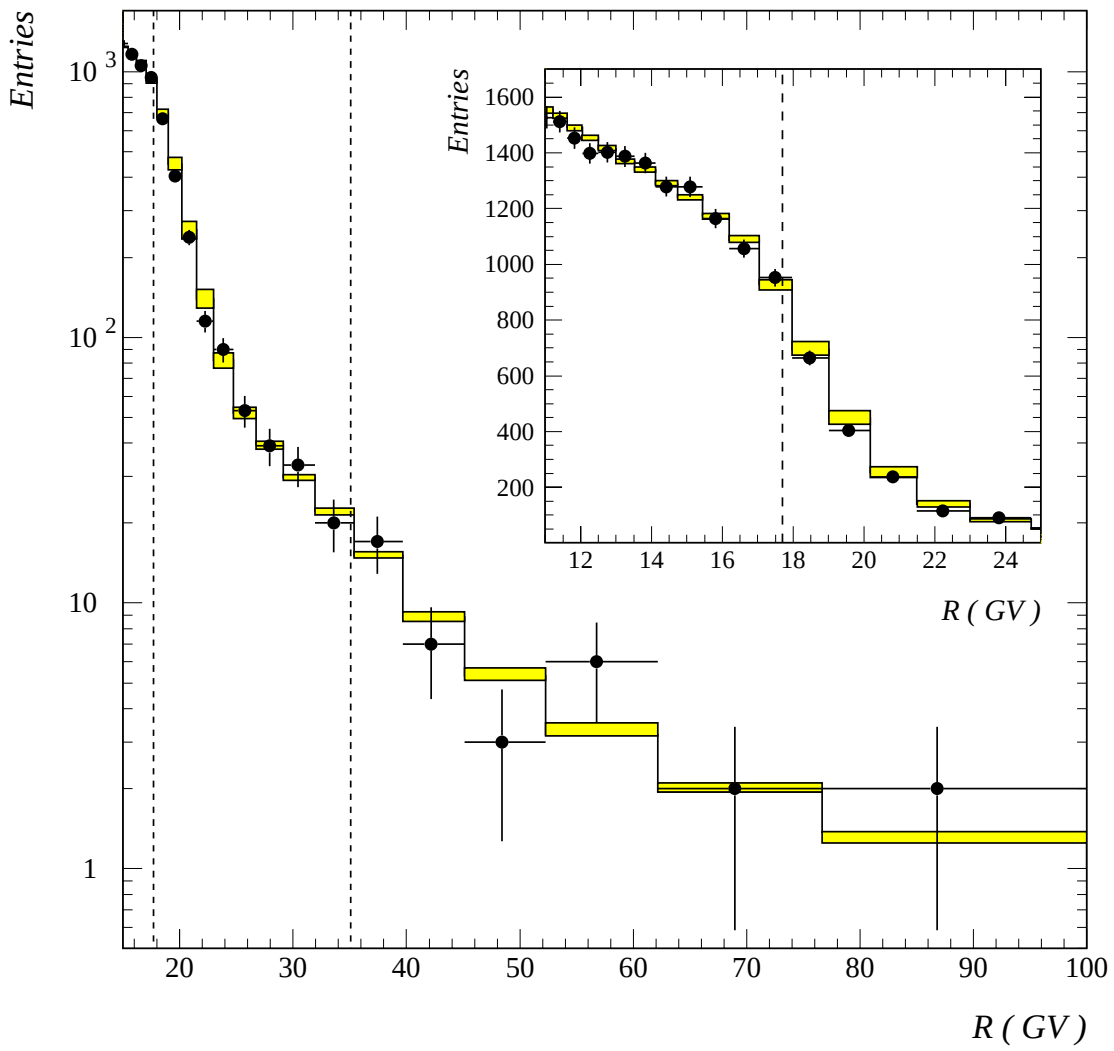

Figure 6.19: *Comparison between the observed distribution of events without a Cherenkov signal and the simulated one obtained including the systematic uncertainties. The simulated distribution has been normalized to data as described in appendix C. The same distribution is shown both in logarithmic and linear scale (inner plot). Filled markers: experimental data. Shaded rectangles: upper and lower systematic bounds of the simulation. Dashed lines: proton and deuteron rigidity threshold for Cherenkov light emission.*

In order to check the reliability of the simulation, the observed distribution of N_{OFF} as a function of the rigidity is compared in fig. 6.19 with the simulation lower and upper bounds obtained by including the systematic uncertainties. The filled markers represent the experimental data, while the shaded rectangles represents the bounds of the simulation output set by the systematic errors. The good agreement between data and simulation indicates that the instrument response model reproduces properly the performances of the detectors. Beside that, the comparison shows that the systematic uncertainties affect the deuteron component estimate by an amount which is anyway lower than the statistical error.

Chapter 7

The deuterium spectrum and the deuterium-to-helium ratio

The aim of the described measurement is to estimate the deuteron component at the top of atmosphere. The results presented at the end of the previous chapter refer instead to the estimated number of deuterons detected in the spectrometer. In order to get the final result these numbers must be corrected for the selection efficiency of the various detectors and for the attenuation and the secondary production due to interactions in the material above the tracking system, including the residual atmosphere. This has been done by solving analytically the deuterium transport equations.

In section 7.1 the corrections necessary to obtain the number of particles at the top of the atmosphere are described. From this quantity both the deuterium flux and the deuterium-to-helium ratio have been obtained. In section 7.2 the results are discussed in comparison with the data from other experiments and theoretical predictions.

7.1 The deuterium at the top of atmosphere

7.1.1 The deuterons in the spectrometer

The first correction to be considered is the detection efficiency. In chapter 5 all the applied selection criteria have been described and the selection efficiencies for each detector estimated. The overall mean selection efficiency in the rigidity range from 20 to 50 GV is $\epsilon = 0.625 \pm 0.009 + 0.012$, where the first error is statistical and the second one comes from the systematic uncertainty on the tracking efficiency (see section 5.2). The number of deuterons corrected for the detection efficiency are presented in tab. 7.1, together with the statistical and systematic errors, including the one-

sided bound coming from the tracking system systematic uncertainty[1]. The number of selected deuterons, after the correction for the detection efficiency, gives the number of deuterons entering the spectrometer (N_D^{Sp}) and satisfying the applied geometrical conditions.

Table 7.1: *Number of deuterons entering the spectrometer. The presented uncertainties are respectively the statistical error, the systematic error from the simulation and the systematic error from the tracking efficiency.*

Rigidity bin (GV)	Number of deuterons N_D^{Sp}
$26.7 - 31.9$	$80.7 \pm 14.8\ ^{+4.0}_{-3.8} - 1.5$
$29.1 - 45.1$	$85.0 \pm 18.5\ ^{+4.2}_{-3.7} - 1.6$

7.1.2 Secondary production and attenuation corrections

To reach the tracking system the particles had to go through the residual atmosphere above the payload and through the payload material above the spectrometer. This resulted in particle losses and productions due to interactions, which have to be taken into account in order to estimate the number of deuterons at the top of atmosphere. Such effects have been accounted for by solving analytically a simplified version of the transport equation for deuterons (eq. 3.19).

The simplified transport equations

From the discussion about the atmospheric deuteron production in section 3.2.2, it follows that at high energy both the ionization energy loss and the secondary production due to the air nuclei fragmentation are negligible. The main secondary production contribution comes from the spallation of He and HN, which leads to the production of fragments mainly in the forward direction and with the same energy per nucleon of the projectiles. As a consequence, eq. 3.19 simplifies as follows:

$$\frac{\partial J_D(E,\theta,x)}{\partial l} = -\frac{J_D(E,\theta,x)}{\lambda'_D(E)} + \frac{J_{He}(E,\theta,x)}{\lambda_{He\to D}(E)} + \frac{J_{HN}(E,\theta,x)}{\lambda_{HN\to D}(E)}\,, \qquad (7.1)$$

[1]The systematic uncertainties have been treated as lower and upper bounds on the estimated number of deuterons N_D. In order to propagate them, all the described corrections have been applied to the extreme values of N_D, set by the systematic errors. The presented systematic uncertainties represent the difference between the obtained values and the best estimate.

where J_i, with i =D,He,HN are the deuteron, helium and heavy nuclei fluxes as a function of the kinetic energy per nucleon. Similar equations hold for He and HN, with the differences that the HN equation includes only the attenuation term and the He equation has also a production term, describing the spallation of HN. The system of equations can be solved analytically and the solution for the deuterium flux, as a function of the depth x, is:

$$J_D(E,\theta,x) = J_D^{ToA}(E)\, e^{-\frac{x}{\lambda'_D \cos\theta}} + \sum_{n=He,HN} J_n^{ToA}(E)\, \sigma_{n\to D} \left[\frac{e^{-\frac{x}{\lambda'_n \cos\theta}} - e^{-\frac{x}{\lambda'_D \cos\theta}}}{\sigma'_D - \sigma'_n} \right] . \tag{7.2}$$

In eq. 7.2 J_i^{ToA} $(i = D, He, HN)$ is the isotropic flux at the top of atmosphere (primary flux). The first term on the right hand side of eq. 7.2 describes the attenuation of the primary deuterium flux. The second term describe the secondary deuteron production from the spallation of He and HN; these terms are proportional to the corresponding fragmentation cross-section and to a further term, between squared brackets, which takes into account the fluxes attenuation. The deuterium flux at the top of the payload is given by:

$$J_D^{ToP}(E,\theta) = J_D^{ToA}(E)\, e^{-\frac{A_D}{\cos\theta}} + \sum_{n=He,HN} J_n^{ToA}(E)\, \frac{\sigma_{n\to D}}{\sigma'_D - \sigma'_n} \left[e^{-\frac{A_n}{\cos\theta}} - e^{-\frac{A_D}{\cos\theta}} \right] , \tag{7.3}$$

where

$$A_i \equiv \frac{x_{air}}{\lambda'_{i,air}} \quad i = D, He, HN. \tag{7.4}$$

In eq. 7.4 x_{air} is the atmospheric depth and $\lambda'_{i,air}$ is the total interaction length, so that A_i expresses the thickness of traversed atmosphere in units of interaction lengths for the nucleus of type i. From eq. 7.3 the deuterium flux at the top of the payload is derived, taking into account both the secondary deuterium production and the primary deuterium attenuation.

In order to reach the spectrometer, the deuterium had to further traverse the material layers above the tracking system. It has been assumed that all the particles which had interacted above the tracking system were rejected by the selection criteria. As a consequence, from the top of the payload down to the tracking system, the variation of

the deuterium flux is described by the attenuation term only. The flux in the spectrometer (J_D^{Sp}) is given by eq. 7.3 multiplied by the attenuation factor $\exp[-x/(\lambda'_{D,air} cos\theta)]$, so that we have:

$$J_D^{Sp}(E,\theta) = J_D^{ToA}(E)\, e^{-\frac{M_D+A_D}{\cos\theta}} + \sum_{n=He,HN} J_n^{ToA}(E)\, \frac{\sigma_{n\to D}}{\sigma'_D - \sigma'_n} \left[e^{-\frac{M_D+A_n}{\cos\theta}} - e^{-\frac{M_D+A_D}{\cos\theta}} \right] , \quad (7.5)$$

where

$$M_D \equiv \sum_j \frac{x_j}{\lambda'_{D,j}}. \quad (7.6)$$

In eq. 7.6, where the notation is the same one used in eq. 7.4, the summation is carried out over all the traversed layers of different materials in the payload above the spectrometer, so that M_D represents the total thickness of material that the deuterons had to go through, in units of interaction length. Notice that, while J_D^{ToA} is isotropic, J_D^{Sp} depends on the azimuth angle θ. This is a consequence of the different amount of material traversed by the particles in any direction.

To obtain the number of deuterons entering the spectrometer $N_D^{Sp}(E)dE$, in a kinetic energy range between E and $E + dE$, eq. 7.5 has to be integrated over the detector field of view. If a simple geometry is assumed, given by a detector surface $S_\circ$ with an angular aperture corresponding to a solid angle $\Omega_\circ$ (so that $GF \sim S_\circ \Omega_\circ$), we have:

$$N_D^{Sp}(E)dE = S_\circ \left(\int_{\Omega_\circ} J_D^{Sp}(E,\theta) d\Omega \right) dE \, . \quad (7.7)$$

If we take into account the fact that

$$N_D^{ToA}(E)dE = 2\pi S_\circ (1 - \cos\theta_\circ) J_D^{ToA}(E)dE \, , \quad (7.8)$$

from eq. 7.5 it follows:

$$N_D^{Sp}(E) = \frac{N_D^{ToA}(E)}{(1-\cos\theta_\circ)} \int_0^{\theta_\circ} e^{-\frac{M_D+A_D}{\cos\theta}} \sin\theta d\theta + \sum_{n=He,HN} \frac{N_n^{ToA}(E)}{(1-\cos\theta_\circ)} \frac{\sigma_{n\to D}}{\sigma'_D - \sigma'_n} \left[\int_0^{\theta_\circ} \left(e^{-\frac{M_D+A_n}{\cos\theta}} - e^{-\frac{M_D+A_D}{\cos\theta}} \right) \sin\theta d\theta \right] . \quad (7.9)$$

Equations 7.8 and 7.9 have been obtained by expressing the angular aperture of the detector in a polar reference system with the axis in the zenith direction, so that

Table 7.2: *Material that a particle had to go through to reach the tracking system.*

	Material	Atomic weight	Thickness (g/cm^2)
Atmosphere	$N_2(80\%)\ O_2(20\%)$	14.4	5.5
Dome	Al	26.98	0.81
Gondola gas	N_2	14.01	0.03
RICH cover	Al	26.98	0.14
Pad plane	G10	17.75	1.02
Window	Quartz	21.65	1.16
Radiator	C_4F_{10}	17.59	1.02
Mirror	Quartz	21.65	1.39
RICH box	Al	26.98	0.42
Scintillator	Plastic	11.16	1.05

$\Omega_\circ = 2\pi(1 - \cos\theta_\circ)$. The integral in eq. 7.9 has an analytical solution which can be found in the integral tables. Equations similar to eq. 7.9 hold for He and HN.

The result of the calculation described above is that, if data are expressed in bins of kinetic energy per nucleon, the number of particles N_i^{Sp} entering the spectrometer is related to the number of particles N_i^{ToA} at the top of atmosphere through a system of linear equations. In particular, only three nuclear components ($i = D, He, HN$) are necessary to describe the deuterium propagation, resulting in a system of three equations. The coefficients of the system depend on the amount of traversed material, included the residual atmosphere, on the geometrical acceptance of the detector and on the cross-sections. Once the coefficients are known, the unknown number of particles at the top of atmosphere N_i^{ToA} can be expressed as a function of the observed number of particles entering the spectrometer N_i^{Sp}.

Corrections for the CAPRICE98 configuration

The CAPRICE98 experiment was performed at an average atmospheric depth of 5.5 g cm^{-2}, which correspond to $A_D \sim 0.111$ interaction lengths. The needed partial cross-section values are those given in section 3.3.2 and appendix A.

The material above the tracking system in the CAPRICE98 configuration is summarized in table 7.2, where both the mean atomic weight and the thickness in g/cm^2 of each layer are reported. The traversed material included the aluminum shell of the payload , the whole RICH detector and the top scintillator of the TOF system. The

probability of an interaction in the drift chamber material has been considered negligible. The corresponding interaction lengths have been estimated by scaling to the proper atomic weight, as described in section 3.3.1 and appendix A. The resulting total thickness in units of interaction length is $M_D \sim 0.137$.

The field of view of the apparatus is essentially determined by the geometrical condition for the containment of the Cherenkov ring inside the pad plane (cut 12 in tab. 5.1), which limits the arrival direction of the detectable particles to a maximum zenith angle of $\theta_\circ \sim 12^\circ$.

The heavy nuclei contribution has been treated by assuming $N_{HN}^{ToA} = f N_{He}^{ToA}$, where f has been estimated, for each kinetic energy bin, from the flux parameterizations described in section 3.4, as the ratio between the HN and the He fluxes. The system of equations has then been solved and the unknown quantities N_D^{ToA} and N_{He}^{ToA} have been expressed as a function of the observed quantities N_D^{Sp} and N_{He}^{Sp} for each kinetic energy bin[2].

Table 7.3: *Variation of the number of deuterons and helium nuclei from the top of the atmosphere down to the spectrometer. The atmospheric contributions are divided in primary (p) and secondary (s).*

Kinetic energy bin (GeV/n)	Particles in the spectrometer		Particles at the top of the payload					Particles at the top of atmosphere	
			N_D^{ToP}			N_{He}^{ToP}			
	N_D^{Sp}	N_{He}^{Sp}	p	s(He)	s(HN)	p	s(HN)	N_D^{ToA}	N_{He}^{ToA}
$12.47 - 15.06$	80.7	385.5	78.9	9.6	4.2	434.1	5.2	88.2	486.2
$15.06 - 21.63$	85.0	490.7	80.0	12.2	5.4	552.5	6.7	89.5	618.8

The estimated number of particles at the top of the atmosphere is presented in tab. 7.3. In the same table the number of particles at the top of the payload is also shown. For a given particle type, both the primary (denoted with p) and the secondary component (denoted with s), resulting from the spallation of heavier nuclei, are indicated. These values were obtained by propagating the number of particles from the top of the atmosphere. From the results presented in tab. 7.3 it follows that the number of deuterons increases for increasing atmospheric depth: after traversing the

[2]The helium has been selected by applying the analysis procedure described in [81]. The number of helium nuclei N_{He}^{Sp} entering the spectrometer has been estimated by scaling to the geometrical factor for the deuteron selection.

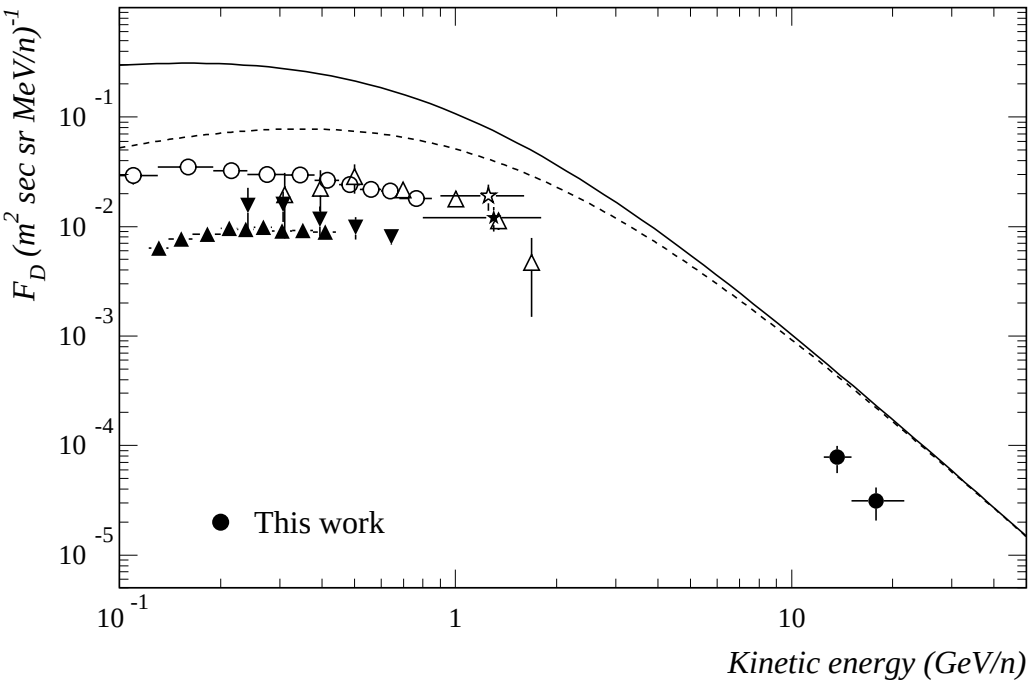

Figure 7.1: *The cosmic-ray deuterium flux. Filled circles: CAPRICE98 result. Other symbols: results from other experiments (see tab. 7.6 for references). Solid and dashed curves: primary helium flux at minimum and maximum solar modulation level, respectively.*

residual atmosphere the number of secondaries is about 20% of the attenuated primary component. The overall correction on the number of deuterons in the spectrometer amounts to about 7%.

The resulting estimates of N_D^{ToA} and N_{He}^{ToA} are presented also in tab. 7.4, together with the uncertainties.

Table 7.4: *Estimated number of deuterons and helium nuclei at the top of atmosphere.*

Kinetic energy bin (GeV/n)	Number of deuterons N_D^{ToA}	Number of helium nuclei N_{He}^{ToA}
$12.47 - 15.06$	$88.2 \pm 19.0\ ^{+5.1}_{-4.9} - 1.9$	486.2 ± 31.6
$15.06 - 21.63$	$89.5 \pm 23.8\ ^{+5.3}_{-4.8} - 2.0$	618.8 ± 35.6

7.1.3 The deuterium-to-helium ratio and the deuterium flux

The deuterium-to-helium ratio at the top of the atmosphere has been obtained from the ratio between the values of N_D^{ToA} and N_{He}^{ToA} presented in tab. 7.4. The results are shown in column 2 of tab. 7.5.

The deuterium flux has been calculated according to:

$$F_D^{ToA}(E) = \frac{N_D^{ToA}}{T_{live} \cdot GF \cdot \Delta E} \,, \tag{7.10}$$

where T_{live} is the live time of the experiment (see eq. 4.18), GF is the geometrical factor (see tab. 5.2) and ΔE is the width of kinetic energy bin. The resulting values are presented in column 3 of tab. 7.5. In column 1 of tab. 7.5 we reported the center of each kinetic energy bin, calculated as the center-of-gravity of the bin.

Table 7.5: *D/He ratio and deuterium flux at the top of the atmosphere.*

Mean kinetic energy (GeV/n)	Deuterium-to-helium ratio D/He	Deuterium flux F_D^{ToA} $(\mathrm{m^2\ s\ sr\ GeV/n})^{-1}$
13.66	$0.181 \pm 0.036\ ^{+0.011}_{-0.010} - 0.004$	$(7.8 \pm 1.6\ ^{+0.5}_{-0.4} - 0.2) \times 10^{-2}$
17.80	$0.145 \pm 0.034\ ^{+0.021}_{-0.008} - 0.008$	$(3.13 \pm 0.83\ ^{+0.19}_{-0.17} - 0.07) \times 10^{-2}$

Reference	Year	Symbol
Apparao [6]	1973	❋
Bogomolov *et al.*[7]	1979	☆
Webber *et al.* [10]	1989*	▲
Papini [11]	1989*	▼
Bogomolov *et al.*[8]	1990*	★
Finetti [12]	1994	△
Lamanna [13]	1998	○

Table 7.6: *Deuterium measurement reference list. Column 2 indicates the year when each experiment was carried out. The symbol * indicates the measurements performed during maximum solar modulation level.*

7.2 Comparison between theoretical and experimental data

Fig. 7.1 shows the deuterium flux measured by CAPRICE98[3], compared with the results given by other experiments (see section 2.1). The reference list for the reported

[3]The presented error bars have been obtained by adding the systematic uncertainties to the statistical errors.

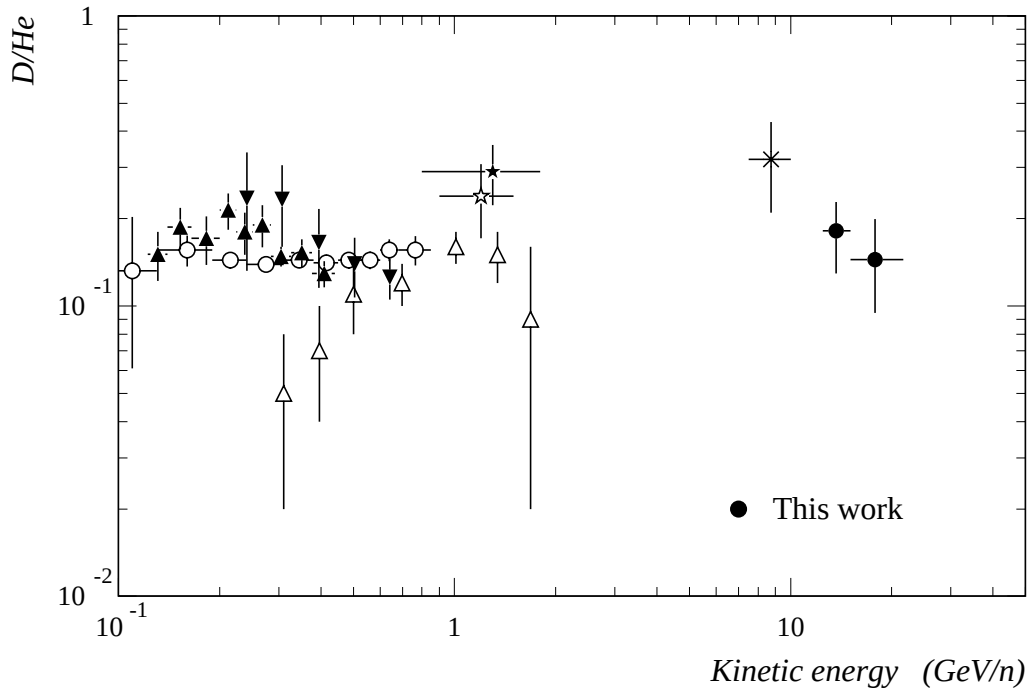

Figure 7.2: *D/He ratio. Filled circles: CAPRICE98 result. Other symbols: results from other experiments (see tab. 7.6 for references).*

data is presented in tab. 7.6, together with the year when each experiment was carried out. In the same plot the helium flux, both at minimum (solid curve) and maximum (dashed curve) solar modulation level, is also shown for comparison, as resulting from the parameterization given in section 3.4. One can notice that the CAPRICE98 measurement represents the first result on the deuterium flux obtained at energies above 2 GeV/n. All the other published results cover an energy range which is affected by solar modulation. The observed differences among the measurements are in fact consistent with the solar activity indicated by the Climax neutron monitor (fig. 3.4).

As discussed in chapter 2, at high energy the deuterium is mainly a product of the nuclear interactions of primary cosmic-ray helium in the interstellar medium. The deuterium-to-helium ratio (D/He) is thus a meaningful quantity to study the interstellar propagation mechanism. Fig. 7.2 shows the CAPRICE98 result, compared with those given by other experiments. Only one measurement exists above 2 GeV/n, which is consistent, within the experimental errors, with the CAPRICE98 result. The whole data suggest that the D/He ratio does not depend significantly on the energy, over the

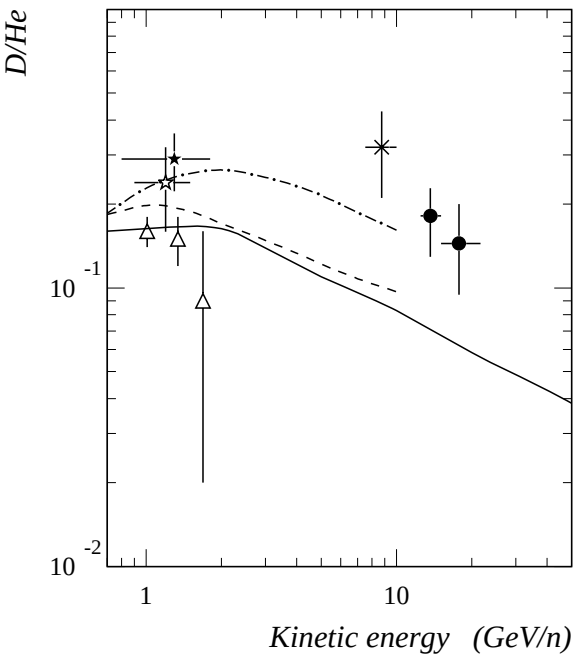

Figure 7.3: *Theoretical predictions for the D/He ratio, resulting from three different calculations within the framework of the LBM. Filled circles: CAPRICE98 result. Other symbols: results from other experiments (see tab. 7.6 for references). Solid curves: Stephens [19]. Dashed curves: Webber [21]. Dotted-dashed curve: Mewaldt [20].*

energy range from 100 MeV/n to several tens of GeV/n.

To interpret the experimental observations below ~ 1 GeV/n, assumptions on both the solar modulation and the interstellar propagation are necessary. Since the two effects are not clearly separable, low energy data provide limited informations concerning the propagation mechanisms through the interstellar medium. Above ~ 1 GeV/n the solar modulation effects are instead small, so that measurements of the secondary abundances above this energy are useful tools to test propagation models.

In fig. 7.3 the high energy measurements of the D/He ratio are compared with the theoretical predictions, obtained on the basis of some standard models formulated within the framework of the *Leaky-Box Model* (LBM). The details of these models have been discussed in section 2.2.1. The general agreement is that cosmic-ray hydrogen and helium have the same propagation history of heavier cosmic-ray nuclei. The standard propagation models for H and He assumes in fact the same amount of matter traversed within the Galaxy as deduced from the study of the most abundant heavier secondary cosmic-ray nuclei. According to this assumption the secondary-to-primary ratio should decrease at high energy, following the observed decrease with energy of the escape mean free path from the Galaxy. However, from fig. 7.3 it is inferable that, even within the

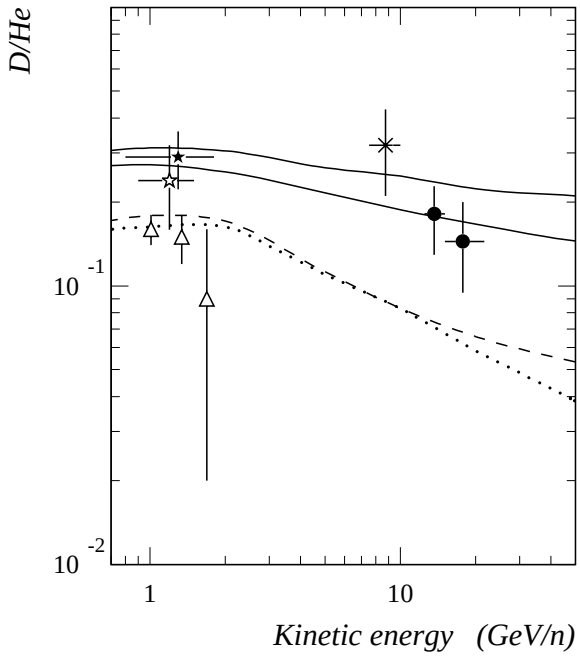

Figure 7.4: *Theoretical predictions for the D/He ratio from the calculation of Stephens [19], on the basis of some non-standard models. Filled circles: CAPRICE98 result. Other symbols: results from other experiments (see tab. 7.6 for the references). Upper solid curve: CGM calculation. Lower solid curve: TSM calculation. Dashed curve: NLBM calculation. Dotted curve: LBM calculation.*

same standard scenario, different calculations give results that differ by large amounts. The experimental data suggest a better agreement with the Mewaldt [20] (dotted-dashed curve) result, which predicts a ratio D/He at 10 GeV/n which is about a factor 2 grater than the value predicted by the calculation of Stephens [19] (solid curve).

In reference [19] the author presents also results concerning some non-standard models: the *Nested Leaky Box Model* ($NLBM$), the *Closed Galaxy Model* (CGM) and the *Thick Source Model* (TSM), described in section 2.2.2. The comparison with these theoretical predictions is shown in fig. 7.4. The $NLBM$ predicts a deuterium-to-helium ratio similar to that obtained from the LBM. The CGM and the TSM assume a large amount of matter to be traversed by cosmic rays before the escape from the Galaxy, which results in a larger abundances of light secondaries, if compared with that predicted by standard models. By comparing data with the Stephens [19] predictions, the CGM and the TSM are better supported than standard models.

7.2.1 Conclusions

From the discussion above one can conclude that the scenario is still unclear. This is due both to the paucity of results concerning the light isotope abundances at high energy

and to the uncertainties on propagation parameters, which lead to disagreements even within the same model. Notice however that, as discussed in section 1.3, the light nuclei abundances provide more significant informations, about the propagation mechanism through the Galaxy, than the heavier nuclei, being their interaction mean free path considerably longer than the escape mean free path. The new results given by the CAPRICE98 experiment, concerning both the deuterium flux and the ratio D/He, provide useful tools to test propagation models for the cosmic-ray helium. We thus aim to stimulate new theoretical studies and experimental measurements concerning this important subject.

Appendix A

Cross-section compilation

Total interaction cross-sections

The present compilation of total interaction cross-sections includes the available data for deuterium, ^{3}He, ^{4}He and ^{12}C projectiles on carbon target, above 100 MeV/n of projectile kinetic energy. Tab. A.1 shows the collected cross-section values, together with the corresponding references. These same values are plotted in fig. 3.1 as a function of the projectile energy.

Table A.1: *Total interaction cross-section reference list, for carbon target. Open symbols refer to results from track-chamber experiments, while filled symbols refer to counter experiment [37].*

Reference and symbol	Kinetic energy (GeV/n)	$\sigma'(mb)$		
		D projectile	^{4}He projectile	^{12}C projectile
[47] ▲	0.08	-	-	965 ± 30
[47] ▲	0.20	-	-	864 ± 45
[47] ▲	0.25	-	-	873 ± 60
[47] ▲	0.30	-	-	858 ± 60
[46] ★	0.79	-	503 ± 5	-
[42] ●	0.87	411 ± 21	527 ± 26	939 ± 49
[44] ☆	1.	459 ± 19	-	-
[43] ○	1.	425 ± 21	-	-
[41] ▼	2.1	-	-	826 ± 23
[42] ●	2.1	426 ± 22	535 ± 27	888 ± 50
[37] △	3.4	380 ± 20	440 ± 20	790 ± 50
[38] □	3.7	-	450 ± 20	780 ± 30
[39] □	3.7	-	410 ± 25	-
[40] ■	3.7	-	529 ± 11	-
[45] ◊	4.2	400 ± 20	450 ± 20	830 ± 50

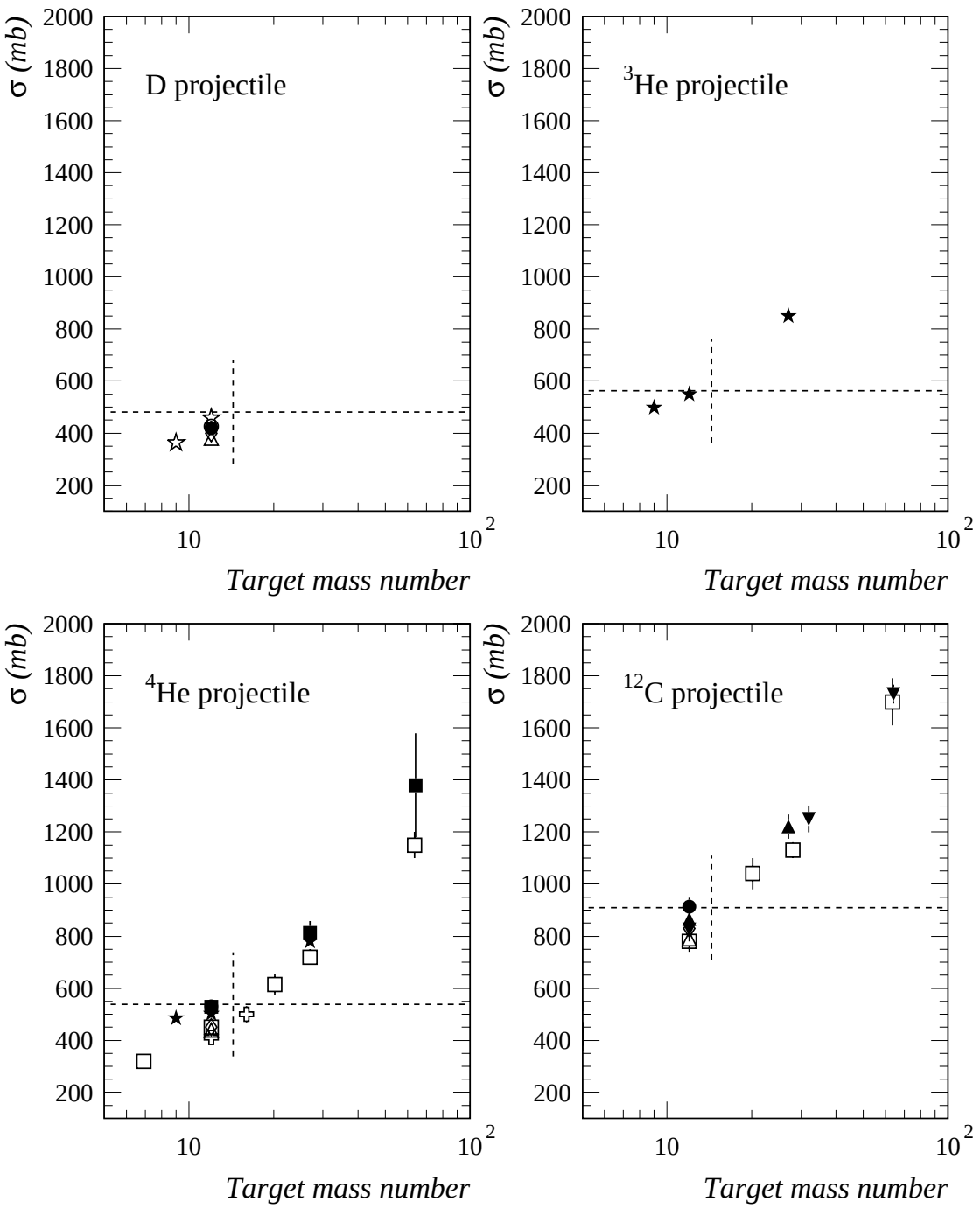

Figure A.1: *Total interaction cross-sections for deuterium, ^{3}He, ^{4}He and ^{12}C projectiles as a function of the target mass number. Symbols: experimental data (see reference list in tab. A.1). Dashed lines: estimated total interaction cross-sections for air target.*

Some authors, included in the compilation, present also results for target nuclei different from carbon. Fig. A.1 shows the total interaction cross-section for deuterium, ^{3}He, ^{4}He and ^{12}C projectiles as a function of the target mass number. For those works presenting results at different projectile energies the average value has been plotted. In the same figure the estimated cross-section values for air target are shown by horizontal dashed lines. The general rule applied to to scale the cross-sections to air target has been to consider the cross-section values, from the same references, for two different reactions, as similar as possible to that one with air nuclei, and evaluate the parameter y in eq. 3.19 from the ration between the corresponding cross-sections.

Partial fragmentation cross-sections

The present compilation of partial fragmentation cross-sections includes the available data for ^{4}He projectile on hydrogen target, as well as ^{4}He and ^{12}C projectiles on carbon target, above 100 MeV/n of projectile kinetic energy.

Tab. A.2 shows the inclusive cross-sections for the production of deuterium, ^{3}H and ^{3}He from the fragmentation of ^{4}He projectile on hydrogen target, together with the corresponding references. These values are those shown in fig. 3.3 as a function of the projectile kinetic energy.

Table A.2: *Partial fragmentation cross-sections reference list, for ^{4}He projectile on hydrogen target.*

Reference and symbol	Kinetic energy (GeV/n)	$\sigma_{^4\text{He}\rightarrow\text{fragment}}$ (mb)		
		D fragment	^{3}H fragment	^{3}He fragment
[52] ★	0.15	24.0 ± 2	29 ± 3	-
[54] ▲	0.22	30.2 ± 1.0	20.7 ± 0.7	34.6 ± 1.1
[52] ★	0.20	13.6 ± 1	28.3 ± 3	28.3 ± 3
[52] ★	0.38	12.6 ± 2	26.3 ± 3	26.3 ± 3
[52] ★	0.52	-	-	26.4 ± 3
[55] ◇	0.63	32.1 ± 1.1	20.9 ± 0.8	23.5 ± 0.8
[56] ▼	1.	-	24.1 ± 1.9	-
[53] ●	1.41	31.35 ± 0.3	28.59 ± 0.3	24.87 ± 0.3
[53] ●	2.59	25.95 ± 0.1	23.89 ± 0.3	23.66 ± 0.3

The partial fragmentation cross-sections for ^{4}He and ^{12}C projectiles on carbon target have been obtained from references [57, 51], respectively (see tab. 3.1). These same

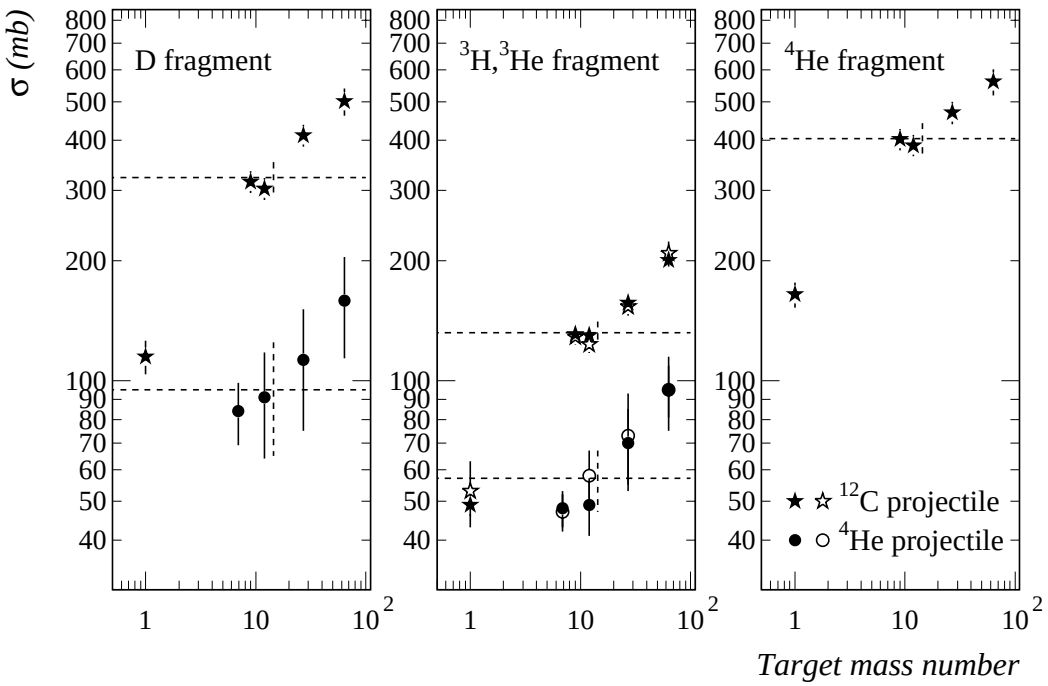

Figure A.2: *Partial fragmentation cross-sections for ^{4}He and ^{12}C projectiles as a function of the target mass number. Stars: experimental data for ^{12}C projectiles. Circles: experimental data for ^{4}He projectiles. Open and filled symbols in the central frame: ^{3}H and ^{3}He fragment results respectively. Dashed lines: estimated partial fragmentation cross-sections for air target.*

authors present results for target nuclei different from carbon. Fig. A.2 shows the inclusive cross-sections for the production of deuterium, ^{3}H, ^{3}He and ^{4}He fragments, from ^{4}He (circles) and ^{12}C (stars), as a function of the target mass number. The results from reference [51] have been averaged over the energy. The ^{3}H and ^{3}He results are shown in the same frame by open and filled symbols respectively. Notice that the inclusive cross-section is the same for ^{3}H and ^{3}He fragment production, within the experimental errors. These data have been used to scale the cross-section values from carbon to air target, as discussed above. The obtained values are presented in tab. 3.2 and are shown by horizontal dashed lines in fig. A.2.

Appendix B

The RICH MWPC detection efficiency

The probability of zero detected photoelectron has been evaluated using ground muons, selected requiring $N_{eff} = 0$ (see section 6.3). Theoretically we would expect this probability to be described by the Poisson probability of zero detected photoelectrons when the expected number is N_{pe}:

$$P_{OFF}(R/R_{th}) = P_{\circ}\, e^{-N_{pe}(R/R_{th})}\,, \tag{B.1}$$

where N_{pe} is rigidity dependent according to eq. 4.12, which is obtained within the framework of the Cherenkov theory. However, in section 6.3.3, we have pointed out that eq. B.1 is not adequate to describe data. Instead they are well reproduced through the relation:

$$P_{OFF}(R/R_{th}) = P_{\circ}\, e^{-N_{pe}(R/R_{th})K(R/R_{th})}\,, \tag{B.2}$$

where $K(R/R_{th})$ (eq. 6.20) is an empirical factor, obtained by fitting experimental data, that increases for increasing rigidity up to an asymptotic value of 1. The empirical factor K can be interpreted as if the photoelectron detection efficiency near the Cherenkov threshold rigidity is lower than the efficiency for relativistic particles, when the Cherenkov angle reach its maximum value. The resulting effect is that the probability of zero detected photoelectron, near the Cherenkov threshold rigidity, is greater than the value expected from eq. B.1.

The only process, starting from the emission of the Cherenkov light to the production of a detectable signal, that can account for this behavior is the photoelectron detection in the MWPC. A characteristic of the MWPC working which could justify

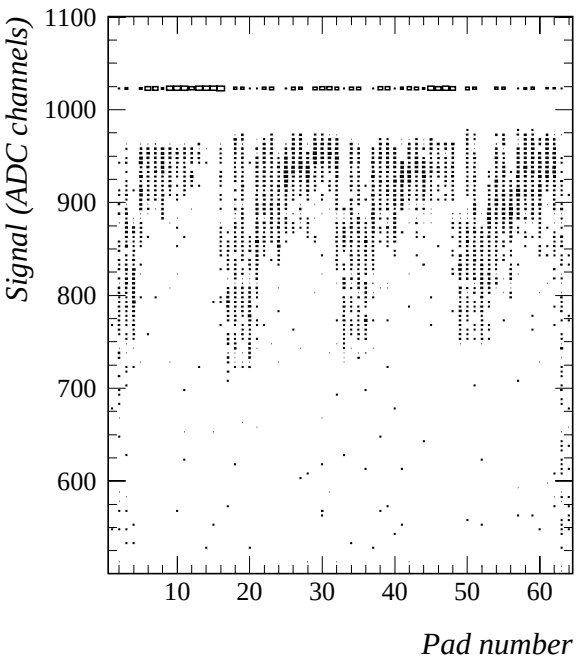

Figure B.1: *Distribution of the greatest signal in the ionization cluster as a function of the pad number along the x direction (in the payload reference system). The plot refers to a restricted area of the pad plane.*

what we observe is a non uniform response of the detector. In fact, let be assumed that the MWPC efficiency is not homogeneous but there are some regions where it is lower than the average value. Let be considered a particle with rigidity greater than the rigidity threshold for Cherenkov light emission, and let be supposed that some photons are converted in the MWPC. The probability to detect a Cherenkov signal for the event is related to the MWPC efficiency along the Cherenkov ring. If the diameter of the minimum detectable ring is greater than the spatial dimensions over which the detector response varies, an effective efficiency can be defined as the MWPC efficiency averaged over the sensor plane, which results in N_{pe}^{max} detected photoelectrons for relativistic particles. This value does not depends neither on the ring size nor on its position inside the pad plane, so that the probability P_{OFF} can be described by eq. B.1. If instead the ring diameter is of the same order of magnitude of the mentioned structures or lower, the situation is more complicate. For example, it can happen that the Cherenkov ring is entirely contained inside a region of low (or of high) efficiency. In this case eq. B.1 is no more adequate to describe the resulting overall probability of no Cherenkov signal detected.

In order to understand how this effect can account for an increase of the probability

P_{OFF} in comparison with the value expected from eq. B.1, it is useful to refer to a simple model. Let be supposed that the sensor plane is divided into regions of two kinds only, whose photoelectron detection efficiencies are ϵ_l (low efficiency) and ϵ_h (high efficiency) respectively. Furthermore, let be supposed that the relative extensions of the two regions are r_l and r_h ($r_l + r_h = 1$), and d is the spatial dimension of the structures. The mean effective efficiency ($\tilde{\epsilon}$) of the detector is obtained by averaging over the sensor plane: $\tilde{\epsilon} = r_l\epsilon_l + r_h\epsilon_h$. It is useful to introduce the quantities $s_{l,r} = \epsilon_{l,r}/\tilde{\epsilon}$, which, by definition, are connected through the relation $r_l s_l + r_h s_h = 1$. When the Cherenkov ring diameter is $d_c \leq d$, so that the ring can be entirely contained within one of the two regions, the probability of zero detected photoelectron is given by:

$$(P_{OFF})_{d_c \leq d} \sim P_\circ(r_l e^{-s_l N_{pe}} + r_h e^{-s_h N_{pe}}) \sim P_\circ(r_l e^{-s_l N_{pe}} + (1 - r_l)e^{-N_{pe}/(1-r_l)}) \,, \quad \text{(B.3)}$$

where N_{pe} is rigidity dependent according to eq. 6.18. The right hand side of eq. B.3 has been obtained by assuming for simplicity that $r_l s_l \sim 0$. Eq. B.3 expresses the probability of zero detected photoelectrons averaged over the sensor plane. The ratio between the probability $(P_{OFF})_{d_c \leq d}$ and the probability P_{OFF} calculated from eq. B.1 is thus given by:

$$\frac{(P_{OFF})_{d_c \leq d}}{P_{OFF}} = r_l e^{(1-s_l)N_{pe}} + (1 - r_l)e^{-\frac{r_l}{(1-r_l)}N_{pe}} \,. \quad \text{(B.4)}$$

In order to evaluate eq. B.4 as a function of s_l we need an estimate of the parameters d and r_l, which are the dimension of the low efficiency structures and their relative extension.

It is not easy to study the spatial structures of the MWPC detection efficiency for the single photoelectron. This is due to the fact that it is difficult to associate each pad having a Cherenkov signal to a specific photoelectron. Therefore, the amplitude of the signal induced by ionizing particles has been studied. A sample of muons has been selected by requiring that the particle tracks intersected the MWPC and for each event the pad with the greatest signal has been considered. Since the signal induced by a ionizing particle is ten time larger than the signal induced by a photoelectron, this pad most probably belongs to the ionization cluster. Fig. B.1 shows the distribution of the greatest signals as a function of the pad number along the x direction. The plot has been obtained by selecting a restricted region of the pad plane, and by projecting the resulting distribution over the x axis. The fixed value of 1023 refers to those

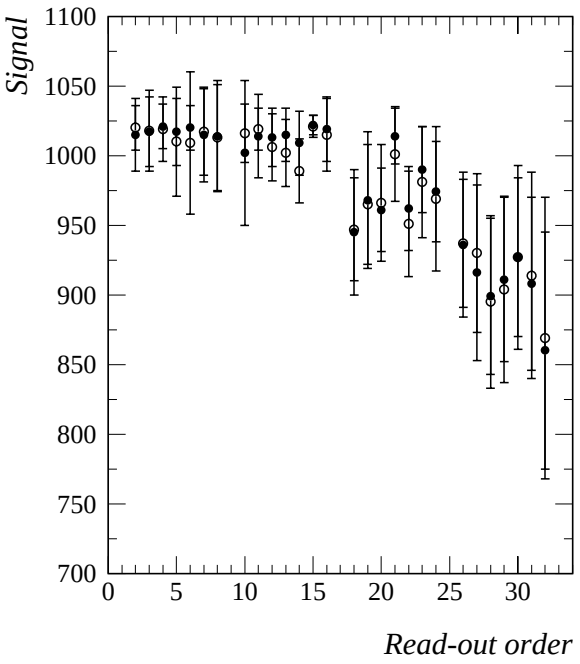

Figure B.2: *The greatest signal in the ionization cluster averaged over each front-chip channels connected to the same multiplexer. The values are ordered according to the readout sequence. Filled circles: ground data. Open circles: flight data.*

pads where the collected signal saturated the ADC. In this case the pedestal is not subtracted. From fig. B.1 it can be noticed that the mean pad signal is not uniform and that it shows two main structures. The pads are grouped in structures of 4 pads, which are related to the groups of 4×4 pads read out from the same front-end chip. Those pads connected to the same chip shows nearly the same behavior, while the mean signal varies for different chips in the range between 800 and 980 ADC channels. The pads are further grouped in structures of 16 pads each, which are related to groups of channels read out through the same multiplexer. This larger structure is nearly the same for all the multiplexers.

The observed variation of the pad signal is a well known effect and it is connected to a temporization feature of the read-out electronics. In fig. B.2 (filled circles) the mean signals of each front-end chip connected to the same multiplexer is plotted according to the read-out sequence. As can be seen, the signal amplitude decreases following the read-out order.

Similar structures are expected to be present also in the case of the signal induced by a photoelectron. Since the threshold for the signal detection was set to a fixed number of channels above the pedestal, this should result in a detection efficiency not

uniform over the pad plane.

From the above considerations, referring to eq. B.4, we can assume that the spatial dimensions of the structure are $d \sim 3$ cm, which is the size of the front-end chips, and that the relative extension of the low efficiency region is $r_l \sim 0.25$, which has been estimated from fig. B.1. From the maximum measured Cherenkov angle value it follows that the condition $d_c = d$ is satisfied when $R/R_{th} \sim 1.05$ and consequently $N_{pe} \sim 2$ (from eq. 6.18). The resulting value of eq. B.4 is equal to 1 when $s_l \sim 0.5$ and increase for decreasing s_l up to a value ~ 2.2 when $s_l = 0$.

This simple model shows that the give interpretation of the observed probability P_{OFF} is plausible. In order to reproduce the observations also quantitatively, a more complex model is required. Nevertheless, our approach has been to take as the best estimate of P_{OFF} the eq. B.2, with the the empirical correction factor $K(R/R_{th})$ obtained by fitting experimental data (eq. 6.20).

In order to check if the same effect was present during the flight, the mean signal induced by the ionizing particles at ground has been compared with that during the flight. As an example, in fig. B.2 the flight data (open circles) are shown together with ground data (filled circles) for the channels read-out through a same multiplexer. From the comparison it follows that there were no significant variation of the RICH MWPC behavior during the flight.

Appendix C

Normalization of the simulation

In order to estimate the content of protons and deuterons (N_p and N_D) in the total sample of selected $Z = 1$ particles (N_{TOT}) two methods have been considered. The first one is based on the normalization of the simulation output to data, over a proper rigidity interval. The second consists in the estimate of N_p and N_D performed bin-by-bin as described in section 6.5.2.

In order to normalize the simulation the total distribution of generated particles $N_\circ$ as a function of the measured rigidity has been normalized to the total number of selected $Z = 1$ events in the rigidity range $10 - 100$ GV. The distribution of background protons $N_{p,bk}$ has then been obtained as:

$$N_{p,bk} = N_\circ \left(\frac{1}{D/p + 1} \right) c_{sel} \ , \tag{C.1}$$

where D/p is the estimated deuteron-to-proton ratio in the rigidity range $26.7 - 45.1$ GV. The corresponding number of deuterons can be derived from the selected sample of events without a Cherenkov signal (N_{OFF}) as $N_D = (N_{OFF} - N_{p,bk})/\epsilon_{sel}$. The underline hypothesis of the above method is that both protons and deuterons have the same rigidity spectrum or, equivalently, that the deuteron-to-proton ratio is constant over the whole range. However, we preferred to estimated N_D bin-by-bin, using c_{sel} and ϵ_{sel} obtained from the simulation (section 6.5.1). Even this method depends on the assumption for both protons and deuterons to have the same rigidity spectrum. But, since c_{sel} and ϵ_{sel} depend on the spectrum shape only locally, we expect that the effect on the final result is lower than that one resulting from the global normalization.

The first method is useful to check the reliability of the instrument response model, by comparing the simulation output with data over a wide rigidity range, which extends

up to rigidities where the proton background outnumbers the deuteron component. The simulated background distributions shown in fig. 6.18 (shaded area) has been obtained from eq. C.1. The same method has been used to normalize the distribution of events without a Cherenkov signal shown in fig. 6.19. In this case the number of selected deuterons without a Cherenkov signal has been first calculated as:

$$N_{D,OFF} = N_{\circ} \left(\frac{D/p}{D/p+1} \right) \epsilon_{sel} \, . \tag{C.2}$$

The number of selected events has then been obtained as $N_{OFF} = N_{D,OFF} + N_{p,bk}$.

Bibliography

[1] Simpson J. A., Rev.Nucl.Part.Sci. **33**, 323 (1983)

[2] Ginzburg V. L. & Syrovatskii S. I., *Origin of Cosmic Rays*, Pergamon Press, 1964

[3] Longair M. S., *High Energy Astrophysics*, Cambridge University Press, 1981

[4] Berezinskiĭ V. S., Bulanov S. V., Dogiel V. A., Ginzburg V. L. & Ptuskin V. S., *Astrophysics of Cosmic Rays*, North-Holland, 1990

[5] Gaisser T. K., *Cosmic Rays and Particle Physics*, Cambridge University Press, 1990

[6] Apparao K. M. V., Proc. ICRC 13^{th}**1**, 126 (1973)

[7] Bogomolov E. A. *et al*, Proc. ICRC 16^{th}**1**, 330 (1979)

[8] Bogomolov E. A. *et al*, Proc. ICRC 24^{th}**2**, 598 (1995)

[9] Golden R. L. *et al*, Phys.Rev.Lett. **43**, 1264 (1979)

[10] Webber W. R. *et al*, Astrophys.J. **380**, 230 (1991)

[11] Papini P., PhD thesis, Università degli Studi di Firenze, Florence, Italy

[12] Finetti N., PhD thesis, Università degli Studi di Perigia, Perugia, Italy

[13] Lamanna G., PhD thesis, Università degli Studi di Bari, Bari, Italy `http://glamanna.home.cern.ch/glamanna/index1.html`

[14] Webber W. R. & Yushak M., Astrophys.J. **275**, 391 (1983)

[15] Beatty J. J. *et al*, Astrophys.J. **413**, 268 (1993)

[16] Reimer O. *et al*, Astrophys.J. **496**, 490 (1998)

[17] Hatano Y. *et al*, Phis.Rev.D **52**, 6219 (1995)

[18] Stephens S. A. & Golden R. L., Sp.Sci.Rev. **46**, 31 (1987)

[19] Stephens S. A., Adv.Sp.Res. **9**, 145 (1989)

[20] Mewaldt R. A. *et al*, AIP Conf.Proc. **183**, 124 (1989)

[21] Webber W. R., Adv.Sp.Res. **5**, 755 (1997)

[22] Davis A. J., Proc. ICRC 24^{th} **1**, 622 (1995)

[23] Cowsik R. & Wilson L., Proc. ICRC 13^{th} **1**, 500 (1973)

[24] Meneguzzi M., Nat.Phys.Scien. **241**, 100 (1973)

[25] Cowsik R. & Gaisser T. K., Proc. ICRC 17^{th} **2**, 218 (1981)

[26] Peters B. & Westergaard N. J., Astrophys.Sp.Sci. **48**, 21 (1977)

[27] Powell C. F. *et al.* , *The Study of Elementary Particles by the Photographic Method* Pergamon, New York, N.Y. (1959)

[28] Papini P., Grimani C. & Stephens S. A., Proc. ICRC 24^{th} **4**, 1044 (1995)

[29] Papini P., Grimani C. & Stephens S. A., Nuovo Cim. C **19**, 367 (1996)

[30] Vannuccini E., Papini P., Grimani C. & Stephens S. A., Proc. ICRC 27^{th} **10**, 4181 (2001)

[31] Hernández J. J., Phys.Lett.B**239**, 1 (1990)

[32] Ramaty R. & Lingenfelter R. E. , Astrophys.J. **155**, 587 (1969)

[33] Anderson L. *et al.* , Phys.Rev.C **28**, 1224 (1983)

[34] Greiner D. E. *et al.* , Phys.Rev.Lett.**35**, 152 (1975)

[35] Meyer J. P. , Astro.Astroph.Supp. **7**, 417 (1972)

[36] Dar A. *et al.* , Phys.Lett.B **87**, 136 (1979)

[37] Abrakhmanov E. O. *et al.* , Z.Phys.C **5**, 1 (1980) preprinted as JINR E1-11517 (1978)

[38] Aksinenko V. D. *et al.* , Nucl.Phys.A **348**, 518 (1980)

[39] Bokova L. N. *et al.* , preprinted as JINR P1-9364 (1975)

[40] Ableyev V. G. *et al.* , preprinted as JINR P1-10565 (1977)

[41] Lindstrom R. J., Greiner D. F. & Heckman H. H. , Bull.Am.Phys.Soc.**17**, 488 (1972)

[42] Jaros J. *et al.* , Phys.Rev.D **18**, 2273 (1978)

[43] Gulkanian G. R. *et al.* , preprinted as YERE-1150-27-89 (1989)

[44] Viryasov N. M. *et al.*, preprinted as JINR-P1-91-455 (1991)

[45] Grigalashvili N. S. *et al.*, Yad.Fiz. **48**, 476 (1988) Sov.J.Nucl.Phys. **48**, 301 (1988)

[46] Tanihata. I. *et al.*, Phys.Lett.B **160**, 380 (1985)

[47] Kox S. *et al.*, Phys.Rev.C **35**, 1678 (1987)

[48] Webber W. R. *et al.*, Phys.Rev.C **41**, 520 (1990)

[49] Webber W. R. *et al.*, Phys.Rev.C **41**, 533 (1990)

[50] Letaw R. J., Silberberg R. & Tsao C. H., Astrophys.J.Suppl. **51**, 271 (1983)

[51] Olson D. L. *et al.*, Phys.Rev.C **28**, 1602 (1983)

[52] Webber W. R. , Am. Inst.of Phys. Conf.Proc. **203**, 294 (1990)

[53] Glagolev V. V. *et al.*, Z.Phys.C **60**, 421 (1993)

[54] Abdullin S. K. *et al.*, Nucl.Phys.A **569**, 753 (1994)

[55] Blinov A. V. *et al.*, E-Print Archive nucl-ex/9910012 (1999)

[56] Bizard G. *et al.*, Nucl.Phys.A **285**, 416 (1977)

[57] Abdurakhimov A. Kh. *et al.*, Nucl.Phys.A **362**, 376 (1981)

[58] Alcaraz J. *et al.*, Phys.Lett.B **472**, 217 (2000)

[59] Sanuki J. *et al.*' E-Print Archive astro-ph/0002481 (2000)

[60] Boezio M. *et al.*, Astrophys.J. **518**, 457 (1999)

[61] Menn . *et al.*, Proc. ICRC 25^{th} **3**, 409 (1997)

[62] Bellotti R. *et al.*, Phys. Rev. D **60**, 052002 (1999)

[63] Buckley J. *et al.*, Astrophys.J. **429**, 736 (1994)

[64] Beatty J. J. *et al.*, Astrophys.J. **413**, 268 (1993)

[65] Seo E. S. *et al.*, Astrophys.J. **378**, 763 (1991)

[66] Müller D. *et al.*, Astrophys.J. **374**, 356 (1991)

[67] Engelmann J. J. *et al.*, Astro.Astroph. **223**, 96 (1990)

[68] McDonald F. B. *et al.*, J.Geoph.Res. **97**, 1557 (1992)

[69] von Rosenvinge T. T., McDonald F. B. & Trainor J. H., Proc. ICRC 16^{th} **12**, 170 (1979)

[70] Lezniak J. A. & Webber W. R., Astrophys.J. **202**, 265 (1975)

[71] Simon M. *et al.*, Astrophys.J. **239**, 712 (1980)

[72] Caldwell J. H., Astrophys.J. **218**, 269 (1977)

[73] Garcia-Munoz M., Mason G. M. & Simpson J. A., Astrophys.J. **202**, 265 (1975)

[74] Mason G. M., Astrophys.J. **171**, 139 (1972)

[75] Hsieh K. C., Mason G. M. & Simpson J. A., Astrophys.J. **166**, 221 (1971)

[76] Simpson J. A., Ann.Rev.Nucl.Part.Sci. **33**, 323 (1983)

[77] Ambriola M. *et al*, Nucl.Phys.(Proc.Suppl.)B **78**, 32 (1999)

[78] Bergström D. *et al* , Astrophys.J. **534**, 177 (2000)

[79] Bergström D., PhD thesis, Royal Institute of Technology, Stockholm, Sweden `http://www.particle.kth.se/group_docs/astro/research/CAPRICE.html`

[80] Boezio M. *et al*, Adv.Sp.Res. **27-4**, 669 (2001)

[81] Mocchiutti E. *et al*, Proc. ICRC 27^{th} **5**, 1634 (2001), Mocchiutti E. private comunication

[82] Hansen P. *et al*, Proc. ICRC 27^{th} **3**, 921 (2001)

[83] Vannuccini E. *et al*, Proc. ICRC 27^{th} **5**, 1638 (2001)

[84] Hof M. *et al*, Nucl.Instrum.Meth. **A345**, 561 (1994)

[85] Golden R. L. *et al*, Nucl.Instrum.Meth. **148**, 179 (1978)

[86] Hof M., PhD thesis,University of Siegen, Siegen, Germany (1996)

[87] Golden R. L. *et al*, Nucl.Instrum.Meth.A **306**, 366 (1978)

[88] Particle Data Group, EPJ C**3,1-4** (1998)

[89] Bocciolini M. *et al*, Nucl.Instrum.Meth.A **370**, 403 (1996)

[90] Ricci M. *et al*, Proc. ICRC 26^{th} **5**, 49 (1999)

[91] Francke T. *et al*, Nucl.Instrum.Meth.A **433**, 87 (1999)

[92] Bergström D., Licentiat thesis, Royal Institute of Technology, Stockholm, Sweden `http://www.particle.kth.se/group_docs/astro/research/CAPRICE.html`

[93] Bergström D. *et al*, To be published in Nucl.Instrum.Meth.A (1999)

[94] Agakichiev G. *et al*, Nucl.Instrum.Meth.A **371**, 243 (1996)

[95] Boezio M., PhD thesis, Royal Institute of Technology, Stockholm, Sweden `http://www.particle.kth.se/group_docs/astro/research/CAPRICE.html`

[96] Weber N., PhD thesis, Royal Institute of Technology, Stockholm, Sweden `http://www.particle.kth.se/group_docs/astro/research/CAPRICE.html`

[97] Sullivan J. D. *et al*, Nucl.Instrum.Meth. **95**, 5 (1971)

[98] D'Agostini G., Nucl.Instrum.Meth.A **362**, 487 (1995)

[99] Lafferty G. D. & Wyatt T. T., Nucl.Instrum.Meth.A **355**, 541 (1995)

[100] Codino A. *et al*, J.Phys.G(Nucl.Part.Phys.) **23**, 1751 (1997)

[101] Webber W. R. *et al*, Astrophys.J. **275**, 391 (1983)

Desidero, innanzitutto, ringraziare tutti i colleghi della collaborazione WiZard con i quali ho lavorato e collaborato per più di tre anni. Durante il Dottorato di Ricerca ho avuto il piacere di lavorare con il Prof. Alfred Stephens. La nostra collaborazione è stata breve ma costruttiva. Un particolare ringraziamento va alla Dott. Catia Grimani e al Dott. Emiliano Mocchiutti per la loro disponibilità e la loro collaborazione. Un ringraziamento affettuoso va a tutti i colleghi e amici del gruppo WiZard di Firenze e a tutti i fedeli della pausa caffè. Devo indubbiamente l'opportunità che ho avuto di studiare fisica ai miei genitori, Antonio ed Eva, e per questo non li ringrazierò mai abbastanza. Ringrazio mia sorella Laura, per avermi pazientemente sopportato, e tutti i miei amici. Un ultimo ringraziamento va agli amici e ai "maestri" della Scuola Internazionale di Comics, che, a modo loro, hanno contribuito al raggiungimento di questo importante traguardo.